

Dissertations and Theses

5-2017

Performance Analysis of a Coaxial Helicopter in Hover and Forward Flight

Stanrich D. Fernandes

Follow this and additional works at: <https://commons.erau.edu/edt>



Part of the [Aerospace Engineering Commons](#)

Scholarly Commons Citation

Fernandes, Stanrich D., "Performance Analysis of a Coaxial Helicopter in Hover and Forward Flight" (2017). *Dissertations and Theses*. 326.
<https://commons.erau.edu/edt/326>

This Thesis - Open Access is brought to you for free and open access by Scholarly Commons. It has been accepted for inclusion in Dissertations and Theses by an authorized administrator of Scholarly Commons. For more information, please contact commons@erau.edu.

PERFORMANCE ANALYSIS OF A COAXIAL HELICOPTER IN
HOVER AND FORWARD FLIGHT

A Thesis
Submitted to the Faculty
of
Embry-Riddle Aeronautical University
by
Stanrich D. Fernandes

In Partial Fulfillment of the
Requirements for the Degree
of
Master of Science in Aerospace Engineering

May 2017
Embry-Riddle Aeronautical University
Daytona Beach, Florida

PERFORMANCE ANALYSIS OF A COAXIAL HELICOPTER IN
HOVER AND FORWARD FLIGHT

by

Stanrich D. Fernandes

Thesis prepared under the direction of the candidate's committee chairman, Dr. J. Gordon Leishman, Department of Aerospace Engineering, and has been approved by the members of the thesis committee. It was submitted to the School of Graduate Studies and Research and was accepted in partial fulfillment of the requirements for the degree of Master of Science in Aerospace Engineering.

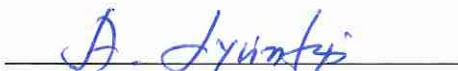
THESIS COMMITTEE



Chairman, Dr. J. Gordon Leishman



Member, Dr. William Engblom



Member, Dr. Tasos Lyrintzis



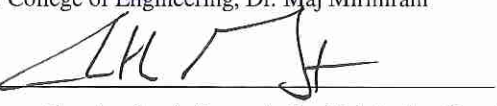
Graduate Program Coordinator, Dr. Magdy Attia

4/24/2017
Date



Dean of College of Engineering, Dr. Maj Mirmirani

4/24/2017
Date



Vice Chancellor, Academic Support, Dr. Christopher Grant

4/26/2017
Date

ACKNOWLEDGMENTS

I would like to take this opportunity to acknowledge everyone who has helped me in the course of my work at Embry-Riddle Aeronautical University. I am very grateful to my advisor and mentor, Dr. J. Gordon Leishman, for his immense help and encouragement. His critical evaluation of my work always motivated me to give my best. His passion for rotary wing aircraft is very inspiring and drove me during my thesis work. I would also like to thank Dr. W. Engblom and Dr. A. Lyrintzis for their valuable inputs toward reaching the goals of this study. I am grateful to Dr. Bharath Govindarajan of the University of Maryland for his help during the initial stages of this research work, during which he helped me to understand the basis of the computer code.

All of my work would not have been possible without the support of my parents, Caitano and Dorothy, who have always supported me and pushed me to work harder. I would also like to thank Sonal, Jack, Catty, Afifano and Sera for their continued support.

I would like to thank my colleagues at the PIV Lab, Sravan, Vinay and Dr. Zheng for their help during this research. I would like to thank my friends Amay, Anuj, Himanshu, Sumanth and Yogesh for their help and company during this journey. Special thanks to Samprada for always being there for me during the good and bad times.

TABLE OF CONTENTS

	Page
LIST OF TABLES	vi
LIST OF FIGURES	vii
NOMENCLATURE	x
ABSTRACT	xiii
1 Introduction	1
1.1 History	2
1.2 Motivation for the Present Work	6
1.3 Prior Work and Literature Review	8
1.3.1 Experiments	11
1.3.2 Numerical Studies	15
1.4 Goals of the Present Work	20
1.5 Outline of the Thesis	21
2 Methodology	22
2.1 The Free-Vortex Wake Problem	22
2.2 Maryland Free Wake Method	26
2.2.1 Discretization of the Physical Problem	26
2.2.2 Transformation of PDE	28
2.2.3 Numerical Integration Scheme	30
2.2.4 Blade Aerodynamic Model	30
2.3 Rotor Trim Methodology	34
3 Results and Discussion	39
3.1 Validation	39
3.1.1 Harrington Rotors	40
3.1.2 University of Texas (UT) Rotor	49
3.2 Forward Flight Validation	52
3.3 Coaxial Rotor and Equivalent Single Rotor	64
3.3.1 Equivalent Single Rotor	64
3.3.2 Hover Performance Comparison: Harrington 2	67
3.3.3 Forward Flight Performance Comparison: UT Coaxial Rotor	68
3.4 Inter-Rotor Spacing: Harrington 2	77
3.5 Effects of Comparison with Isolated rotors: UT coaxial rotor	83
4 Conclusions and Recommendations	92

	Page
4.1 Conclusions	92
4.2 Recommendations for Future Work	95
REFERENCES	103
A Appendix: Rotor Geometries	104
B Appendix: Vortex Core Model	107
C Appendix: MATLAB Code for Contour Plots	111
D Appendix: MATLAB Code for Wake Boundary	133

LIST OF TABLES

Table	Page
3.1 <i>Rotor geometry of the Harrington 2 rotor and its equivalent single rotor.</i> . . .	66
3.2 <i>Rotor geometry of the UT coaxial rotor and its equivalent single rotor.</i> . . .	70
A.1 <i>Rotor geometry of the Harrington 1.</i>	104
A.2 <i>Rotor geometry of the Harrington 2.</i>	105
A.3 <i>Rotor geometry of the UT Rotor.</i>	106

LIST OF FIGURES

Figure	Page
1 Jacob Ellenmahher's coaxial helicopter in free flight.	3
2 Corradino d'Ascanio's coaxial helicopter designed in 1930, which held flight records during its time.	4
3 First successful coaxial helicopter designed by Louis Breguet and René Dorand.	5
4 Ka-50 light-weight attack helicopter (Source: http://Airliners.net).	6
5 Idealization of the curved rotor wake into straight line segments connected by collocation points [2].	23
6 Schematic showing the vortex wake of the coaxial rotor system [23].	27
7 Discretization of the rotor wake [39].	27
8 Discretized computational domain [40].	28
9 Schematic of the Weissinger-L model [23].	31
10 Airfoil coefficients for the NACA 0012.	33
11 Rotor blade shape of Harrington 1 rotor.	40
12 Power polar for the Harrington 1 rotor.	42
13 Wake geometry of the Harrington 1 rotor in hover at $C_T = 0.004$	42
14 Predicted inflow ratio distribution of the upper and lower rotors for the Harrington 1 rotor in hover at $C_T = 0.004$	43
15 Predicted spanwise distribution of thrust on the upper and lower rotors for the Harrington 1 rotor in hover at $C_T = 0.004$	44
16 Predicted spanwise distribution of torque on the upper and lower rotors for the Harrington 1 rotor in hover at $C_T = 0.004$	45
17 Predicted spanwise lift coefficient on the upper and lower rotors for the Harrington 1 rotor in hover at $C_T = 0.004$	46
18 Contour plot showing: (a) Inflow ratio and (b) Coefficient of lift across the Harrington 1 rotor.	47

Figure	Page
19 Blade shape of the Harrington 2 rotor.	48
20 Power polar for the Harrington 2 rotor.	49
21 Contour plot showing: (a) Inflow ratio and (b) Coefficient of lift across the Harrington 2 rotor.	50
22 Blade shape of the University of Texas coaxial rotor.	50
23 Power polar for the University of Texas coaxial rotor.	51
24 Contour plot showing: (a) Inflow ratio and (b) Coefficient of lift across the UT coaxial rotor.	52
25 Forward flight comparison for the Harrington 1 rotor with experimental results. $C_T = 0.0048 V_{tip} = 142.95 \text{ m/s}$	54
26 Lift to drag ratio for the Harrington 1 rotor. $C_T = 0.0048 V_{tip} = 142.95 \text{ m/s}$	55
27 Thrust sharing for the Harrington 1 rotor. $C_T = 0.0048 V_{tip} = 142.95 \text{ m/s}$	56
28 Geometry of the blade tip vortices for varying advance ratio.	57
29 Instantaneous contours of inflow distribution over the upper and lower rotors of the Harrington 1 rotor.	58
30 Instantaneous contour of inflow distribution over the upper and lower rotors of the Harrington 1 rotor.	59
31 Comparisons between the predicted and measured wake geometry for the Ka-32 rotor.	61
32 Comparisons between the predicted and measured wake geometry for the Ka-32 rotor.	62
33 Condensation of the rotor wake of the Ka-32 helicopter in hover.	63
34 Comparison between the Harrington 2 rotor and its equivalent single rotor in hover.	67
35 Variation in induced and profile power at varying system thrusts for the Harrington 2 rotor compared with its equivalent single rotor.	68
36 Inflow distributions across the blade span of the Harrington 2 rotor and its equivalent single rotor in hover. $C_T = 0.005$	69
37 Thrust gradient across the blade span of Harrington 2 and its equivalent single in hover. $C_T = 0.005$	69
38 Power required by the UT coaxial rotor compared to its equivalent single rotor in forward flight.	71

Figure	Page
39 Lift-to-drag ratios of the UT coaxial rotor compared to its equivalent single in forward flight.	72
40 Thrust sharing between the upper and lower rotors of the UT coaxial rotor in forward flight.	73
41 Wake geometry produced by the UT rotor.	74
42 Lift coefficient distribution across the UT rotor compared to its equivalent single rotor at $\mu = 0.2$	75
43 Lift coefficient distribution across the UT rotor compared to its equivalent single rotor at $\mu = 0.225$	76
44 Lift coefficient distribution across the UT rotor compared to its equivalent single rotor at $\mu = 0.25$	77
45 Power polar of the Harrington 2 for varying inter-rotor spacings.	78
46 Decomposition of induced and profile power for varying inter-rotor spacing.	79
47 Spanwise inflow ratio across the Harrington 2 rotor.	80
48 Inflow ratio across the upper and lower rotors of the Harrington 2 rotor.	82
49 Thrust sharing for varying inter-rotor spacings of the Harrington 2 rotor.	83
50 Wake boundary as affected by varying inter-rotor spacing of the Harrington 2 rotor.	84
51 Performance of the UT rotor compared to isolated rotor system operating at the same thrust.	85
52 Power in forward flight for the upper and lower rotors of UT rotor compared to isolated rotors operating at same thrust.	87
53 Lift-to-drag ratios of the upper and lower rotors of the UT rotor compared to isolated rotors.	88
54 Inflow ratio across UT rotor compared to isolated rotors in hover.	89
55 Inflow ratio across UT rotor compared to isolated rotors at $\mu = 0.1$	90
56 Inflow ratio across UT rotor compared to isolated rotors at $\mu = 0.2$	91
57 Vortex core model [2].	108
58 Non-dimensional tangential velocity profiles [2].	110

NOMENCLATURE

A	Rotor disk area (for one rotor), m^2
c	Blade chord, m
c_{root}	Blade root chord, m
c_{tip}	Blade tip chord, m
C_d	Sectional drag coefficient
C_{d_0}	Minimum or zero-lift profile drag coefficient
C_l	Sectional lift coefficient
C_{l_α}	Sectional lift-curve-slope, rad^{-1}
C_P	Rotor power coefficient, $= P/\rho A \Omega^3 R^3$
C_Q	Rotor torque coefficient, $= Q/\rho A \Omega^2 R^3$
C_T	Rotor thrust coefficient, $= T/\rho A \Omega^2 R^2$
$C_{T_{\text{req}}}$	Required or target thrust coefficient of coaxial rotor system
D_f	Equivalent parasitic drag area of airframe, m^2
DL	Disk loading
i, j, k	Unit vectors along the coordinate axes
I	Influence coefficient matrix used in the Weissinger-L model
I_β	Flapping moment inertia of the blade, kg m^2
I_B	Influence coefficient matrix for the bound circulation
I_{NW}	Influence coefficient matrix for the near-wake circulation
\mathbf{J}	Jacobian matrix
k_β	Flapping spring stiffness, Nm rad^{-1}
M_β	Flapping moment about the blade hinge, Nm
N_b	Number of blades (for one rotor)
N_s	Number of spanwise segments along the rotor blade
P	Rotor power, kW
P_i	Induced power, KW
Q	Rotor torque, Nm
r	Radial distance of a point on the blade from the vortex, m
\mathbf{r}	Position vector of a collocation point, m
\mathbf{r}_0	Initial position vector of a collocation point, m
R	Rotor radius, m
z/R	Non-dimensional inter-rotor spacing distance
T	Rotor thrust, N
v	Induced velocity, m s^{-1}
\mathbf{V}	Velocity vector at collocation point, ms^{-1}
V_∞	Forward flight speed, ms^{-1}

\mathbf{V}_∞	Forward flight velocity of the helicopter, ms^{-1}
\mathbf{V}_B	Induced velocity component from the bound circulation, ms^{-1}
\mathbf{V}_{FW}	Induced velocity component from the free-vortex trailers, ms^{-1}
\mathbf{V}_{NW}	Induced velocity component from the near wake trailers, ms^{-1}
\mathbf{V}_{ind}	induced velocity resulting from wake effects, ms^{-1}
x, y, z	Cartesian coordinates, m, m, m
\mathbf{x}	Vector of control input parameters
\mathbf{y}	Response vector

Greek Symbols

α_s	Forward tilt of the rotor shaft, deg
β_0	Blade coning angle, rad
β_{1c}	Longitudinal flapping angle, rad
β_{1s}	Lateral flapping angle, rad
Γ	Circulation associated with a vortex filament, m^2s^{-1}
λ_i	Induced inflow ratio, $v_i/\Omega R$
λ_∞	Non-dimensional axial velocity, $V_\infty/\Omega R$
μ	Advance ratio
ν_β	Non-dimensional rotating blade flapping frequency
ν_i	Induced velocity, ms^{-1}
$\Delta\zeta$	Discretization along spatial direction, rad
$\Delta\psi$	Temporal or azimuthal discretization, rad
Ω	Rotational speed of the rotor, rad s^{-1}
ϕ	Inflow angle, rad
ρ	Air density, kg m^{-3}
σ	Rotor solidity, $N_b c / \pi R$
σ_{eq}	Equivalent rotor solidity
σ_{coax}	coaxial rotor solidity
θ	Blade pitch, rad
θ_0	Collective blade pitch, rad
θ_{1c}	Lateral cyclic pitch, rad
θ_{1s}	Longitudinal cyclic pitch, rad
ω_0	Non-rotating blade flapping frequency, $k_\beta / I_\beta \Omega^2$, rad s^{-1}
ω_β	Rotating blade flapping frequency, rad s^{-1}

Subscripts

l	Refers to lower rotor
u	Refers to upper rotor

Superscripts

$\dot{()}$	Time derivative ($= \partial/\partial t$)
\star	Azimuthal derivative ($= \partial/\partial\psi = \Omega\partial/\partial t$)
$()$	Refers to coaxial system
coaxial	Refers to equivalent single rotor
equiv	Refers to lower rotor
l	Refers to total
tot	Refers to upper rotor
u	

List of Abbreviations

AoA	Angle of Attack
BEMT	Blade Element Momentum Theory
CFD	Computational Fluid Dynamics
DL	Disk Loading
FDE	Finite Difference Equation
FVM	Free Vortex Method
MFW	Maryland Free Wake
NACA	National Advisory Committee for Aeronautics
NASA	National Aeronautics and Space Administration
PC2B	Predictor-Corrector 2 nd -order Backward Difference
RANS	Reynolds Averaged Navier-Stokes
SMT	Simple Momentum Theory
TPP	Tip Path Plane
VTM	Vorticity Transport Model

ABSTRACT

The performance of a coaxial rotor system has been analyzed by establishing a proper basis of comparison between a conventional single rotor and coaxial rotor. An attempt has also been made to better understand the complicated aerodynamic interactions associated with coaxial rotor wakes by using a free-vortex methodology (FVM). The FVM is a Lagrangian-based wake convection methodology, which solves for the evolution of the vortical wake produced by the rotor blades under the influence of an external flow. The extent to which the two rotors interact with each other was found to be highly dependent on the inter-rotor spacing. To this end, parametric variations of inter-rotor spacing were performed to show the effect on performance on each rotor and also as a system. An attempt was made to quantify the effect of aerodynamic interference on the performance of the upper and lower rotor by comparing them to an isolated rotor. It was shown that the equivalent single rotor performs better than the coaxial rotor at moderately high advance ratios, while the coaxial rotor performs better in hover. The inter-rotor spacing profoundly affected the performance of the coaxial rotor system, giving higher power requirements at lower inter-rotor spacing. Finally, it was shown that the upper rotor becomes affected by the lower rotor in hover, and while this was an expected result in hover and low advance ratios, the performance of the upper rotor was also affected at higher advance ratios.

1. Introduction

Helicopters lifted by counter-rotating coaxial rotor systems have existed since the earliest days of attempts at vertical flight. In fact, most of the earliest helicopter contraptions built prior to 1930 were twin rotor concepts of various types, with either coaxial, tandem or side-by-side rotor placements. However, various technical challenges building and flying the coaxial rotor configuration led to the adoption of the single rotor/tail rotor helicopter configuration, which has been the basis for most helicopters built since 1940. Nevertheless, the last few years have seen engineers revisit the coaxial rotor concept as a configuration that could potentially open up the flight envelope of the helicopter, allowing it to reach higher forward speeds and also reach better levels of operational efficiency. Recently, much effort has been put into developing the coaxial helicopter configuration in the U.S., the most notable one being Sikorsky's X2 demonstrator, which was followed by the S-97 *Raider* [1] as pre-production flight demonstrator.

The present work analyzes the performance of coaxial helicopters, particularly from the perspective of better understanding the aerodynamic interactions between the upper and lower rotors. In addition, the overall performance of a coaxial helicopter is compared to an “equivalent” conventional single rotor, the objective being to objectively assess any performance benefits for a coaxial rotor. This thesis discusses the motivation for the present work, which is followed by the literature review of the prior work done previously

and being done currently on coaxial rotors, including numerical and experimental efforts. Following this, the specific goals set down for the present study are discussed in detail.

1.1 History

Early forms coaxial rotor concepts actually date back over two centuries. The first coaxial rotor concept seems to have been developed by Mikhail Lomonosov, his bench-top “Aerodynamic” machine being demonstrated around 1754. While the rotors were able to create thrust, the machine contained many gears and other mechanisms and was far too heavy to fly.

During the 18th century, several French scientists including Ponton d’Amecourt began to study various small rotor devices that could make short free-flights. Most of these devices were composed of turkey feathers that were attached at the end of a stick, which were then spun by the tension in a bowstring and released into free flight. While mostly toys, many inventors and engineers were inspired to think about how to scale up the idea to a human-carrying rotor concept.

In 1912, Jacob Ellehammer from Denmark built a coaxial helicopter, which was also one of the first helicopters to takeoff under its own power and sustain free flight with a pilot on board; see Fig. 1. During early 1930s, an Italian aeronautical engineer Corradino d’Ascanio, built a coaxial rotor helicopter, as shown in Fig 2. The d’Ascanio helicopter held modest records for the era, including time aloft, forward speed and altitude reached.

With the overwhelming success of the modern helicopter in the single rotor/tail rotor configuration, one might think that it was this configuration that would taste success be-

fore any other configuration. Yet, the first practical helicopter was actually a coaxial rotor helicopter [2], which is shown in Fig. 3. Louis Breguet and René Dorand developed this helicopter, which for its time held a number of records, yet it did not go into production. Boulet [3] and Liberatore [4] discuss various other coaxial rotor helicopter prototypes, but not all of them were able to achieve successful flight.

By 1935, Igor Sikorsky's VS-300 was able to hover, fly sideways and backwards under complete control. Sikorsky's huge success with the VS-300 and shortly after with the R-4 and R-5 quickly popularized the single rotor configuration. Meantime, other configurations, including the coaxial and side-by-side rotor configurations, saw little further development during the following decades as the single rotor helicopter platform continued to mature.

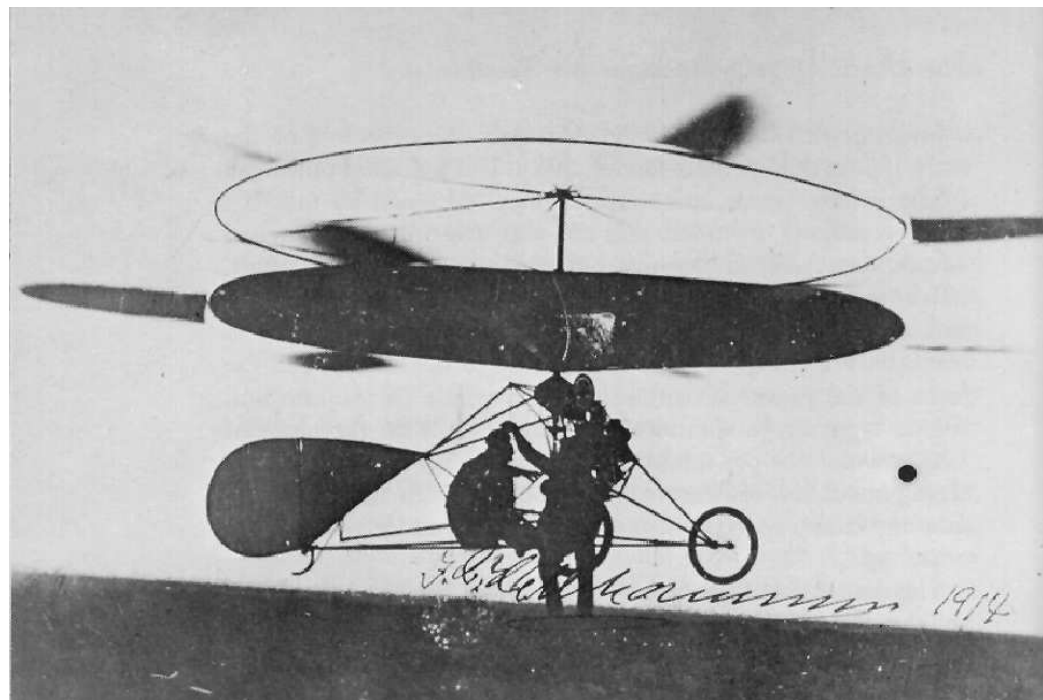


Fig. 1: Jacob Ellenmahher's coaxial helicopter in free flight.

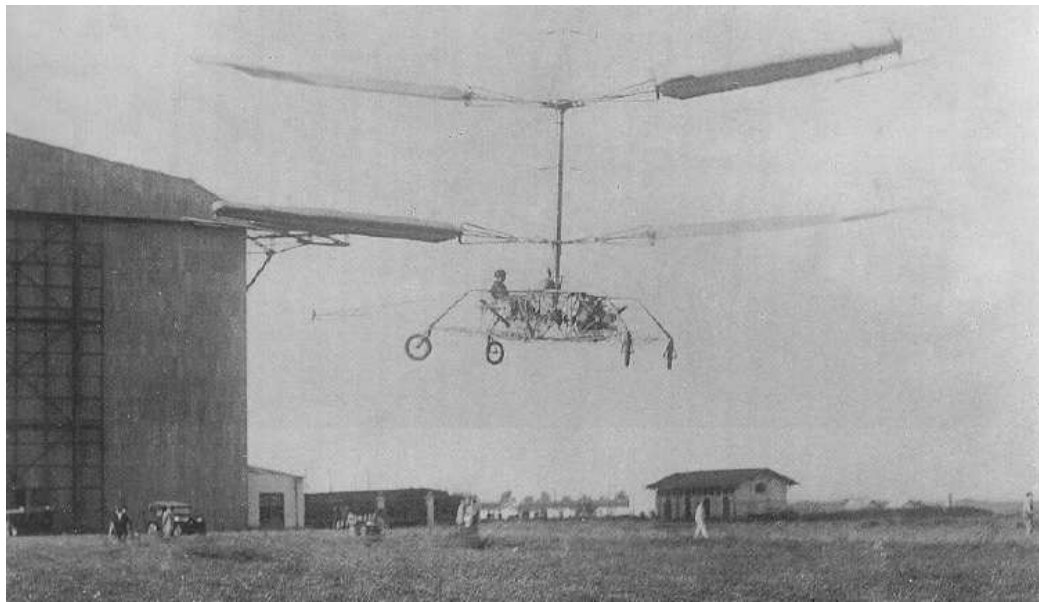


Fig. 2: Corradino d'Ascanio's coaxial helicopter designed in 1930, which held flight records during its time.

However, the coaxial rotor design was adopted by the Kamov company in Russia in the 1950s, and they have continued to develop their coaxial rotor helicopter concepts into the 21st century. Their first machines were Ka-8 and Ka-10, which because of the relatively compact size of a coaxial rotor compared to a single rotor could be more easily operated off ships. The most notable Kamov machines are the Ka-15, Ka-18 and Ka-20, which were very successful light- and medium-weight helicopters and have seen operational service in many countries. The more recent Ka-50 is an attack helicopter, Fig 4, which has been exclusively used by the Russian Army since 1995 [5].

One of the earliest coaxial rotor helicopters developed in the U.S. was called the Advancing Blade Concept (ABC) helicopter [6]. This new rotorcraft design was meant to address the major problems faced by the conventional helicopter, namely the lifting potential



Fig. 3: First successful coaxial helicopter designed by Louis Breguet and René Dorand.

and maximum speed capability. Two ABC aircraft were built, which showed the potential for the coaxial rotor design to reach airspeeds above 200 knots. But this aircraft did not go into production. This ABC design received renewed attention in 2008 when Bagai [1] presented the blade design for the X2 Technology Demonstrator aircraft, a derivative of the ABC helicopter. The innovative and unorthodox rotor design consisted of non-uniform planform, different airfoils and varying blade twist distributions, and showed the potential for significantly improved speed and efficiency. In 2010, the X2 reached speeds of up to 250 knots, which was much faster than any other helicopters at that time. A derivative of the X2, called the S-97 *Raider*, has completed multiple successful test flights and is expected to fly at speeds up to 250 knots.



Fig. 4: Ka-50 light-weight attack helicopter (Source: <http://Airliners.net>).

1.2 Motivation for the Present Work

Over the years, conventional thinking has led designers to believe that a conventional single main rotor and tail rotor helicopter configuration is superior, and hence it has become the default or preferred configuration for most new helicopters. However, recent analysis suggest that performance capabilities and other abilities of a coaxial rotor system may have been underestimated, and they are certainly not as fully understood as single rotors. Furthermore, the tail rotor of a conventional design consumes up to 10% of the engine power, power that is not used to generate lift. For a coaxial helicopter the problem of anti-torque is “naturally” solved because the counter-rotating upper and lower rotor can be trimmed to achieve a torque balance, and hence all of the engine power can be used for lift and propulsion. Furthermore, because of the different thrust sharing between the upper

and lower rotors of the coaxial configuration, coaxial rotors are capable of carrying more weight and/or higher load factors because of the naturally lower blade loading (C_T/σ) and lift coefficients on each rotor. From Naval operations perspective, the coaxial rotor helicopter often benefits because of its smaller footprint and so requires less space on aircraft carrier decks. The smaller overall size of the rotor of a coaxial helicopter also enhances its maneuverability, which is vital in combat situations.

However, there are a number of disadvantages of a coaxial configuration, some of them being the increased total weight from the more mechanically complex power transmission system, which is compounded by the weight and cost of the additional main rotor system. Aerodynamic interactions between the two rotors can also degrade performance, and can be a source of higher vibrations because of blade vortex interactions as the lower rotor ingests the wake of the upper rotor.

Other than the obvious mechanical complexity, another reason that the coaxial has not seen widespread use could be that the comparison between a conventional and coaxial helicopter has not been done thoroughly by means of experiments or calculations, which has led to a perception that conventional helicopters are better. Another reason could be the lack of understanding of rotor-on-rotor aerodynamic interactions and the influence of the wake on the power requirement for flight. However, with advances in computational capabilities and development of high fidelity aerodynamic models that predict the wake structure accurately, today it is possible to conduct more detailed research studies into coaxial rotor systems so as to better understand how to design them to achieve desired levels of performance.

The aerodynamic interactions between the upper and lower rotors of a coaxial configuration are rather complex, and may appear to be detrimental to the overall performance of the helicopter. Obviously, inter-rotor spacing is a major factor affecting these aerodynamic interactions, which occur primarily in hover and may diminish in forward flight. Generally, higher inter-rotor spacing is desired for efficient hovering performance [7], but a higher inter-rotor spacing increases the parasitic drag (due to the larger exposed shaft between the rotors) in forward flight. It is known that when the lower rotor operates in the fully developed wake of the upper rotor the induced power factor for the system is minimum [7]. The modern helicopter is also expected to fly at very high speeds (approaching 200 knots), so it is crucial that the inter-rotor spacing is minimized because the power requirement increases rapidly with increase in airspeed from the parasitic drag. Clearly, a better understanding of how the inter-rotor spacing affects the aerodynamic performance of a coaxial rotor system in hover and forward flight will potentially lead to more efficient designs.

1.3 Prior Work and Literature Review

Predicting the aerodynamic interactions for a coaxial rotor system is a difficult task. Simple momentum theory (SMT) and blade element momentum theory (BEMT) have been previously used for rotor analysis. Harrington [8] and Dingeldein [9] used momentum theory to compare with experimental measurements of coaxial rotor performance. Recently, Leishman [7] applied variations of the SMT and BEMT to coaxial rotors, and showed very good comparisons with measurements of coaxial rotor performance in hovering flight.

Another approach to solve this problem is to use a free-vortex method to obtain the induced velocities in the rotor wake. Bagai and Leishman [10] used the free-wake method (FVM) to study the performance of various multi-rotor systems, including coaxial rotors. This method captures the three-dimensional wake interactions between the two rotors of the coaxial configuration, but the analysis only considers the blade tip vortices. However, their results showed very good agreement with the measured wake displacements and performance measurements of a coaxial rotor. A similar free vortex wake methodology within the CAMRAD II code has also been used for the analysis of coaxial rotors, good comparisons with experimental results for full-scale and model-scale coaxial rotors being shown by Lim et al. [11].

Computational Fluid Dynamics (CFD) has also been used to examine the aerodynamic interactions between the two rotors of a coaxial configuration. CFD techniques are usually based on time-dependent solutions of the Navier-Stokes equations in the form of RANS methods (Reynolds-Averaged Navier-Stokes). All the applicable flow physics in RANS except for turbulence are treated from first principles and much better predictions of the rotor flow can be potentially obtained because viscous effects are included. One of the drawbacks of the various CFD tools, however, is the large computational requirements, substantial processing power and data storage requirements. Another drawback of CFD is the numerical dissipation within the finite difference schemes, which tends to diffuse concentrated vorticity such as tip vortices. Numerical dissipation not only affects the convection of the wake but introduces non-physical effects that makes the preservation of the vortical wake to older wake ages very challenging. Even though such problems have been

resolved by the use of finer computational grids, higher-order schemes and grid adaptation, conducting CFD analysis for a coaxial rotor system still remains a very difficult task.

In general, all of the various computational methodologies from momentum theory to CFD tend to give reasonably good predictions of rotor performance such as thrust and power. These methods, of course, have very different levels of complexity and computational requirements. In some cases, BEMT despite its simplicity, better predicts rotor performance than CFD. However, the physics of the complex three-dimensional flow that occurs between the upper and lower rotors of a coaxial is better captured in the FVM method and, at least in principle, with CFD.

Though the results obtained from all three methodologies give some success when compared to the measurements, the need for more detailed experimental data for validation (such as blade loads and wake surveys) should not be underestimated. Experiments have always been the most reliable source of interpretation of rotor aerodynamics and several have been conducted to study the performance of coaxial rotors. Simulations of flight conditions in wind tunnels tend to give good assessments of rotor performance such as thrust and power. However, the process of making measurements still carries with it a number of issues and concerns, including the exact trim procedures used to set the rotor operating state.

Previous research conducted on coaxial helicopters through the early 1990s has been summarized by Coleman [12]. The effects of wake interference, wake modeling, performance comparison, etc. have been discussed based on published information. The comparison between the coaxial and a “equivalent” single rotor suggests that coaxial performs

better than an equivalent single rotor. However, the description of an “equivalent” single rotor is not fully defined by Coleman. One questionable observation made in this paper that is that inter-rotor spacing does not influence rotor performance, which seems surprising if not downright questionable.

1.3.1 Experiments

Over the years, various experiments have been conducted to determine the performance of coaxial rotor. The earliest systematic experiments on a coaxial configuration was by Harrington at the NACA Langley Research Center [8]. In this experiment, the thrust and power performance of a coaxial rotor was measured for various blade pitch settings and blade tip speeds. The rotor was tested with two different sets of blades; both sets varied in blade thickness from root to tip but one blade was also tapered in planform.

Tests on both the single rotor and coaxial rotor configurations were made to determine the relative performance merits of the two rotor systems. The results obtained compared well with performance based on a variation of momentum theory. For the hover performance comparisons, the coaxial rotor was assumed to be a single four-bladed rotor with same overall solidity. However, this assumption is critical and it will be shown in this thesis that such assumptions affects the conclusions drawn about the relative levels of rotor performance. This latter study also states that accurate estimation of zero-lift profile drag of the blade section is essential to obtain reliable predictions of overall rotor performance.

Several years later, Dingeldein conducted further experiments to measure the performance of twin rotor configurations in the wind tunnel in forward flight operation, namely a

coaxial rotor and a tandem rotor [9]. In this experiment, Dingeldein used the same coaxial rotor configuration used previously by Harrington. The results that were presented suggested that the conventional single rotor configuration is more efficient than a coaxial rotor system because the results indicate that the coaxial requires about 14% more power than the conventional rotor for same operating conditions. However, to come to this conclusion, the basis used for comparison is important.

For example, the effects of various factors such as disk loading and rotor solidity have to be carefully matched to be able to make meaningful comparisons of the two rotors systems. Although the rotor solidity in both the cases was equal, the disk loading was not the same and is well known that the disk loading as a parameter is fundamental to rotor performance. In fact, if the performance metric were to be compared at the same disk loading, then the geometry of the single rotor would be different. Later in this thesis it will be shown how an “equivalent” single rotor must be properly derived from a coaxial rotor configuration such that basis for meaningful comparisons of performance can be established.

Further hover performance studies of coaxial rotors were conducted in the following years. In 1969, Cheney [6] concluded that coaxial configurations could represent an important technological advance in the evolution of the next-generation rotorcraft technology. His reasoning included an improved and more efficient lifting system (no power required for anti-torque and entire power is used for lifting), potential for higher cruise speeds, and simplicity of rotor control. Rorke [13] measured the hover performance of a coaxial rotor configuration and concluded that the coaxial outperformed a conventional rotor system. However, the methodology used for rotor trim is not mentioned in these studies, hence the

usefulness of these results for validation purposes remains somewhat uncertain. In 1977, Arents [14] conducted various experiments on Sikorsky's ABC rotor and concluded that it performs better than most of the military helicopters in service at that time. The reasoning behind this claim was once again the absence of a power-consuming tail rotor with the coaxial configuration. Yet, the basis of comparison between the two configurations was again left rather unclear, so the conclusions cannot be considered as substantiated.

More recently, Ramasamy [15] conducted experiments to study the hover performance of coaxial rotor, tandem rotor and tilt rotor configurations. For the purpose of this study, a sub-scale rotor with a radius of 0.66 m was used. The blades were uniform in chord planform with a chord length of 0.0647 m. Twisted and untwisted blade sets were used separately to study the aerodynamic interference between the two rotors. Ramasamy concluded that the performance of the coaxial configuration was better than an "equivalent" solidity single rotor because of axial separation effects and wake swirl recovery. The coaxial configuration, however, consumed up to 22% more induced power compared to two isolated single rotors, which was consistent with the theoretical findings of Leishman and Syal [7].

Additional claims that the lower rotor influences the performance of the upper rotor are expected but more difficult to quantify. The reasons given were because of the low axial separation distances between the upper and lower rotor, as a result of which the lower rotor operates in the downwash of the upper rotor, which was not yet fully developed. The performance characteristics showed similar trends when using twisted blades. However,

the extent to which the performance of the upper rotor becomes affected was not fully clear.

Cameron and Sirohi [16] measured the performance of a model coaxial rotor at the University of Texas. The rotor was tested at the Glen L. Martin Wind Tunnel at the University of Maryland, and featured 2-bladed upper and lower rotors with a radius of 1 m. The rotor blades were of uniform chord and untwisted along the span, and also used a VR-12 airfoil. This rotor was tested at several advance ratios and at lift offsets of up to 20% for fixed collective pitch angles of the upper rotor. The rotor system was trimmed for torque balance based on fixed collective pitch of the upper rotor. The rotor system was not trimmed for a constant thrust and hence the tests were not conducted in the manner consistent with the previously conducted experiments by Dingeldien. Nevertheless, results suggested that as the advance ratio increased the variation in lift-to-drag ratio was fairly small. However, because the rotor was not trimmed for a constant thrust, the usefulness of these results for validation purposes remains unclear.

Schmaus and Chopra [17] measured the performance of a coaxial rotor similar to the one used by Cameron and Sirohi. It was stated that all the measurements were taken at a physical shaft angle of 0° and the collective pitch of the lower rotor was adjusted to achieve a torque balance. It was found that the lower rotor produces more thrust than the upper rotor at high advance ratios. This outcome is quite unexpected because it has been well known from previous work that the upper rotor must produce more thrust for all flight conditions, which is because the lower rotor operates in the wake of the upper rotor and so results in

higher induced losses for a given thrust. The 0° shaft angle is also not a realistic operational state, and could be a reason for such an unexpected rotor behavior.

Cameron et al. [18] have studied coaxial rotor performance in hover. They also compared the performance of a coaxial rotor and an “equivalent” single rotor. Through these studies, the authors concluded that the coaxial configuration consumed 6% less power than a four-bladed rotor of equivalent solidity. They also compared the upper and lower rotors of a coaxial rotor with isolated rotors, and concluded that the upper and lower rotors consumed 18% and 49% more induced power, respectively, when in operation as a coaxial rotor system because of mutual interference.

1.3.2 Numerical Studies

A helicopter normally operates in under a wide range of flight regimes, i.e., hover, climb, descent and forward flight, as well as combinations of these basic flight conditions. Predicting the performance using mathematical models is very important, especially for design purposes. However, even with modern mathematical models, the prediction of coaxial rotor performance is not an easy task. The flow around a rotor is comprised of a complex, vortical wake structure, but even then the basic performance can be analyzed with good validity by using a relatively simple approach known as the Rankine-Froude momentum theory. The momentum theory is generally viewed as a first-order analysis to predict rotor thrust and performance, and is applicable to hover, climb and forward flight.

Other forms of rotor analysis are based on the blade element momentum theory (BEMT), which has good validity for hover and axial (climbing) flight. BEMT gives an improved

prediction of the various aerodynamic loads acting on the rotor blades, and total rotor performance is then found by spanwise integration. In the BEMT, the assumption is that each blade section is a quasi-2-dimensional airfoil section producing aerodynamic forces. A representation of quasi-3-dimensional effects can be introduced by including the so-called Prandtl tip loss effects [19]. In principle, the BEMT does not account for the mutual influence of the neighboring blade sections, however, unlike the simple momentum theory, the effects of non-uniform inflow are certainly accounted for. Like all blade element methods, the strength of the BEMT lies in rapid and accurate calculation of the induced velocities at each blade section. When the induced velocities are determined, then the forces and moments acting on the rotor can be obtained.

In 1951, Harrington applied the BEMT to predict the hovering performance of a coaxial rotor system based on an extension of the single rotor analysis [8]. The theoretical analysis for single and coaxial rotors was based on method described by Gessow [20]. In this analysis, the coaxial rotor was treated as a four-bladed single rotor and the blade section drag was predicted using a quadratic sectional 2-dimensional drag model. The calculated value of thrust was corrected for tip loss effects. The predictions were in good agreement with measurements but, it was stated that prior knowledge of zero-lift drag of the rotor is essential.

More recently, Leishman and Syal developed a series of figure of merit expressions for a coaxial rotor [7]. For the purpose of this study, four configurations of a coaxial rotor were studied using the BEMT. It was shown that for a coaxial rotor in torque balanced condition, the lower rotor has to operate in the fully developed slipstream of the upper rotor. The

induced loss was a maximum when the two rotors operated in the same plane at the torque balanced condition.

Leishman and Ananthan discussed the basis for developing an optimum coaxial rotor [21] using the BEMT and showed that the optimum blade twist for minimum induced losses is of double hyperbolic form with a break point in twist located at the point where the upper rotor wake impinges in the lower rotor. Additional claims were made that the upper and lower rotor of an optimum hovering coaxial rotor system must have different blade planforms if best overall performance is to be achieved.

It is clear that predicting the performance of a helicopter rotor is largely dependent on the ability to accurately predict the behavior of the rotor wake because it is the wake that mostly defines the net induced velocity field of a rotor. In 1995, Bagai and Leishman developed a new, robust numerical scheme that predicted the tip vortex geometry of a rotor wake, known as free-vortex method (FVM) [22]. This method was based on pseudo-implicit predictor-corrector relaxation scheme, with five-point central differencing for the wake equations that were derived using the principles of vorticity transport. This scheme showed very good comparisons with experimental results for both hover and forward flight regimes. Because of the pseudo-implicit nature, this scheme was computationally expensive compared to the single-step explicit methods. But the robustness of this scheme and much less susceptibility to numerical instabilities made it very usable for both single rotor and multi-rotor analysis.

In 2008, Syal used the FVM to study the performance of a coaxial rotor for the purposes of shape optimization of the rotor blades [23]. Parametric studies of inter-rotor spac-

ing, blade planform (taper) and separate amounts of blade twist on upper and lower rotors were conducted to study their effects. A formal optimization technique to maximize rotor performance in hover and forward flight was also discussed. This study showed that rotor performance improves if the rotor geometries of upper and lower rotor are different. It is also stated that rotor performance is independent of blade geometry at higher advance ratios because of the cleaner separation of the wakes from the upper and lower rotors.

Another method, the vorticity transport model (VTM), also better captures and preserves the vortex structure associated with wakes of a rotor [24, 25]. The VTM solves the vorticity-velocity form of Navier-Stokes equations on an Eulerian grid surrounding a rotor. It is a time-dependent computational solution that preserves the vortical structures from the adverse effects of numerical dissipation. The use of adaptive grid system to capture the vortex wake as it moves downstream makes VTM very useful for the purposes of coaxial rotor research. The VTM has previously been used to study performance of rotor-wake encounters [26, 27], rotors in ground effect [28, 29], and even the vortex ring state [30, 31]. Kim and Brown compared the performance of coaxial rotor and a conventional rotor using VTM [32]. The equivalent rotor geometry was, however, not adjusted so that the thrust sharing remains the same for conventional and coaxial rotors [33]. It was concluded that the coaxial system consumed less power than the “equivalent” single rotor in both hover and forward flight.

As previously mentioned, computational fluid dynamics (CFD) such as RANS is a more sophisticated approach to the problem of solving for the rotor aerodynamics. RANS methods eliminate the semi-empirical approximations associated with vortices, although

semi-empirical turbulence models are still required required. One such code that is used for the CFD analysis of a coaxial rotor is NASA's OVERFLOW 2. Ruzicka and Strawn [34] used OVERFLOW 2 for a coaxial rotor analysis using overset grids. In OVERFLOW 2, basically two types of grids were used, near-body and off-body grids. The grid attached to the rotor comprise the near-body grid and the automatically generated grid away from the solid surfaces is called the off-body grid. The inflow prior to 80% of rotor radius was overpredicted for the upper and lower rotor. Yoon et al. [35] also used OVERFLOW to analyze the interactional aerodynamics of a coaxial rotor in hover for next-generation autonomous drones. This approach showed that the performance of the coaxial does not become affected until the inter-rotor spacing is less than 50% of rotor radius.

Of the various numerical methods used for the purposes of coaxial research, none of them are an obvious choice for the purpose of the present study. While the BEMT is a parsimonious technique that gives rotor performance predictions, the inflow distributions are not captured as well as might be desired. FVM and CFD methods better predict the inflow distribution over the rotors, especially at the outboard blade sections where 3-dimensional effects are stronger. However, Juhasz et al. [36] showed that the net rotor performance predictions using BEMT compared well with experimental results, even better than those from the FVM and CFD.

The computational time required by each of these methods is also very different. While BEMT required negligible computational time on a modern computer, CFD requires almost 10^6 more units of computational time. Also, CFD methods do not preserve the wake structure associated with rotor flows, whereas FVM methods preserves the wake structure

indefinitely, and hence can be used for the purposes of coaxial research. Out of all the methodologies available, it was decided to use the FVM in the current study for the purposes of comparing a conventional and coaxial rotors, and also investigating the effects of inter-rotor spacing on performance.

1.4 Goals of the Present Work

The goals of the present work were to use the FVM to compare the aerodynamics of conventional and coaxial rotor configurations. The specific goals were to better understand the aerodynamic interactions between the two rotors of a coaxial helicopter. In summary, the objectives were:

1. To validate predictions made by a FVM by comparing against available experimental results for conventional and coaxial rotor configurations, and in both hover and in forward flight.
2. Compare the performance of a conventional rotor and a coaxial rotor in hover and forward flight. This study involved deriving an “equivalent” single rotor from a coaxial configuration.
3. To investigate the aerodynamic interference between the upper and lower rotors of a coaxial rotor in hover. This work involved examining the performance of the coaxial by means of parametric variations of inter-rotor spacing.
4. To quantify the degree of aerodynamic losses by comparing the performance of coaxial rotor system with isolated upper and lower rotors.

1.5 Outline of the Thesis

This thesis is divided into four chapters. The first chapter gives a background on coaxial rotor systems and the various aerodynamic concerns that are associated with their operation. Previous research into coaxial rotor systems is also discussed, along with the objectives for the current work. The second chapter discusses the FVM that solves for the rotor wake to calculate induced velocities at the rotor blades. This is followed by a discussion of the Maryland Free Wake (MFW) method developed at University of Maryland [37] and the specific methodology used in the present work to solve for the flow around a coaxial rotor system. The third chapter discusses the validation of the method and other results that were obtained during the process of the present study. The final chapter contains the conclusions drawn from the study, and also some recommendations for future research.

2. Methodology

This chapter discusses the free-vortex method (FVM) that was used to predict the flow field for a coaxial rotor helicopter system in both hovering flight and forward flight. The FVM is Lagrangian-based wake convection methodology, which solves for the evolution of the vortical wake produced by the rotor blades under the influence of an external flow. The vortical elements in the flow comprise of the rotor blades themselves, which are attached to and move with the blades (i.e., the so-called “bound” circulation), and the trailed vortex filaments, the latter which are free to move in the downstream wake under the influence of the local velocity field. The wake becomes “free” when the wake filaments reach equilibrium, force-free positions that are compatible with the bound circulation on the lifting blades at the desired operational state of the rotor(s). It is assumed that all of the vorticity in the flow field is confined to these free elements, and the flow everywhere else is inviscid, incompressible, and irrotational.

2.1 The Free-Vortex Wake Problem

The essence of the FVM is that it solves for the rotor wake geometry and also computes the strengths of the vortices trailed by the rotor blades at the desired flight conditions consistently with the lift on the blades. The blades lay down curved blade tip vortices, which are approximated by using interconnected straight line vortex filaments defined by

markers or collocation points, as shown in Fig. 5. Each vortex filament represents a trailed tip vortex, which is the dominant feature of the rotor wake flow [2]. The initial condition for the simulation is based on an undistorted rigid wake or a prescribed wake, which helps move the wake markers to positions that are closer to where they will ultimately end up. By means of the repeated application of the Biot-Savart law with a desingularized core, which also includes a vorticity diffusion model, the induced velocity field from all of the vortex filaments at any point in space can be calculated. The markers then move to new positions based on the local velocity field. The solution method is based either on time-stepping or relaxation method, and the wake solution proceeds until convergence is obtained, i.e., the wake becomes nominally periodic and repeats from rotor revolution to revolution. Previous studies have shown very good correlations can be obtained between the results of the FVM and measurements of the rotor wake and rotor performance such as thrust and power [22].

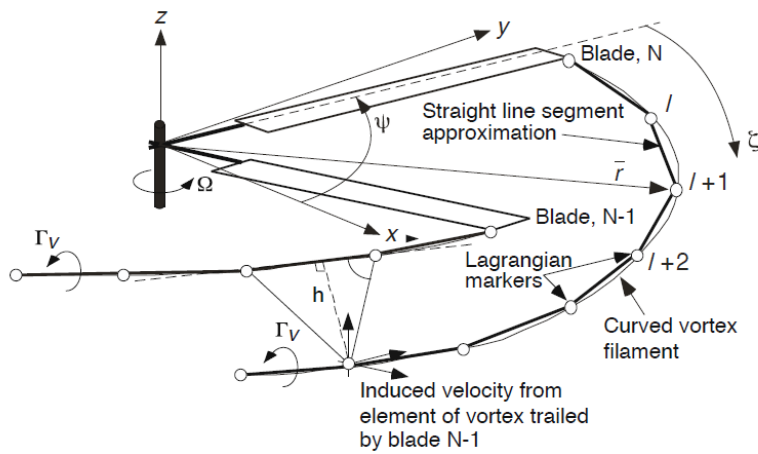


Fig. 5: Idealization of the curved rotor wake into straight line segments connected by collocation points [2].

The foundations of the FVM is based on the vorticity transport equation. It is assumed that the vorticity is confined to the vortices themselves and the flow outside is assumed to be inviscid. Under the conditions of inviscid, incompressible and irrotational flow, Helmholtz's law [38] states that the vortex lines move as material lines at the local flow velocities. The convection of points on these vortex lines is governed by

$$\frac{d}{dt}(\vec{\mathbf{r}}) = \mathbf{V}(\vec{\mathbf{r}}) \quad (2.1)$$

The vector $\vec{\mathbf{r}}$ in Eq. 2.1 gives the position of the Lagrangian markers in the vortical wake. In a blade fixed coordinate system, the left hand side of Eq. 2.1 can be expressed in terms of the rate of change of $\vec{\mathbf{r}}$ with blade azimuth ψ (temporal) and wake age ζ (spatial). Therefore, Eq. 2.1 can now be written in the following partial differential equation form

$$\frac{\partial \vec{\mathbf{r}}(\psi, \zeta)}{\partial \psi} + \frac{\partial \vec{\mathbf{r}}(\psi, \zeta)}{\partial \zeta} = \frac{1}{\Omega} \vec{\mathbf{V}}(\vec{\mathbf{r}}(\psi, \zeta)) \quad (2.2)$$

where Ω is the angular velocity of the rotor. The right-hand side of Eq. 2.2 is a non-linear source term that accounts for the net, instantaneous velocity of an element on the vortex filament.

Equation 2.2 cannot, in general, be solved analytically because of the highly non-linear terms on the right-hand side, and hence it has to be solved by numerical means. However, under the conditions of a uniform flow the equation can indeed be solved analytically [2], which results in a pure helical wake in hover and an epicycloidal wake in forward flight. The numerical integration requires two steps: First, define the source terms in terms of individual constituents; Second, discretize Eq. 2.2 into a finite number of finite difference equations.

The Source Terms

The net instantaneous velocity at a point $\vec{\mathbf{r}}(\psi, \zeta)$ is composed of the external or free-stream velocity and the net induced velocity at that location. This behavior can be denoted by

$$\vec{\mathbf{V}}(\vec{\mathbf{r}}(\psi, \zeta)) = \vec{\mathbf{V}}_\infty(\vec{\mathbf{r}}(\psi, \zeta)) + \vec{\mathbf{V}}_{ind}(\vec{\mathbf{r}}(\psi, \zeta)) \quad (2.3)$$

The free-stream component from forward and/or climbing and/or descending flight can be written as

$$\vec{\mathbf{V}}_\infty(\vec{\mathbf{r}}(\psi, \zeta)) = \mathbf{V}_{\infty x}\hat{i} + \mathbf{V}_{\infty y}\hat{j} + \mathbf{V}_{\infty z}\hat{k} \quad (2.4)$$

which is usually constant everywhere or at least uniform across the rotor.

The induced velocities from the vortices in the wake, however, are more difficult to determine because they are non-uniform and are determined by the application of Biot-Savart law, i.e.,

$$\begin{aligned} \vec{\mathbf{V}}_{ind}(\vec{\mathbf{r}}(\psi, \zeta)) &= \frac{1}{4\pi} \sum_{j=1}^{N_{V_f}} \int \frac{\Gamma_f(\psi_j, \zeta) d\vec{\zeta}_j \times (\vec{\mathbf{r}}(\psi, \zeta) - \vec{\mathbf{r}}_f(\psi_j, \zeta))}{|\vec{\mathbf{r}}(\psi, \zeta) - \vec{\mathbf{r}}_f(\psi_j, \zeta)|^3} \\ &+ \frac{1}{4\pi} \sum_{j=1}^{N_{V_b}} \sum_{i=1}^{i_{max}} \int \frac{\Gamma_b(\psi_j, \zeta) d\vec{l}_{j,i} \times (\vec{\mathbf{r}}(\psi, \zeta) - \vec{\mathbf{r}}_b(\psi_j, \zeta))}{|\vec{\mathbf{r}}(\psi, \zeta) - \vec{\mathbf{r}}_b(\psi_j, \zeta)|^3} \end{aligned} \quad (2.5)$$

where $\vec{\mathbf{r}}(\psi, \zeta)$ is the location of an element that is influenced by total contributions of the j^{th} free vortex located at $\vec{\mathbf{r}}_f(\psi_j, \zeta)$, of strength $\Gamma_f(\psi_j, \zeta)$, plus the influence of the i^{th} bound vortex of the j^{th} blade. The second term on the right-hand-side of Eq. 2.5 accounts for the i_{max} vortex segments from the N_{V_b} bound vortices on each blade, of strength, $\Gamma_b(\psi_j, \zeta)$. The bound vortices also straight are line segments, hence, the Biot-Savart law can be com-

puted analytically. Because the wake convects continuously, the Biot-Savart computations have to be reevaluated repeatedly until convergence of the wake solution is obtained [39].

2.2 Maryland Free Wake Method

The partial differential equation (PDE), Eq. 2.2, as discussed in the preceding section is difficult to solve even by numerical means, i.e., with a scheme that exhibits not only good accuracy and but also stability. The Maryland Free Wake (MFW), developed at the University of Maryland, is formulated to solve the PDE in Eq. 2.2 by using a special predictor-corrector method with spatial and temporal differencing. In summary, the formulation process is divided in to three steps.

1. Discretize the physical problem in space and time.
2. Transform the PDE in Eq. 2.2 in to a finite number of finite difference equations (FDE).
3. Develop numerically stable numerical integration schemes that are not only accurate (at least 2nd-order) but are also very stable.

These three steps will be discussed briefly in the following sections.

2.2.1 Discretization of the Physical Problem

The location of an element in the wake is given by $\vec{r}(\psi, \zeta)$, where ψ is the azimuth position and is, therefore, a time variable. The spatial variable, ζ is the angular location of an element on the wake that was trailed at azimuth location ψ . One rotor revolution is

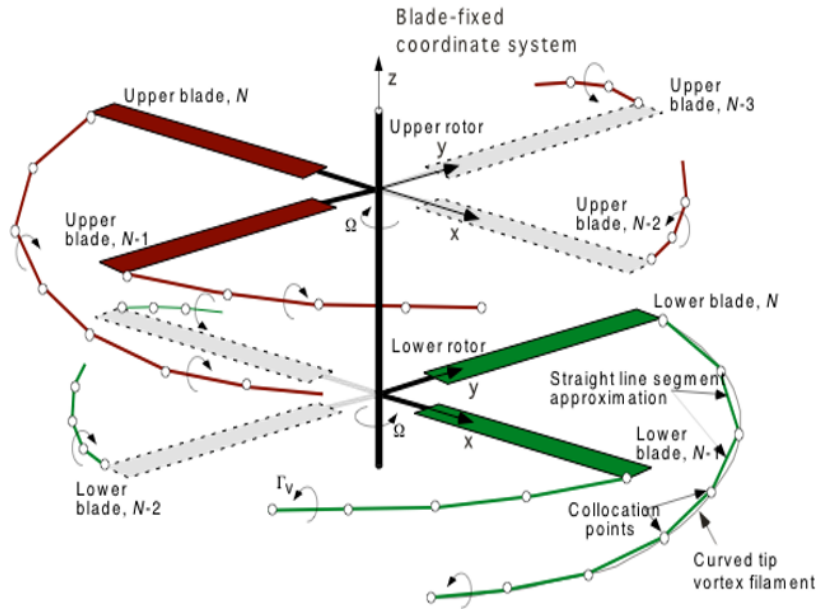


Fig. 6: Schematic showing the vortex wake of the coaxial rotor system [23].

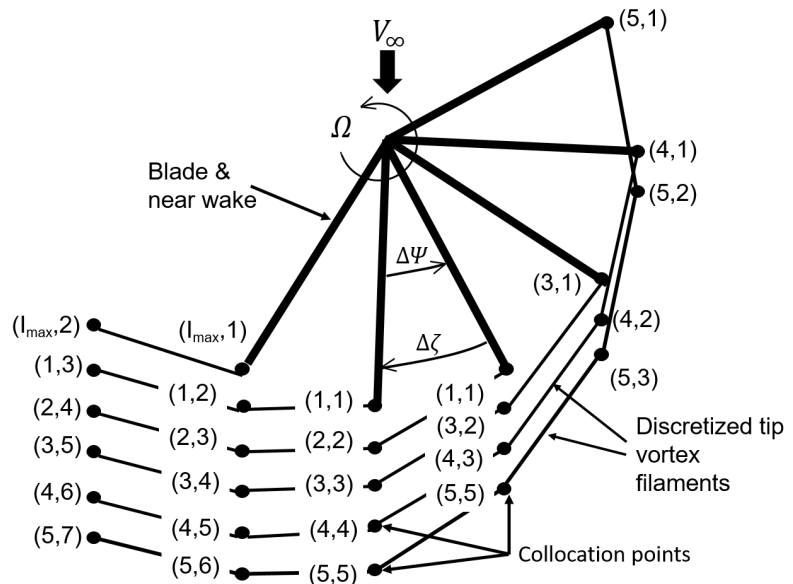


Fig. 7: Discretization of the rotor wake [39].

discretized into a finite number of points with a step size of $\Delta\psi$, and the trailed wake is divided into a finite number of straight line elements of $\Delta\zeta$ angular resolution. The vortex filaments are inter-connected through collocation points, as shown in Fig. 6. For ease of explanation, a single rotor wake discretized into a finite number of points is shown in Fig. 7.

2.2.2 Transformation of PDE

In the previous section, the first step for transforming the PDE in to FDE was discussed, i.e., discretization of the physical domain to a computational domain. The computational domain is shown in Fig. 8. The abscissa represents the ψ direction and the ordinate is in ζ coordinates. Recall that the PDE governing the rotor wake geometry is

$$\frac{\partial \vec{r}(\psi, \zeta)}{\partial \psi} + \frac{\partial \vec{r}(\psi, \zeta)}{\partial \zeta} = \frac{1}{\Omega} \vec{V}(\vec{r}(\psi, \zeta)) \quad (2.6)$$

To transform the Eq. 2.6 into a FDE, the partial derivatives for the terms on the left-hand-

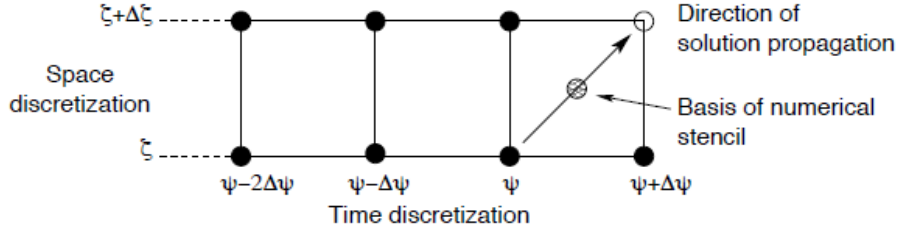


Fig. 8: Discretized computational domain [40].

side must approximated in terms of FDE's. The formulation of MFW is based on 5-point central differencing scheme and the computational stencil is shown in Fig. 8. The MFW algorithm solves Eq. 2.6 by using the predictor-corrector 2nd-order backward difference

(PC2B) approach that was developed by Bhagwat [41]. Using the PC2B approach, the FDE's for the two terms on the left-hand-side of Eq.2.6 are written as

$$\frac{\partial \vec{r}}{\partial \psi} = \frac{3\mathbf{r}(\psi + \Delta\psi, \zeta) - \mathbf{r}(\psi, \zeta) - 3\mathbf{r}(\psi - \Delta\psi, \zeta) + \mathbf{r}(\psi - 2\Delta\psi, \zeta)}{4\Delta\psi} \quad (2.7)$$

$$\frac{\partial \vec{r}}{\partial \zeta} = \frac{\mathbf{r}(\psi + \Delta\psi, \zeta + \Delta\zeta) + \mathbf{r}(\psi, \zeta + \Delta\zeta) - \mathbf{r}(\psi + \Delta\psi, \zeta) - \mathbf{r}(\psi, \zeta)}{2\Delta\zeta} \quad (2.8)$$

Equations 2.7 and 2.8 are at the midpoint of the grid cell, i.e., at $\vec{r}(\psi + \Delta\psi/2, \zeta + \Delta\zeta/2)$.

Also, Eq 2.7 shows that the PC2B approach uses points from the previous three time steps to evaluate the solution at the new time step. In Eq. 2.6, the velocity term at point $\vec{r}(\psi + \Delta\psi/2, \zeta + \Delta\zeta/2)$ is averaged using the neighboring four points and can be written as

$$\vec{V}\left(\vec{r}(\psi + \Delta\psi/2, \zeta + \Delta\zeta/2)\right) = \frac{1}{4} \left(\vec{V}(\psi, \zeta) + \vec{V}(\psi + \Delta\psi, \zeta) + \vec{V}(\psi + \Delta\psi, \zeta - \Delta\zeta) + \vec{V}(\psi, \zeta - \Delta\zeta) \right) \quad (2.9)$$

Substituting Eqs. 2.7, 2.8 and 2.9 into Eq. 2.6 and simplifying, the position of $\vec{r}(\psi, \zeta)$ is written as

$$\begin{aligned} \vec{r}(\psi, \zeta) = & \frac{\vec{r}(\psi + \Delta\psi, \zeta)}{5} + \frac{3\vec{r}(\psi - \Delta\psi, \zeta)}{5} - \frac{\vec{r}(\psi - 2\Delta\psi, \zeta)}{5} \\ & - \frac{4\vec{r}(\psi + \Delta\psi, \zeta + \Delta\zeta)}{5} - \frac{4\vec{r}(\psi, \zeta + \Delta\zeta)}{5} + \frac{1}{10\Omega} \left(\vec{V}(\psi, \zeta) \right. \\ & \left. + \vec{V}(\psi + \Delta\psi, \zeta) + \vec{V}(\psi + \Delta\psi, \zeta - \Delta\zeta) + \vec{V}(\psi, \zeta - \Delta\zeta) \right) \end{aligned} \quad (2.10)$$

because the results discussed are for a uniform grid, i.e., for $\Delta\psi = \Delta\zeta$, the equation for the position of $\vec{r}(\psi, \zeta)$ reduces to Eq. 2.10. The PC2B method that solves Eq. 2.10 is discussed in the following section.

2.2.3 Numerical Integration Scheme

The solution to the FDE in Eq. 2.10 is governed by the non-linear velocity terms on the right-hand side and must be computed for all collocation points in the rotor wake. Solving the equation involves the following steps:

1. Compute the source terms at each collocation point from the instantaneous contributions of the N_v vortices in the wake trailed from the N_b blades.
2. Update the position vectors of all collocation points by solving Eq. 2.10 until the root-mean-square value of the change in wake displacements (i.e., the L_2 norm) drops below a prescribed criterion, which is approximately 10^{-4} .

The predictor step computes an approximate geometry at the new time step. Using the updated wake geometry, the source terms are re-computed. The corrector step then uses a weighted average of the velocities from the predictor step, and solves the equation to determine the wake geometry at this new time step.

2.2.4 Blade Aerodynamic Model

The rotor comprises of N_b rotor blades, which are assumed to be rigid, but must be allowed to exhibit free flapping motion about a hinge in a time-accurate manner. The blade aerodynamic model implemented in the MFW is based on the Weissinger-L model [42]; see Fig. 9. Each rotor blade is divided into N_s segments and the blade bound circulation is fixed at 1/4-chord and the blade control points are located at 3/4-chord location. While the lift and bound vortex strengths are constant along any section, it varies from one section

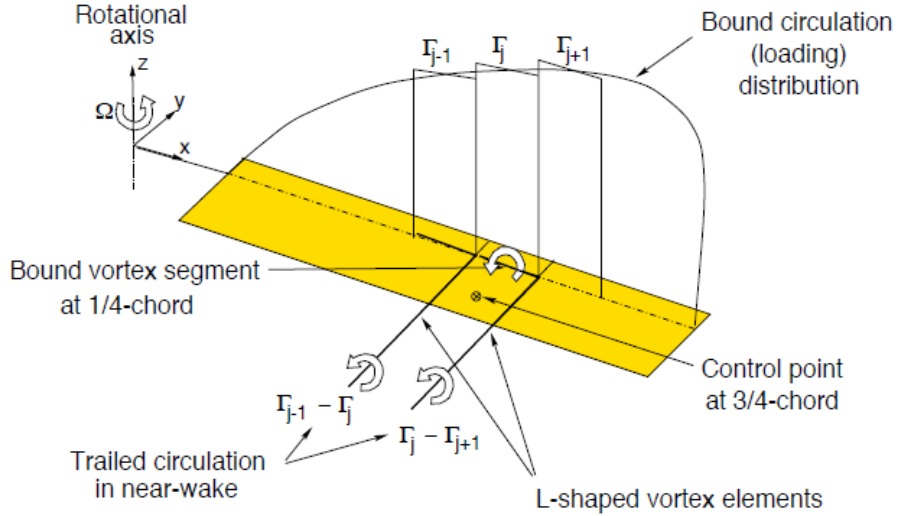


Fig. 9: Schematic of the Weissinger-L model [23].

to another. Consequently, vorticity has to be trailed at the end of each segment, and the strength of this trailed vorticity is determined using Helmholtz laws of conservation of vorticity, see Eq. 2.11, i.e.

$$\Gamma_{t_j} = \Gamma_{b_j} - \Gamma_{b_{j+1}} \quad (2.11)$$

The trailed vorticity is modeled as a planar sheet fixed to the rotor blade for a fixed angular distance, $\Delta\psi$. The unsteady effects from shed vorticity are included using indicial response functions [40]. Because of the need to impose flow tangency, the component of incident velocity perpendicular to the blade segment at 3/4th-chord position is exactly zero, i.e.,

$$\mathbf{V}_i \cdot \bar{n}_i = 0 \quad i = 1, 2, \dots, N_s \quad (2.12)$$

where the incident velocity, \mathbf{V}_i is from the free stream, the bound vortices, the trailed vortices, etc., and is written as

$$\mathbf{V}_i = \mathbf{V}_\infty + \mathbf{V}_{FW} + \mathbf{V}_B + \mathbf{V}_{NW} \quad (2.13)$$

In Eq. 2.13, \mathbf{V}_{FW} is computed by application of the the Biot-Savart law. \mathbf{V}_B and \mathbf{V}_{NW} depend on the bound circulation strength, Γ_j , and the influence coefficient matrix, I , i.e.,

$$\mathbf{V}_{B_i} = \sum_{j=1}^{N_s} I_{B_{ij}} \Gamma_j \quad (2.14)$$

$$\mathbf{V}_{NW_i} = \sum_{j=1}^{N_s} I_{NW_{ij}} \Gamma_j \quad (2.15)$$

where $I_{B_{ij}}$ and $I_{NW_{ij}}$ are the influence coefficient matrices for the bound vorticity and near wake respectively. Substituting Eqs. 2.14 and 2.15 into Eq. 2.12 and rearranging gives

$$\Gamma_j = [I]^{-1} \{(\mathbf{V}_\infty + \mathbf{V}_{FW}) \cdot \bar{n}\}_i \quad (2.16)$$

The strength of the bound vortex is determined by solving Eq. 2.16. Using this approach, the lift at each part of the blade is by determined by applying the Kutta-Joukowski theorem as

$$L = \rho U \Gamma_j \quad (2.17)$$

The previous version of the MFW used Beddoes's two-dimensional, non-linear airfoil model [43] to compute airfoil coefficients. During validation, it was found that the predicted power did not match well with measurements for the coaxial rotor. Therefore, a airfoil table lookup method was used to determine lift and drag coefficients for the symmetric NACA 0012 airfoil, which are shown in Fig. 10.

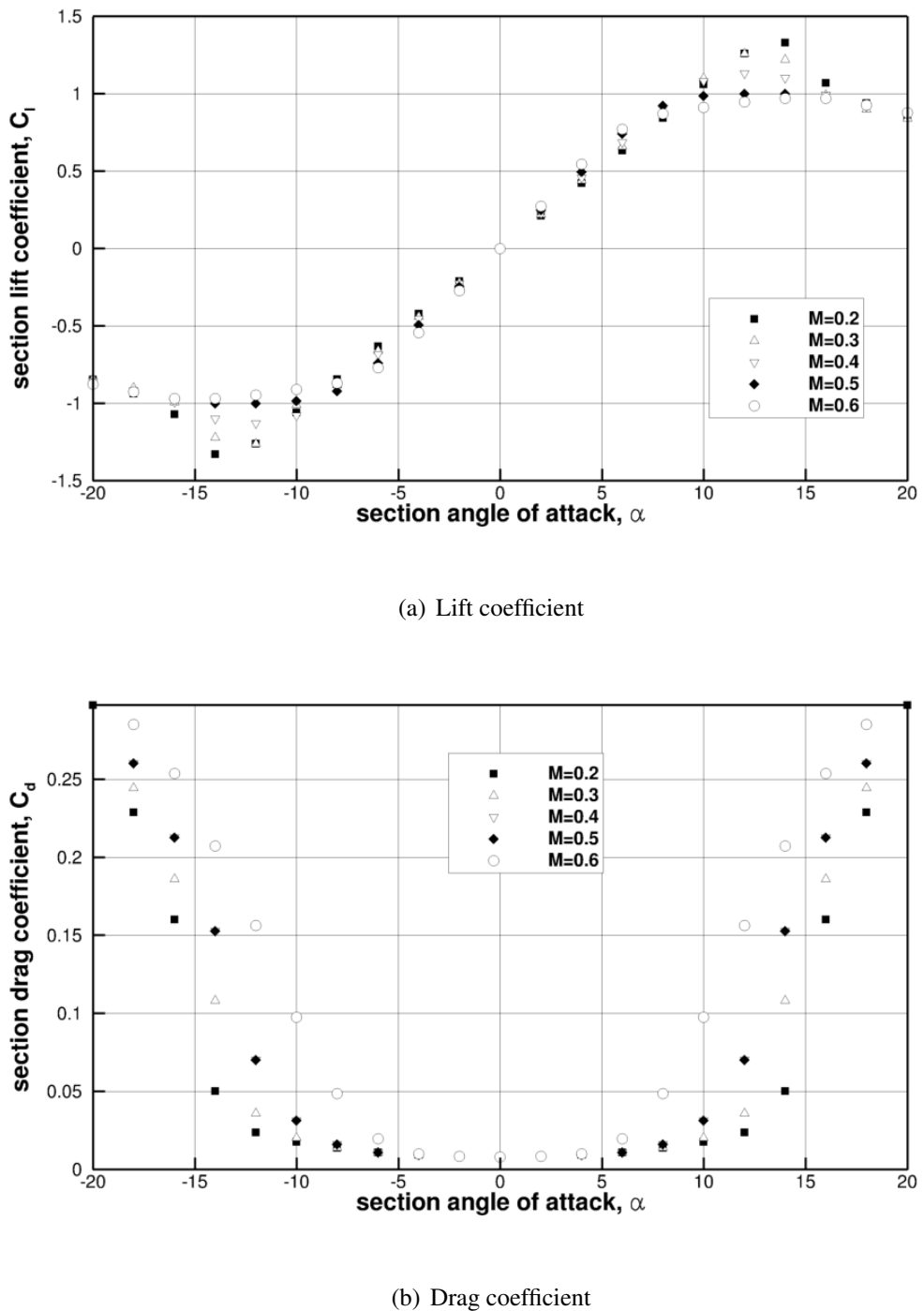


Fig. 10: Airfoil coefficients for the NACA 0012.

The blade flapping is dependent on the aerodynamic response, which in-turn is depends on the wake solution. Also, the blade wake attachment boundary condition necessitates the coupling between rotor wake and blade flapping. The flapping equation for a rigid blade is written as

$$\ddot{\beta} + v_\beta^2 \beta = \frac{M_\beta}{I_\beta \Omega^2} \quad (2.18)$$

where v_β is the natural flap frequency, I_β represents blade moment of inertia about the flapping hinge. Writing Eq. 2.18 as a set of ordinary differential equations in matrix form [40] we have

$$\frac{d}{d\psi} \begin{Bmatrix} \dot{\beta} \\ \beta \end{Bmatrix} + \begin{bmatrix} v_\beta^2 & 0 \\ 0 & 1 \end{bmatrix} \begin{Bmatrix} \dot{\beta} \\ \beta \end{Bmatrix} = \begin{Bmatrix} \frac{M_\beta}{I_\beta \Omega^2} \\ 0 \end{Bmatrix} \quad (2.19)$$

Eq. 2.19 is solved using PC2B scheme [41].

2.3 Rotor Trim Methodology

The aerodynamic response of a helicopter rotor is a highly coupled function of the control input angles (collective and cyclic pitch) and the resulting aerodynamic forces on the rotor. The changes in the collective and cyclic pitch inputs also affect the blade flapping. Trimming a helicopter rotor is essential to maintain a balance of aerodynamic forces and also to compare the results of the wake solutions at various flight conditions. The trim methodology employed in the FVM is based on a Newton-Raphson approach [40].

Single Rotor Trim Methodology

The control input vector of a rotor blade, \mathbf{x} , comprises of the pilot control inputs which are the blade collective θ_0 , the lateral cyclic, θ_{1c} , and the longitudinal cyclic, θ_{1s} . The control input vector (i.e., $\mathbf{x} = \{\theta_0, \theta_{1c}, \theta_{1s}\}^T$) is updated during the trim procedure using the Newton-Raphson approach, which solves the rotor aerodynamic environment to obtain the desired rotor response \mathbf{y} , which comprises the conditions for thrust and TPP orientation. The rotor response vector is written as, $\mathbf{y} = \{C_T, \beta_{1c}, \beta_{1s}\}^T$.

The Taylor series for the rotor response as a function of the input is written as

$$\mathbf{y}(\mathbf{x} + \Delta\mathbf{x}) = \mathbf{y}(\mathbf{x}) + [J]\Delta\mathbf{x} + \dots \quad (2.20)$$

where $\mathbf{y}(\mathbf{x} + \Delta\mathbf{x})$ is the rotor response to the new control input $(\mathbf{x} + \Delta\mathbf{x})$. Rearranging the terms of Eq. 2.20 we get

$$\Delta\mathbf{x} = [J]^{-1} \{ \mathbf{y}(\mathbf{x} + \Delta\mathbf{x}) - \mathbf{y} \} \quad (2.21)$$

where $\mathbf{y}(\mathbf{x} + \Delta\mathbf{x})$ is the response error vector which is written as

$$\mathbf{y}(\mathbf{x} + \Delta\mathbf{x}) - \mathbf{y} = \begin{Bmatrix} C_T - C_{T_{req}} \\ \beta_{1c} \\ \beta_{1s} \end{Bmatrix} \quad (2.22)$$

where $C_{T_{req}}$ is the target total system thrust and β_{1c} and β_{1s} are the lateral and longitudinal TPP tilt. The Jacobian matrix, \mathbf{J} is written as

$$\mathbf{J} = \frac{\partial \mathbf{y}}{\partial \mathbf{x}} = \begin{bmatrix} \frac{\partial C_T}{\partial \theta_0} & \frac{\partial C_T}{\partial \theta_{1c}} & \frac{\partial C_T}{\partial \theta_{1s}} \\ \frac{\partial \beta_{1c}}{\partial \theta_0} & \frac{\partial \beta_{1c}}{\partial \theta_{1c}} & \frac{\partial \beta_{1c}}{\partial \theta_{1s}} \\ \frac{\partial \beta_{1s}}{\partial \theta_0} & \frac{\partial \beta_{1s}}{\partial \theta_{1c}} & \frac{\partial \beta_{1s}}{\partial \theta_{1s}} \end{bmatrix} \quad (2.23)$$

Substituting Eqs. 2.22 and 2.23 in Eq. 2.21 gives

$$\Delta \mathbf{x} = [\mathbf{J}]^{-1} \begin{Bmatrix} C_T - C_{T_{req}} \\ \beta_{1c} \\ \beta_{1s} \end{Bmatrix} \rightarrow 0 \quad (2.24)$$

The trim cycle begins with an initial guess and is later updated by solving Eq. 2.24. The Jacobian would be a diagonal matrix but because of aerodynamic coupling it is actually fully populated. The partial derivatives in Eq. 2.23 are computed using first-order forward difference approximation. The updated response is then used to re-calculate the Jacobian matrix; this latter calculation is computationally expensive and is calculated only when needed during the trim procedure.

Coaxial Rotor Trim Methodology

The aerodynamics of a coaxial rotor is more complicated because of the intermingling of the rotor wakes and hence the rotor trim process is not straightforward because the two rotors need to be trimmed simultaneously. Although the total system thrust is a sum of the thrusts carried by the upper and lower rotors, they do not share the thrust equally i.e., $C_T^u \neq C_T^l$. The control inputs for the upper and lower rotor are interdependent, and hence the trim of a coaxial rotor is a highly coupled problem.

One of the advantages of the coaxial rotor is the absence of a dedicated anti-torque system because two rotors of the coaxial rotor must operate at equal and balanced torques; because the upper and lower rotor are counter-rotating with respect to each the resultant

torque of the system is zero. Also the orientation of the TPP is a necessary trim condition, as it is for a single rotor.

The control input and the response vector of a coaxial rotor can be written as

$$\mathbf{x} = \begin{Bmatrix} \theta_0^u \\ \theta_{1c}^u \\ \theta_{1s}^u \\ \theta_0^l \\ \theta_{1c}^l \\ \theta_{1s}^l \end{Bmatrix} \quad \text{and} \quad \mathbf{y} = \begin{Bmatrix} \Sigma C_T \\ \Sigma C_Q \\ \beta_{1c}^u \\ \beta_{1s}^u \\ \beta_{1c}^l \\ \beta_{1s}^l \end{Bmatrix} \quad (2.25)$$

In Eq. 2.25, the superscripts u and l indicate the upper and lower rotor respectively. The rotor response is a function of the control input, hence Eq. 2.21 is applicable to the coaxial system. The Jacobian for the coaxial system is written as

$$\mathbf{J} = \frac{\partial \mathbf{y}}{\partial \mathbf{x}} = \left[\begin{array}{cccccc} \frac{\partial \Sigma C_T}{\partial \theta_0^u} & \frac{\partial \Sigma C_T}{\partial \theta_{1c}^u} & \frac{\partial \Sigma C_T}{\partial \theta_{1s}^u} & \frac{\partial \Sigma C_T}{\partial \theta_0^l} & \frac{\partial \Sigma C_T}{\partial \theta_{1c}^l} & \frac{\partial \Sigma C_T}{\partial \theta_{1s}^l} \\ \frac{\partial \Sigma C_Q}{\partial \theta_0^u} & \frac{\partial \Sigma C_Q}{\partial \theta_{1c}^u} & \frac{\partial \Sigma C_Q}{\partial \theta_{1s}^u} & \frac{\partial \Sigma C_Q}{\partial \theta_0^l} & \frac{\partial \Sigma C_Q}{\partial \theta_{1c}^l} & \frac{\partial \Sigma C_Q}{\partial \theta_{1s}^l} \\ \frac{\partial \beta_{1c}^u}{\partial \theta_0^u} & \frac{\partial \beta_{1c}^u}{\partial \theta_{1c}^u} & \frac{\partial \beta_{1c}^u}{\partial \theta_{1s}^u} & \frac{\partial \beta_{1c}^u}{\partial \theta_0^l} & \frac{\partial \beta_{1c}^u}{\partial \theta_{1c}^l} & \frac{\partial \beta_{1c}^u}{\partial \theta_{1s}^l} \\ \frac{\partial \theta_0^u}{\partial \theta_0^u} & \frac{\partial \theta_{1c}^u}{\partial \theta_{1c}^u} & \frac{\partial \theta_{1s}^u}{\partial \theta_{1s}^u} & \frac{\partial \theta_0^l}{\partial \theta_0^l} & \frac{\partial \theta_{1c}^l}{\partial \theta_{1c}^l} & \frac{\partial \theta_{1s}^l}{\partial \theta_{1s}^l} \\ \frac{\partial \beta_{1s}^u}{\partial \theta_0^u} & \frac{\partial \beta_{1s}^u}{\partial \theta_{1c}^u} & \frac{\partial \beta_{1s}^u}{\partial \theta_{1s}^u} & \frac{\partial \beta_{1s}^u}{\partial \theta_0^l} & \frac{\partial \beta_{1s}^u}{\partial \theta_{1c}^l} & \frac{\partial \beta_{1s}^u}{\partial \theta_{1s}^l} \\ \frac{\partial \theta_0^u}{\partial \theta_0^u} & \frac{\partial \theta_{1c}^u}{\partial \theta_{1c}^u} & \frac{\partial \theta_{1s}^u}{\partial \theta_{1s}^u} & \frac{\partial \theta_0^l}{\partial \theta_0^l} & \frac{\partial \theta_{1c}^l}{\partial \theta_{1c}^l} & \frac{\partial \theta_{1s}^l}{\partial \theta_{1s}^l} \\ \frac{\partial \beta_{1c}^l}{\partial \theta_0^u} & \frac{\partial \beta_{1c}^l}{\partial \theta_{1c}^u} & \frac{\partial \beta_{1c}^l}{\partial \theta_{1s}^u} & \frac{\partial \beta_{1c}^l}{\partial \theta_0^l} & \frac{\partial \beta_{1c}^l}{\partial \theta_{1c}^l} & \frac{\partial \beta_{1c}^l}{\partial \theta_{1s}^l} \\ \frac{\partial \theta_0^l}{\partial \theta_0^u} & \frac{\partial \theta_{1c}^l}{\partial \theta_{1c}^u} & \frac{\partial \theta_{1s}^l}{\partial \theta_{1s}^u} & \frac{\partial \theta_0^l}{\partial \theta_0^l} & \frac{\partial \theta_{1c}^l}{\partial \theta_{1c}^l} & \frac{\partial \theta_{1s}^l}{\partial \theta_{1s}^l} \\ \frac{\partial \beta_{1s}^l}{\partial \theta_0^u} & \frac{\partial \beta_{1s}^l}{\partial \theta_{1c}^u} & \frac{\partial \beta_{1s}^l}{\partial \theta_{1s}^u} & \frac{\partial \beta_{1s}^l}{\partial \theta_0^l} & \frac{\partial \beta_{1s}^l}{\partial \theta_{1c}^l} & \frac{\partial \beta_{1s}^l}{\partial \theta_{1s}^l} \\ \frac{\partial \theta_0^l}{\partial \theta_0^u} & \frac{\partial \theta_{1c}^l}{\partial \theta_{1c}^u} & \frac{\partial \theta_{1s}^l}{\partial \theta_{1s}^u} & \frac{\partial \theta_0^l}{\partial \theta_0^l} & \frac{\partial \theta_{1c}^l}{\partial \theta_{1c}^l} & \frac{\partial \theta_{1s}^l}{\partial \theta_{1s}^l} \end{array} \right] \quad (2.26)$$

The perturbed input vector for the coaxial system is written as

$$\Delta \mathbf{x} = [\mathbf{J}]^{-1} \left\{ \begin{array}{c} \sum C_T - C_{T_{req}} \\ \sum C_Q \\ \beta_{1c}^u \\ \beta_{1s}^u \\ \beta_{1c}^l \\ \beta_{1s}^l \end{array} \right\} \rightarrow 0 \quad (2.27)$$

where $C_{T_{req}}$ denotes target system thrust and $\sum C_Q$ denotes the net system torque. β_{1c}^u and β_{1s}^u are the lateral and longitudinal tilt of the TPP for the upper rotor respectively. β_{1c}^l and β_{1s}^l are the lateral and longitudinal tilt of the TPP for the lower rotor respectively. The TPP is kept perpendicular to the rotor shaft by ensuring that the values of β_{1c}^u , β_{1s}^u , β_{1c}^l and β_{1s}^l are zero at the end of the trim process.

The trim cycle begins with initial guesses for the control input vector \mathbf{x} , which is used to compute rotor response \mathbf{y} . Using \mathbf{x} and \mathbf{y} the Jacobian, \mathbf{J} for the rotor is computed. Using Eq. 2.21, the necessary perturbation to achieve rotor trim can be obtained. This trim cycle is repeated until all the elements of the response vector are zero.

3. Results and Discussion

3.1 Validation

The results obtained from the FVM were validated by comparing with measurements conducted on three sets of single and coaxial rotor configurations. Two sets of coaxial rotors used for the purpose of validation were the rotors used by Harrington [8]. These two rotor sets were referred to as Harrington 1 and Harrington 2 rotors for convenience. Both the rotor sets comprised of untwisted blades and had the same radius, however, the Harrington 1 rotor blades were tapered in planform and thickness with a rotor solidity of 0.027 per disk. The Harrington 2 rotor blades were tapered in thickness only with a rotor solidity of 0.076 per disk. The rotors used symmetric NACA airfoils; the FVM is a lifting line model so that it does not explicitly take into consideration the varying thickness along the span, this being done from the perspective of the airfoil section data. In the present work, the airfoil coefficients were derived from generic NACA 0012 airfoil tables.

Another rotor that was used for the purpose of validation was the one used by Cameron and Sirohi at The University of Texas [16]. This rotor is a small-scale, 2-bladed coaxial rotor of radius 1 m; the blades were untwisted, with uniform planform and solidity of 0.05 per rotor disk. The blades used VR-12 airfoil section with a trailing edge tab. The detailed rotor geometries for the three coaxial rotor systems are in Tables A.1, A.2 and A.3.

The following sections discuss the validation of the FVM by comparing predictions with existing experimental data that was obtained from tests conducted on the three rotors. All the results discussed are for a given system thrust, zero net torque for the coaxial system, and the rotor tip-path-plane (TPP) orientation is maintained perpendicular to rotor shaft. Also, for forward flight, the shaft angle was adjusted so that the propulsive force is same for the rotor systems being compared.

3.1.1 Harrington Rotors

Harrington 1

In this section, the results obtained from the FVM are compared with the experimental results of Harrington, a schematic of the blade planform being shown in Fig. 11. To account

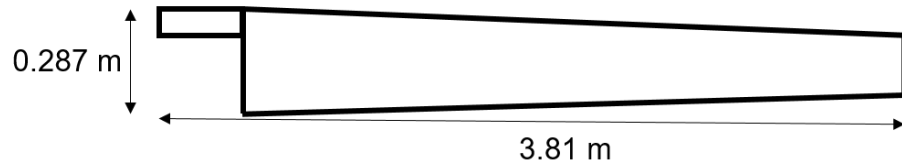


Fig. 11: Rotor blade shape of Harrington 1 rotor.

for the varying thickness of the blade, the average zero thrust profile drag *i.e.* C_{d0} was adjusted to 0.00904 using airfoil measurements. The zero-lift sectional drag coefficient for the NACA symmetric series can be approximated by the equation

$$C_{d0} \approx 0.007 + 0.025 \left(\frac{t}{c} \right) \quad (3.1)$$

where t/c is the thickness-to-chord ratio. The result is valid in the range $0.06 \leq t/c \leq 0.24$, which is in the range used on the Harrington 1 rotor. The effects of Mach number compound the behavior of the drag, but at moderate angles of attack below the drag divergence Mach number the effects of compressibility are small.

If the blade tapers in thickness from an airfoil with a 24% thickness-to-chord ratio at the root to a 6% ratio at the tip then the drag coefficient can be written as

$$C_{d_0}(r) = 0.007 + 0.025(0.24 - 0.18r) = 0.013 - 0.0045r. \quad (3.2)$$

The profile power coefficient can now be estimated using the blade element model where

$$C_{P_0} = \frac{1}{2}\sigma \int_0^1 C_{d_0} r^3 dr = \frac{1}{2}\sigma \int_0^1 (0.013 - 0.0045r) r^3 dr \quad (3.3)$$

Evaluation of this expression gives a value of $\frac{1}{8}\sigma(0.00904)$ compared to the value $\frac{1}{8}\sigma(0.013)$ without the use of thickness. In the FVM, the drag coefficient from lookup table is about 0.008 which would give profile power coefficient of $\frac{1}{8}\sigma(0.008)$, which did not predict the C_{P_0} accurately when compared to measurements in Fig. 12. Using the method described above the drag coefficient was adjusted by adding 0.00104 to the value obtained from the lookup table. This ensured that the FVM predictions for C_{P_0} were similar to measurements.

The predicted power polar for the Harrington 1 rotor is shown in Fig. 12. The power predictions made by the FVM are in reasonable agreement with the measurements. Predictions for the single rotor agree very well with the measurements, however there is a slight overprediction in power for the coaxial rotor system. The coaxial rotor did not trim for higher system thrust values and therefore the results were not available.

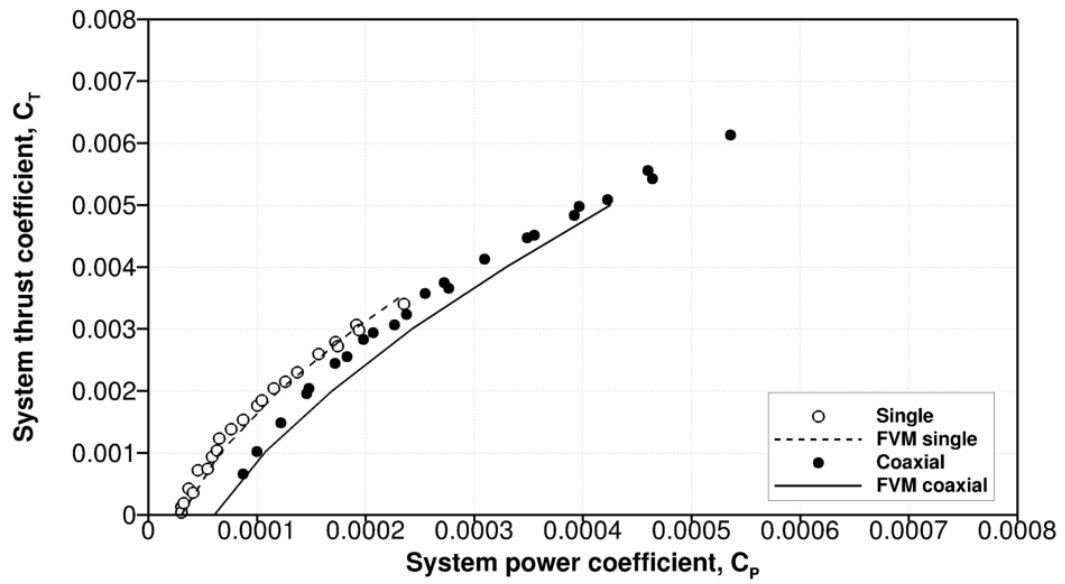


Fig. 12: Power polar for the Harrington 1 rotor.

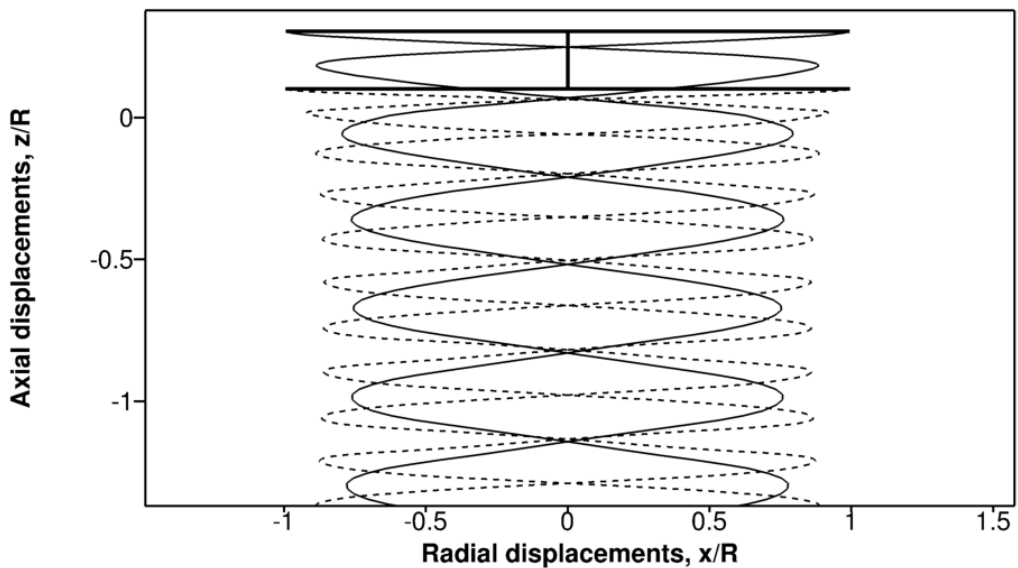


Fig. 13: Wake geometry of the Harrington 1 rotor in hover at $C_T = 0.004$.

Figure 13 shows the predicted wake geometry for the Harrington 1 rotor that was obtained using the FVM. The wake geometry that is plotted is time history of tip vortices released at different azimuth locations by the upper and lower rotors. The two wakes interact without significantly distorting the helical structure of the wake. Notice that the wake from the upper rotor has a different helical pitch than the lower rotor, confirming the operation at different thrusts and also an interaction between the two wakes. Because the experiment conducted by Harrington did not measure the wake geometry, there are no wake data for comparison. However, the wake structure is consistent with the flow visualization experiments conducted by Taylor [44] and McAlister et al [45].

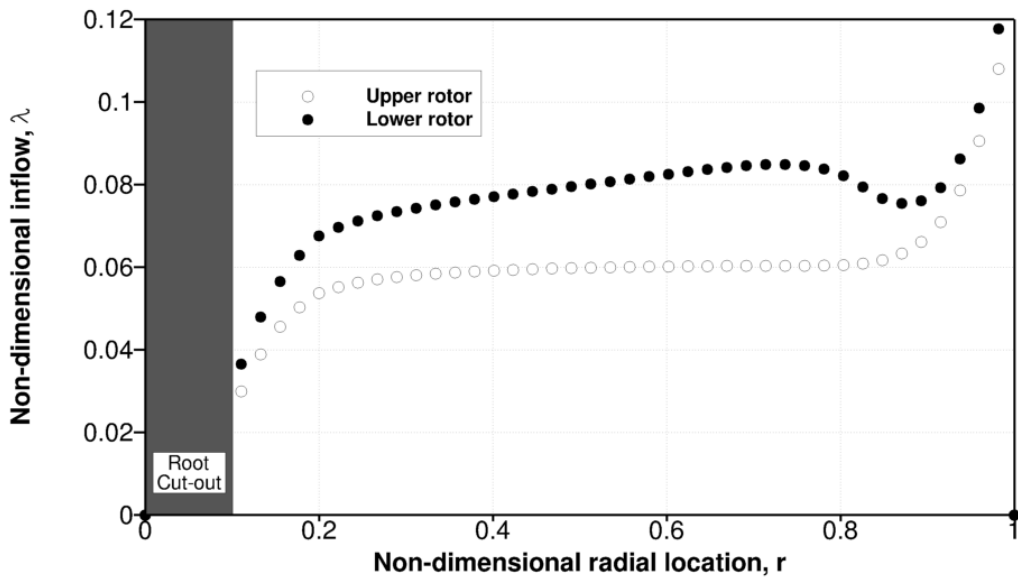


Fig. 14: Predicted inflow ratio distribution of the upper and lower rotors for the Harrington 1 rotor in hover at $C_T = 0.004$.

Figure 14 shows the predicted inflow ratio across the upper and lower rotors. The plot is an average of the inflow ratio along the mid-span for one rotor revolution. The inflow ratio is fairly uniform across the span of the upper rotor. However, the inflow across the lower rotor is distinctly different. The effects of the wake from the upper rotor impinge on the lower rotor, which can be clearly seen at about 80% of the blade span. At this point, the inflow ratio is higher on the inboard sections of the lower rotor compared to the inboard sections of the upper rotor, but then abruptly drops to a lower value, and eventually equaling the inflow ratio across the upper rotor near the blade tip. Consequently the upper rotor carries higher thrust compared to the lower rotor when operated at a torque trim condition.

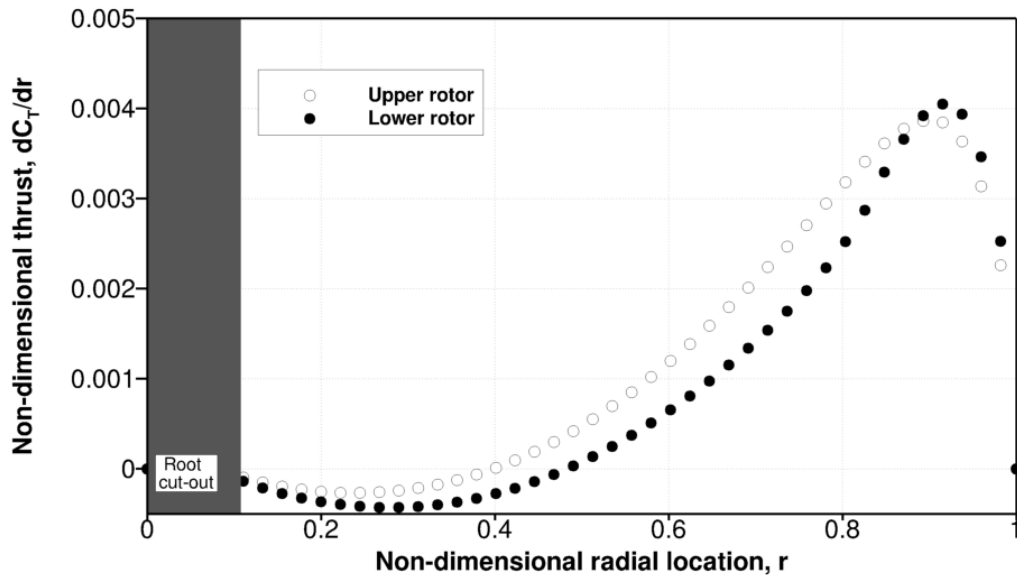


Fig. 15: Predicted spanwise distribution of thrust on the upper and lower rotors for the Harrington 1 rotor in hover at $C_T = 0.004$.

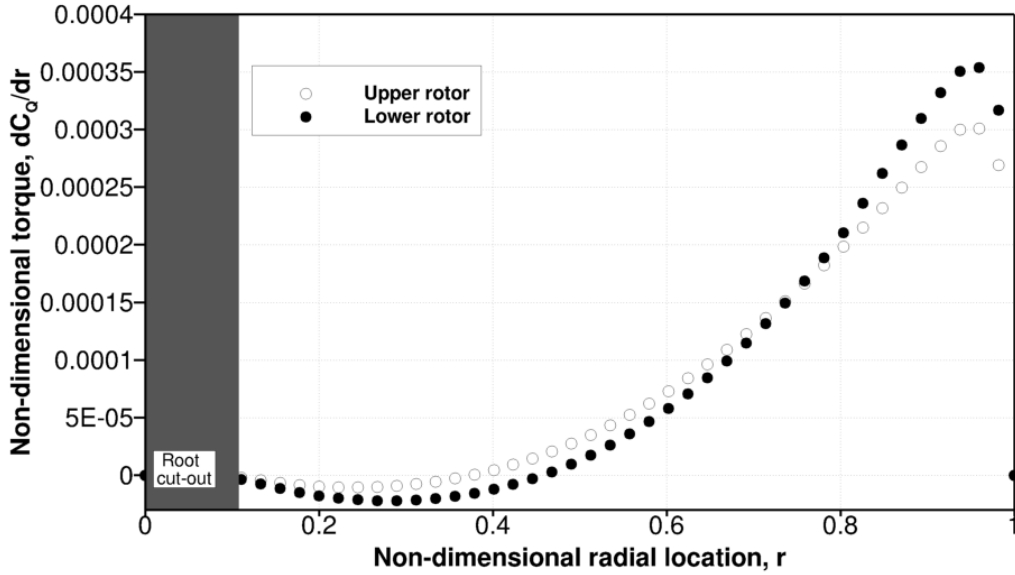


Fig. 16: Predicted spanwise distribution of torque on the upper and lower rotors for the Harrington 1 rotor in hover at $C_T = 0.004$.

Figure 15 shows the spanwise thrust on the upper and lower rotors. Over the inboard section, the upper rotor carries more thrust because of the lower inflow across the inboard sections of the upper rotor, whereas in the outboard sections notice that the sectional thrust for the upper and lower rotors is almost equal.

Figure 16 shows the corresponding predicted spanwise distribution of torque across the upper and lower rotors of the Harrington 1 rotor. Because the coaxial rotor system is at a torque balanced condition, the area under the curves is equal.

Figure 17 shows the lift distribution across the span of the upper and lower rotors of the Harrington 1. Notice that the lower rotor has a lower coefficient of lift than the upper rotor in the inboard sections. This outcome is because the downwash from the upper rotor

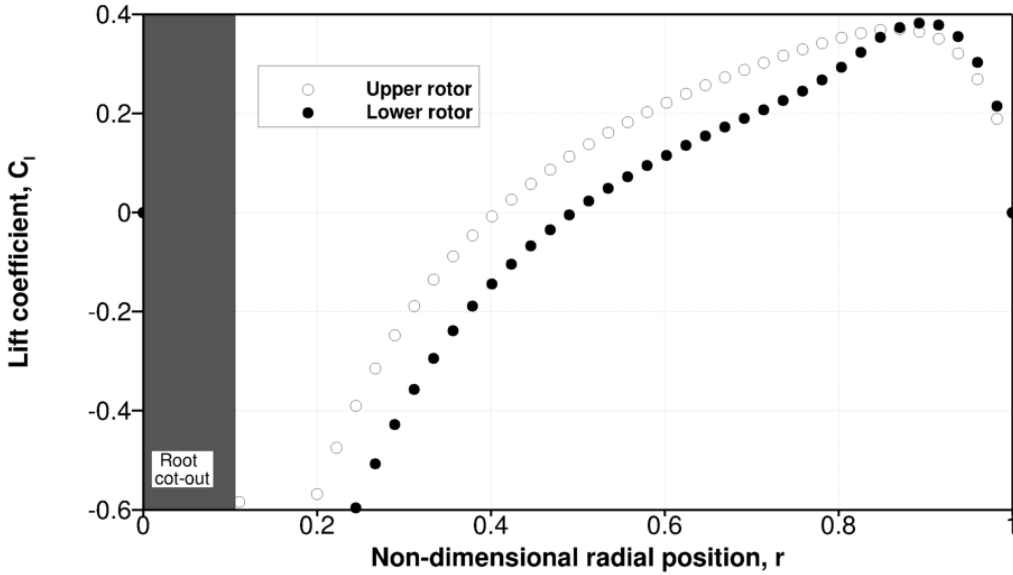


Fig. 17: Predicted spanwise lift coefficient on the upper and lower rotors for the Harrington 1 rotor in hover at $C_T = 0.004$.

increases the inflow ratio over the lower rotor. The resultant increase in inflow velocity increases the magnitude of the inflow angles at the blade elements, which can be seen by using

$$\phi = \tan^{-1} \left(\frac{U_P}{U_T} \right) \quad (3.4)$$

where U_P is the inflow. The increased inflow angle reduces the effective angle of attack α , and, therefore, a lower coefficient of lift is produced because the value of lift coefficient obtained from the airfoil lookup table is dependent on α .

$$C_l = C_l(\alpha) = C_l(\theta - \phi) \quad (3.5)$$

Figures 18(a) and 18(b) show the instantaneous inflow ratio and coefficient of lift distribution over the upper and lower rotors, respectively; notice that the upper rotor rotates in

a counter-clockwise and lower rotor rotates in a clockwise direction. The upper rotor wake impinging on the lower rotor can be clearly seen in Figs.18(a). Notice that the inflow ratio is higher in the region where the upper rotor wake impinges upon the lower rotor.

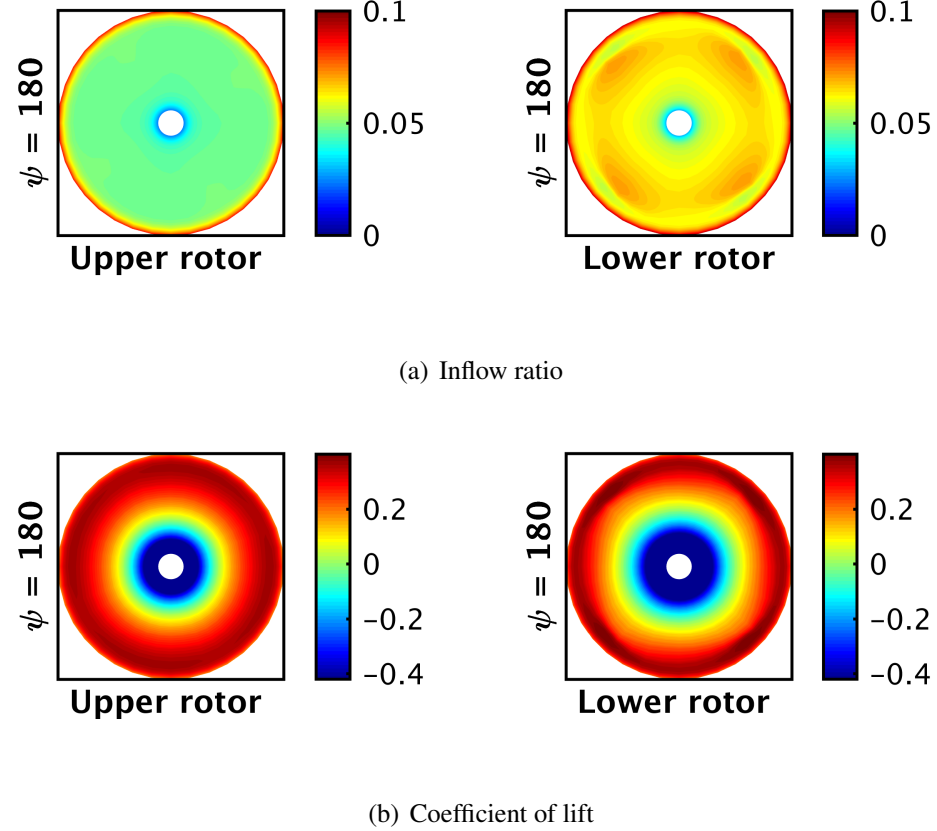


Fig. 18: Contour plot showing: (a) Inflow ratio and (b) Coefficient of lift across the Harrington 1 rotor.

Harrington 2

In this section, the results obtained for the other coaxial rotor geometry, the Harrington 2 rotor, are discussed. A schematic of the blade planform is shown in Fig. 19. Because of

the varying thickness of the blade; 24% thickness-to-chord ratio at the root and 15% ratio at the tip, using Eq. 3.1, the zero-thrust profile drag, C_{d_0} , was adjusted by adding 0.00312 so that the FVM prediction for C_{P_0} was similar to the measurements.

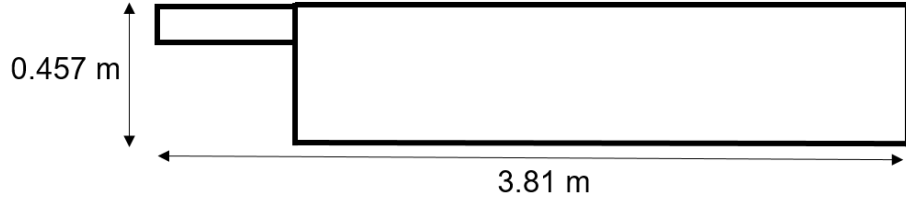


Fig. 19: Blade shape of the Harrington 2 rotor.

Figure 20 compares the predicted power polar for the Harrington 2 rotor with the experimental results, where it can be seen that the FVM results are in good agreement with the measurements. For the coaxial rotor case, however, there is an overprediction in power, similar to the observation made for the Harrington 1 rotor system.

Figures 21(a) and 21(b) show the instantaneous inflow ratio and coefficient of lift across the Harrington 2 rotor, respectively. The effects of the upper rotor wake impinging on the lower rotor can be seen in Figs. 21(a). Notice in Fig. 21(b), on the lower rotor contour near the blade tip region there are darker bands, which correspond to a higher coefficient of lift. These dark bands are not axisymmetric and are a result of blade passage effects; blade passage effects are basically the local effects of the counter-rotating blades passing close to each other, which gives a local perturbation in angle of attack.

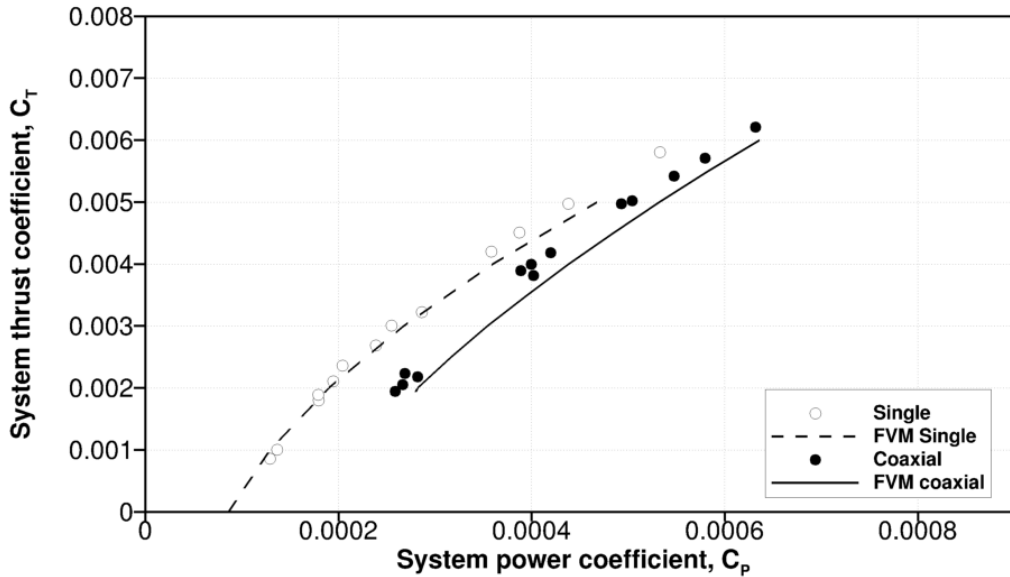


Fig. 20: Power polar for the Harrington 2 rotor.

Other performance factors such as spanwise inflow ratio, thrust coefficient, power coefficient, lift coefficient for the Harrington 2 rotor showed similar trends as for the Harrington 1 rotor and hence not discussed.

3.1.2 University of Texas (UT) Rotor

This section compares the FVM results with the experimental results obtained by Cameron and Sirohi at the University of Texas [16]; see Fig. 22 for a schematic of the blade planform of this rotor. The experimental results obtained during this study were for a small scale rotor, the tip chord Reynolds number of which is of the order of 0.45 million. The drag coefficient decreases with increasing Reynolds number up to 20 million [46]. For NACA 0012 airfoil, the drag coefficient, C_d , for Reynolds number below 1 million increases, so to

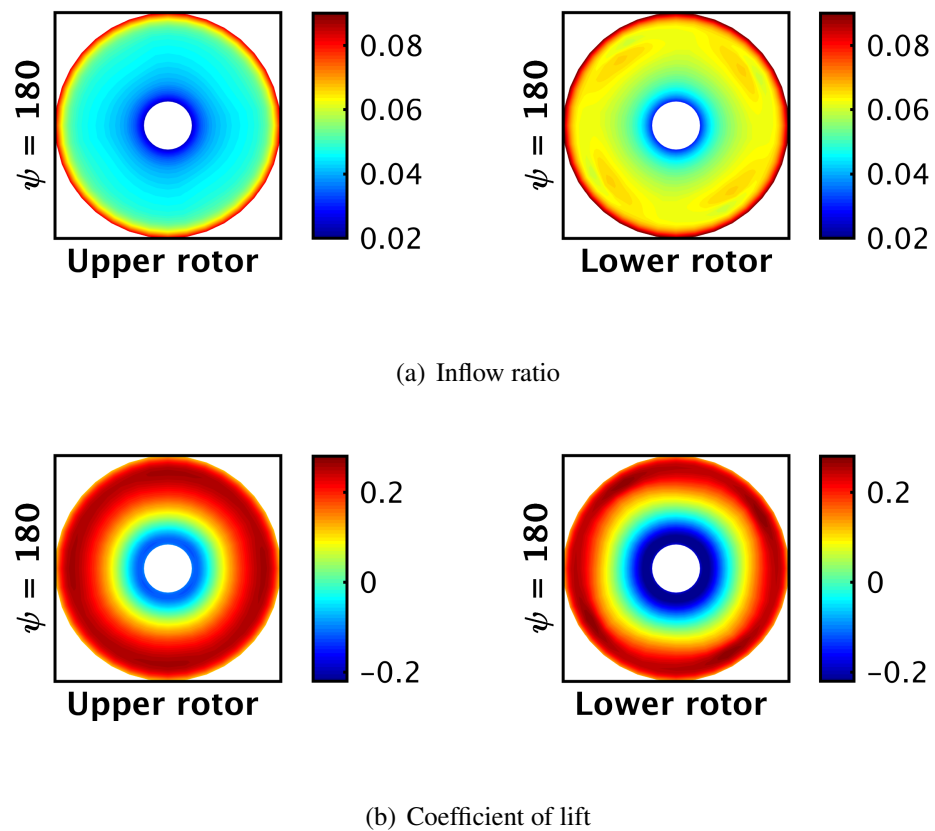


Fig. 21: Contour plot showing: (a) Inflow ratio and (b) Coefficient of lift across the Harrington 2 rotor.

account for the low Reynolds number drag characteristics, the profile drag coefficient for the model scale rotor was adjusted to 0.0012.

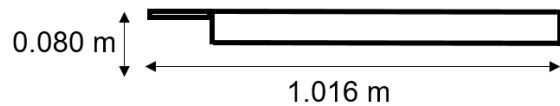


Fig. 22: Blade shape of the University of Texas coaxial rotor.

Figure 23 shows that the predictions compare very well with the experimental results for the single rotor, but a slight overprediction is obtained for the coaxial rotor configuration. It was found that the FVM could not trim this coaxial rotor at higher system thrust values, hence no results were available.

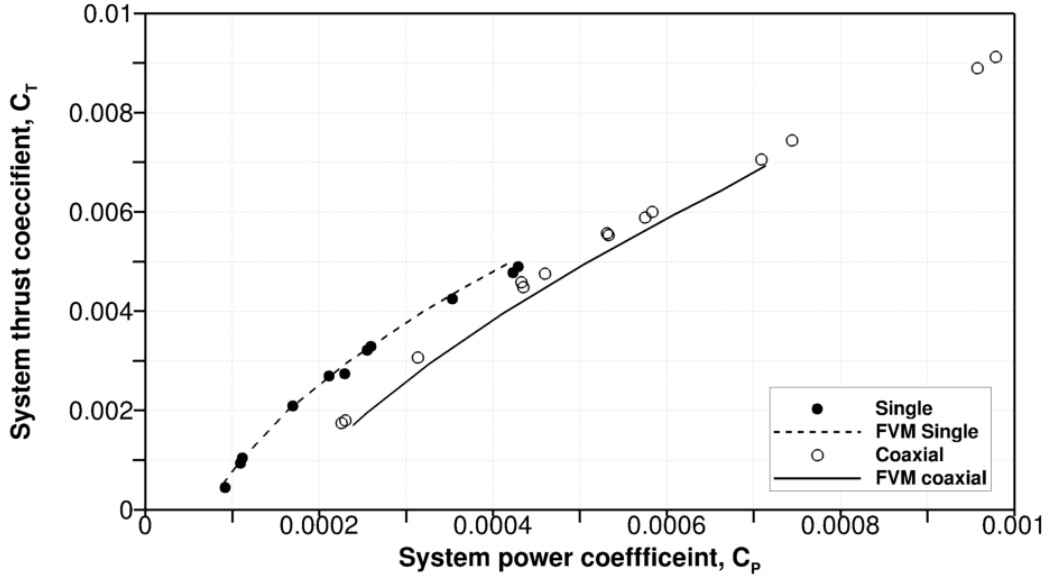


Fig. 23: Power polar for the University of Texas coaxial rotor.

Figure 24(a) and 24(b) show the instantaneous inflow ratio and lift distribution for the UT coaxial rotor respectively. The upper rotor wake impinging on the lower rotor can be seen clearly near the blade tip of the lower rotor. Concentrated dark red bands on the lower rotor shown in Fig. 3.24(b) are a result of blade passage effects. Other performance parameters such as thrust, power, etc. showed similar trends, just like the Harrington rotors.

Now that the the FVM predictions in hover have been shown to compare fairly well with the experimental results, a certain level of confidence has been established in the

methodology. The following section discusses the validation of the FVM for forward flight operation.

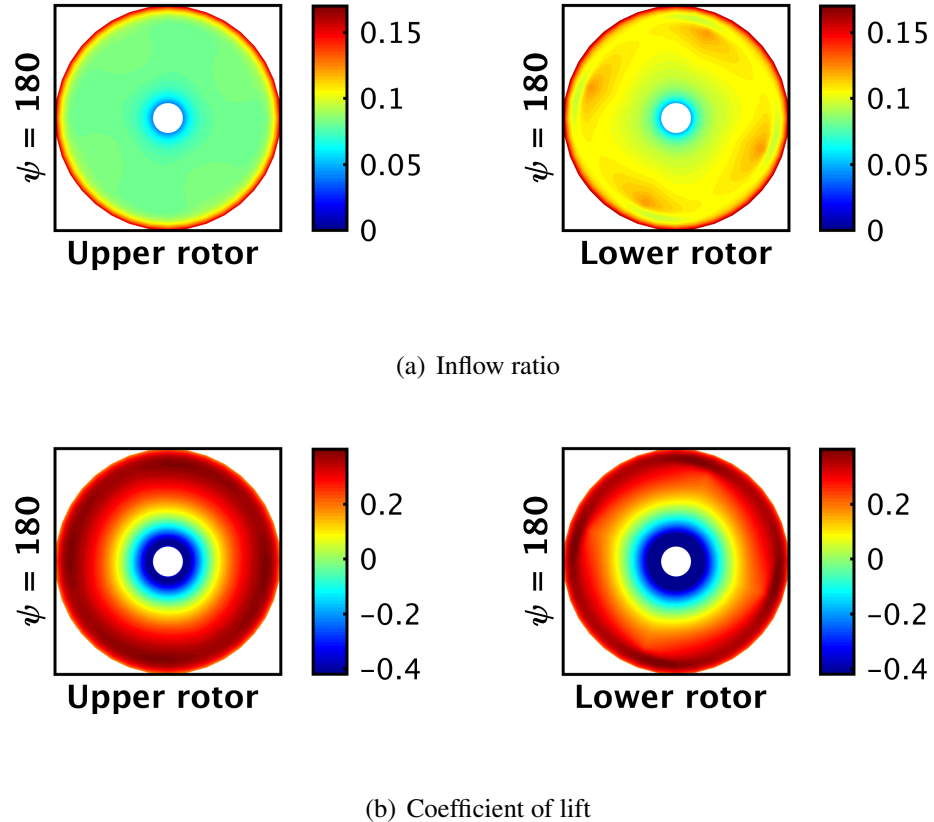


Fig. 24: Contour plot showing: (a) Inflow ratio and (b) Coefficient of lift across the UT coaxial rotor.

3.2 Forward Flight Validation

The relative dearth of experimental measurements on coaxial rotors makes it difficult to validate any type of performance prediction method. In fact, there are very few properly documented experiments for coaxial rotors in forward flight that can be used for validation

purposes. For most of the experiments, the wind tunnel trim conditions are not always available (i.e., the collective and cyclic pitch values) or other trim state such as based on a propulsive trim requirement to simulate free flight. Hence, without knowledge of the trim state usefulness of any measurements for validation purposes is unclear. Nevertheless, the following section discusses comparison between experiments conducted by Dingeldien and the FVM predictions for forward flight.

Harrington 1

Dingeldien [9] conducted experiments to study the performance of a single and a coaxial rotor in both hover and forward flight. The Harrington 1 rotor was used for these experiments. The coaxial rotor was tested at a constant system thrust coefficient of 0.0048 with a constant rotational tip speed.

Wind tunnel trim conditions are not mentioned but it would seem that an equivalent flat plate parasitic drag area of 0.929 m^2 was used to simulate the variation in the shaft angle with forward flight. The drag for the given equivalent flat plate parasitic drag area, f , is defined as

$$D_f = \frac{1}{2} \rho f V_\infty^2 \quad (3.6)$$

To overcome this drag, the TPP of the rotor is tilted forward by an amount

$$\sin \alpha_s = \frac{D_f}{T} \quad (3.7)$$

where T is the thrust and α_s is the rotor shaft angle, which is what would likely be used in the wind tunnel tests.

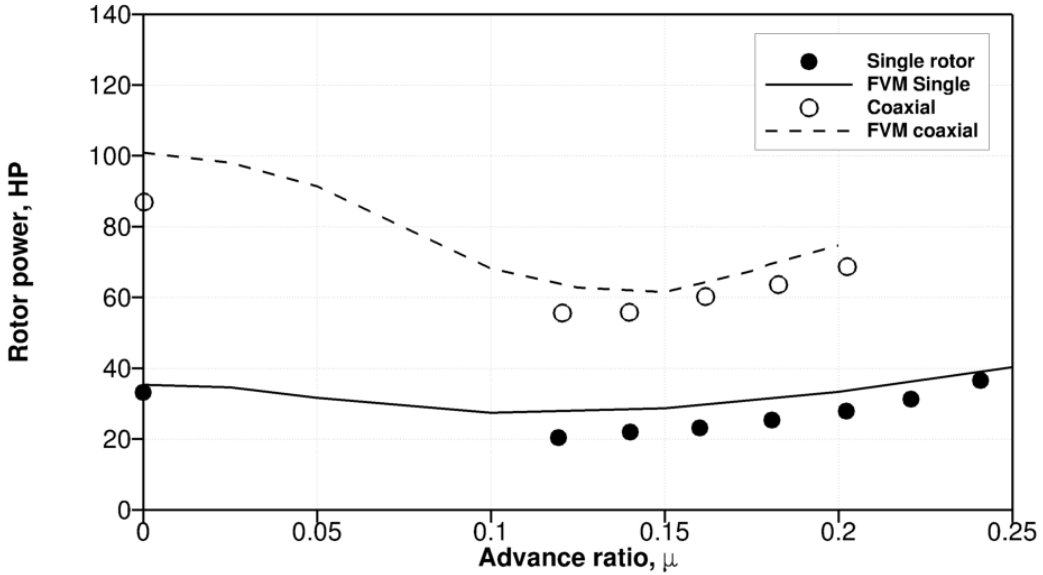


Fig. 25: Forward flight comparison for the Harrington 1 rotor with experimental results.

$$C_T = 0.0048 \quad V_{\text{tip}} = 142.95 \text{ m/s}$$

For the single rotor simulations, the total system thrust coefficient was 0.0024, i.e., half of the system thrust than for the coaxial rotor configuration. Similarly, the simulations were done at various advance ratios (μ) up to 0.25. For $\mu \geq 0.2$, the coaxial rotor did not trim properly and hence the predictions were not available.

The FVM predictions for the Harrington 1 single and coaxial rotor configuration are plotted in Fig. 25. There is an overprediction in power, however the trend in power variation with forward flight is well captured. Again, recall that trim conditions for the experiments were not clearly stated, which could be a reason the the FVM predictions overpredict the power.

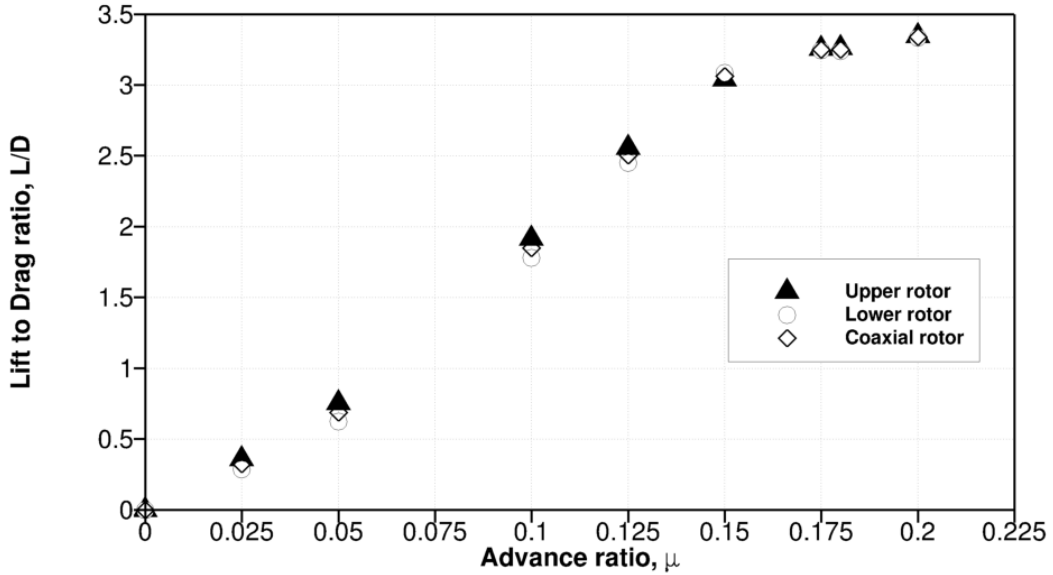


Fig. 26: Lift to drag ratio for the Harrington 1 rotor. $C_T = 0.0048$ $V_{\text{tip}} = 142.95$ m/s

The Lift-to-drag (L/D) ratio for the Harrington 1 rotor is shown in Fig. 26. As the forward flight speed increases, the induced power requirements decrease as a result L/D increases and reaches a maximum and then reduces quickly because the increasing drag of the rotor. Notice that in Fig. 26, the L/D ratio increases rapidly and then plateaus. In practice, the maximum L/D ratio for a rotor is important because it corresponds to the conditions of best aerodynamic efficiency.

The ratio of thrust carried by the upper (C_{T_u}/C_T) and lower rotor (C_{T_l}/C_T) to the total system thrust for the Harrington 1 is shown in Fig. 27. It is seen that the upper rotor carries more thrust than the lower rotor at all advance ratios, however the difference in thrust sharing is not the same at all advance ratios. The aerodynamic interference between the upper and lower rotors affects the lower rotor performance, increasing the torque required to pro-

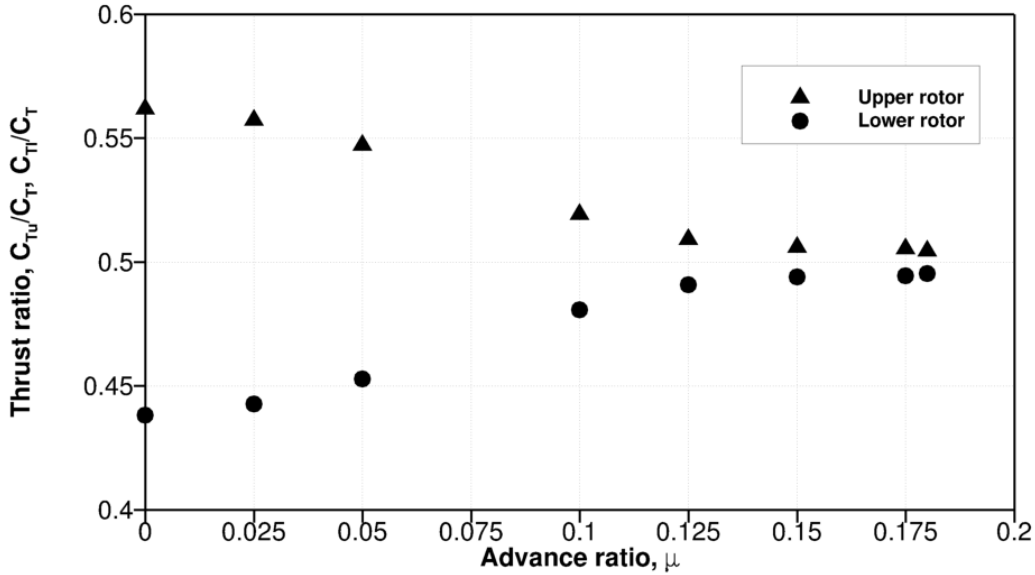


Fig. 27: Thrust sharing for the Harrington 1 rotor. $C_T = 0.0048$ $V_{\text{tip}} = 142.95$ m/s

duce a given thrust. Hence, for a torque balance the upper rotor needs to carry more thrust at all advance ratios to obtain a trimmed flight condition. As the advance ratio increases, the upper rotor wake skews back so the lower rotor is less influenced by the upper rotor, as shown in Fig 28. Eventually at higher advance ratios, the performance of the upper and lower rotors become almost independent of each other.

Inflow Contours at Varying Advance Ratios

Figures 29 and 30 (the arrows indicate the direction of flow) show the instantaneous inflow distributions across the upper and lower rotors of the Harrington 1 coaxial system. The inflow is highest across the upper and lower rotors during hover, as would be expected for any rotor, this is because the entire upper rotor wake is ingested by the lower rotor when

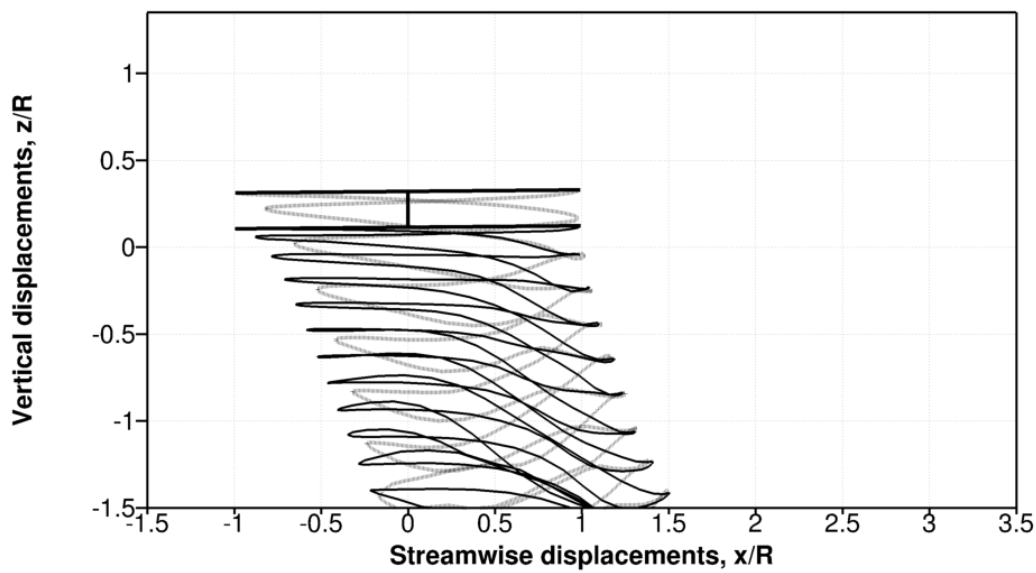
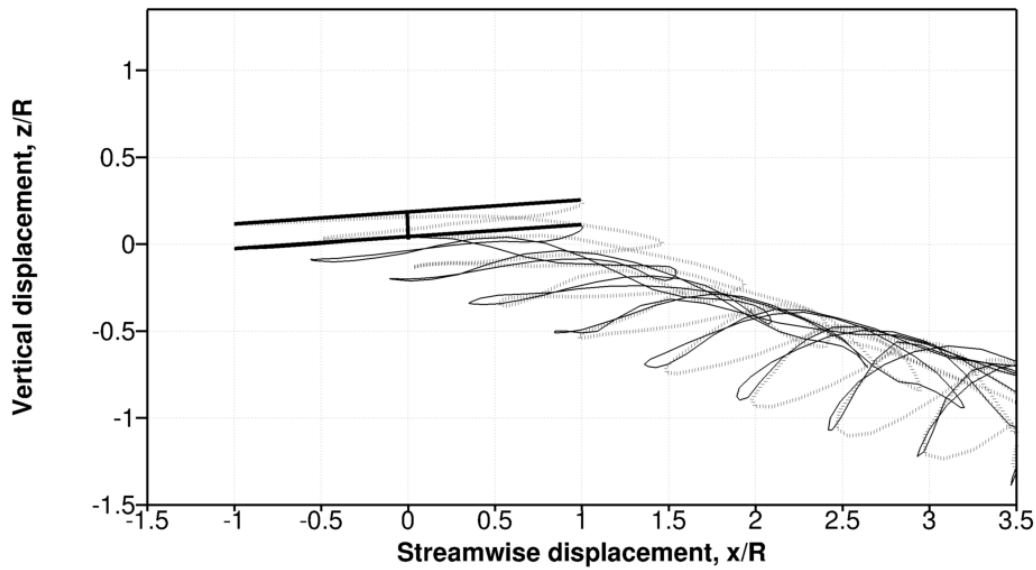
(a) $\mu = 0.05$ (b) $\mu = 0.18$

Fig. 28: Geometry of the blade tip vortices for varying advance ratio.

hovering. At an advance ratio of $\mu = 0.05$, the upper rotor wake does not impinge over the entire lower rotor, and a discontinuous inflow distribution is observed between the fore and aft parts of the lower rotor.

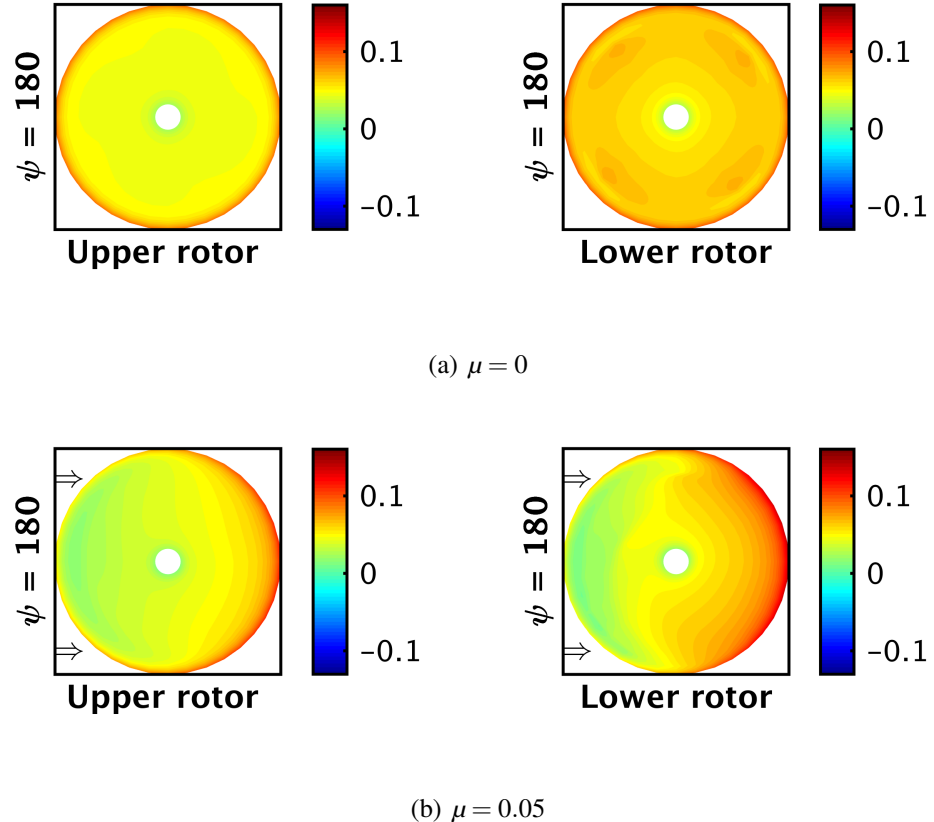


Fig. 29: Instantaneous contours of inflow distribution over the upper and lower rotors of the Harrington 1 rotor.

At a moderately higher advance ratio of $\mu = 0.10$, the contours indicate that the aft section of the lower rotor is mostly affected because of the wake from the upper rotor (notice the bands of yellow and dark red on the aft section of lower rotor). At $\mu = 0.20$, the inflow distributions on the rotors mimic each other (mirror images because the rotors

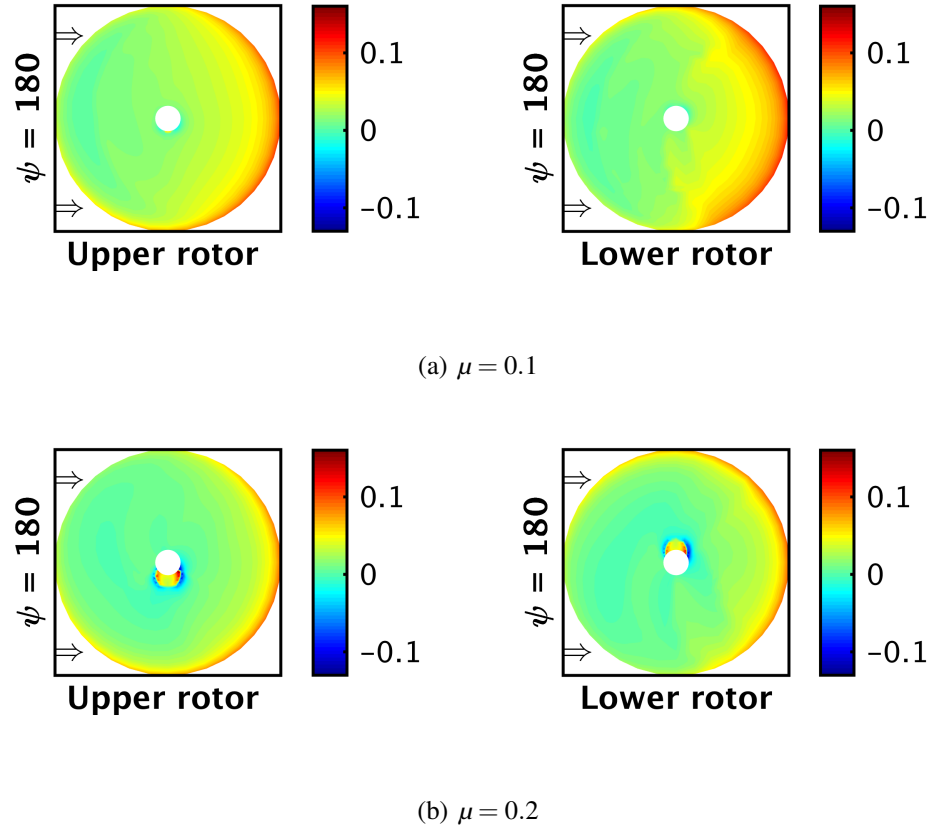


Fig. 30: Instantaneous contour of inflow distribution over the upper and lower rotors of the Harrington 1 rotor.

are counter-rotating) and also the development of the reverse flow region can be seen near blade root on the upper and lower rotors respectively (i.e., the dark blue regions on the retreating sides of the rotors).

Comparison with Wake Geometry Measurements: Ka-32

This section discusses comparison between the FVM predicted wake geometries and measured wake geometries for the Ka-32 coaxial rotor. Wake displacement data have been

obtained from smoke flow visualization experiments conducted by Akimov et.al. [47]. The results are plotted on a longitudinal plane passing through the rotor disk, i.e., for the $\psi = 0^\circ$ and 180° locations.

The comparison between predicted and measured wake geometries is shown in Figs. 31 and 32. Comparisons have been made at four different advance ratios, namely $\mu = 0.006, 0.089, 0.169$ and 0.279 . The total system thrust and shaft angle were adjusted to provide the same propulsive force to mimic the flight conditions.

At the lowest advance ratios it can be seen that the wake geometry is almost symmetric, with slight differences in the fore and aft locations; see Fig. 31(a). As the advance ratios increases, the wake geometry becomes different and the upper rotor wake does not impinge on the lower rotor entirely; see Fig. 31(b). At $\mu = 0.089$, the wake in the forward sections of the upper and lower rotors is close to the TPP, and this behavior is captured well by the FVM predictions for the upper rotor. However, there are a few discrepancies between the predictions and measurements for the lower rotor wake; see Fig. 31(b). But the wake geometry is captured well near the rear end of the rotor as the wake moves further downstream.

At moderately high advance ratios, i.e., $\mu = 0.169$ and 0.279 , the wake skews back and begins to look entirely different; see Fig. 32(a) and 32(b). At $\mu = 0.169$, the experiments indicate the tip vortices are close to the the TPP, but the FVM predicts that the tip vortices from the upper rotor are ingested by the lower rotor. At the downstream side of the rotor, while the upper rotor wake is captured by the predictions, the skew angle of the lower rotor

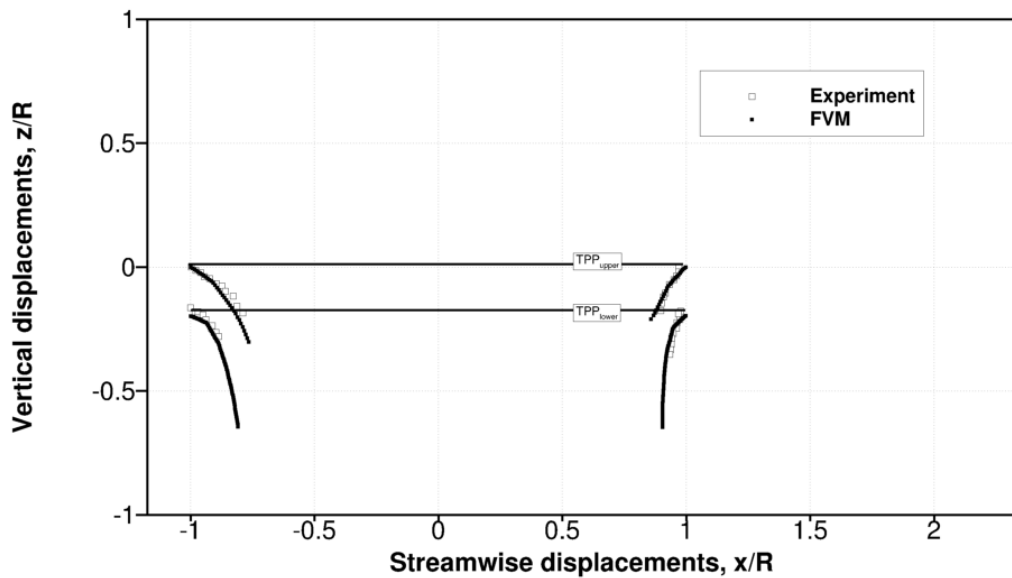
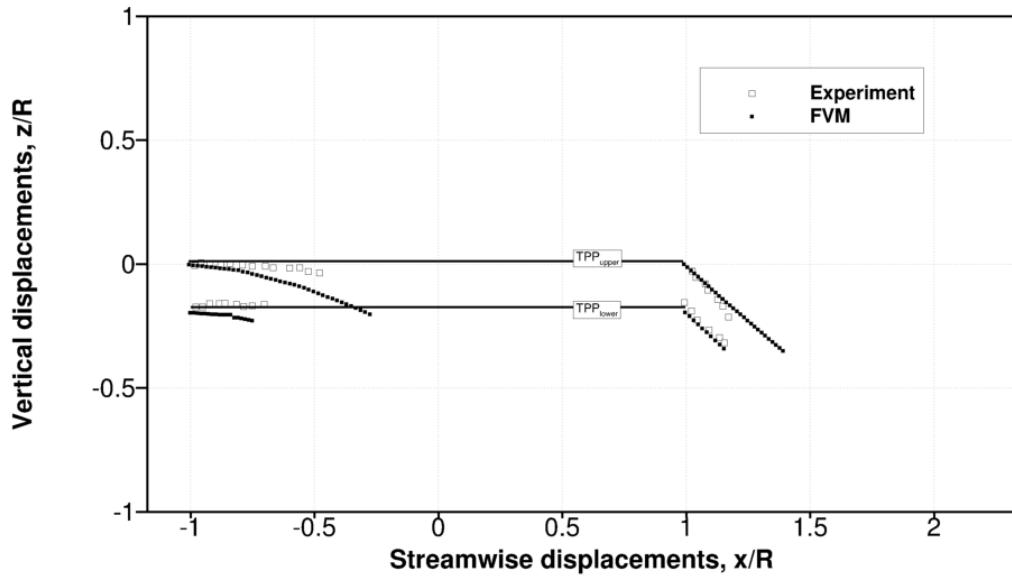
(a) $\mu = 0.006$ (b) $\mu = 0.089$

Fig. 31: Comparisons between the predicted and measured wake geometry for the Ka-32 rotor.

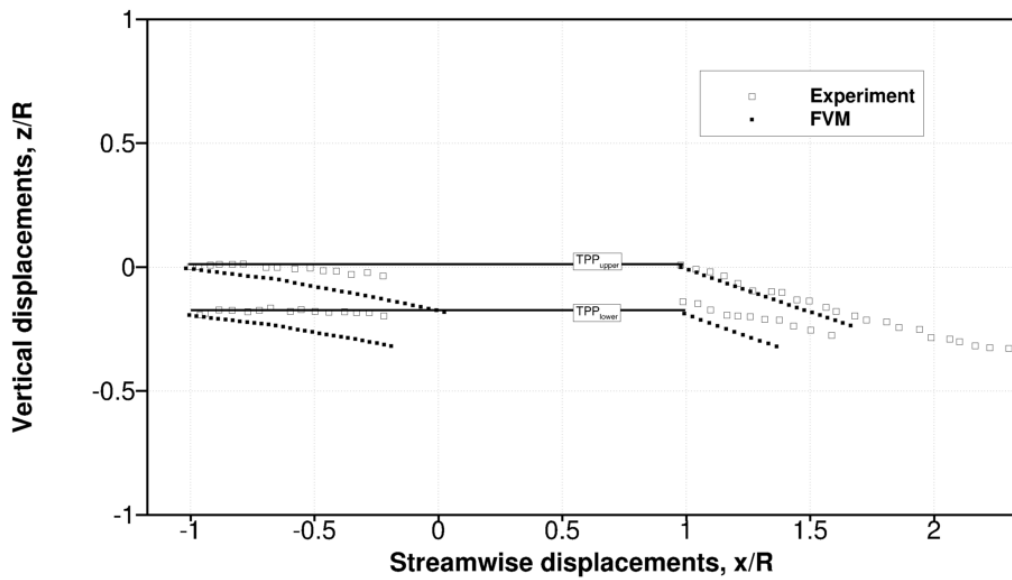
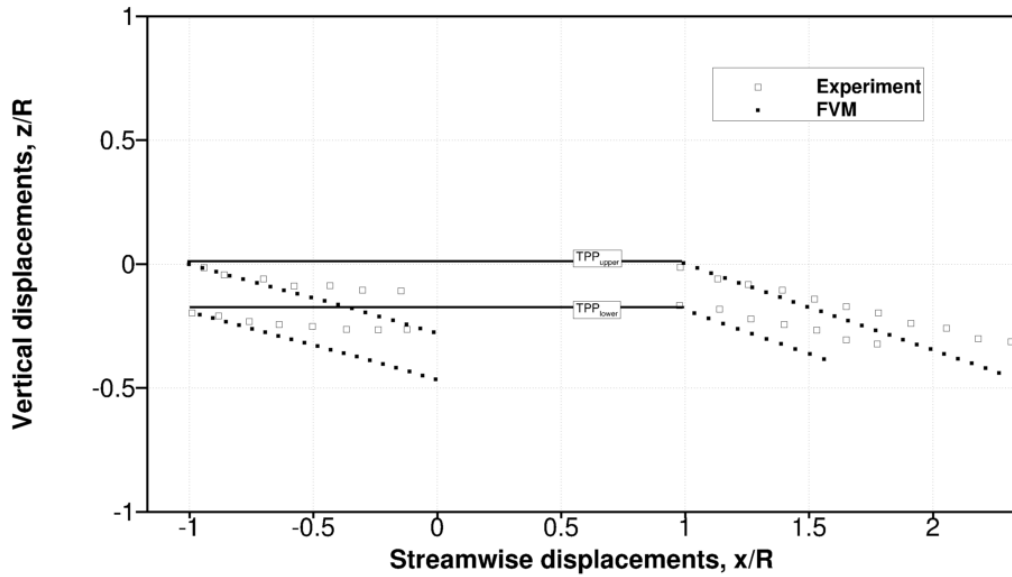
(a) $\mu = 0.169$ (b) $\mu = 0.279$

Fig. 32: Comparisons between the predicted and measured wake geometry for the Ka-32 rotor.

wake is underpredicted. At $\mu = 0.279$, the wake skew angle seems to be underpredicted for both the upper and lower rotors.



Fig. 33: Condensation of the rotor wake of the Ka-32 helicopter in hover.

Overall, the trends in the wake behavior seems to be captured well at low advance ratios, but as advance ratio increases the predictions are not as good. One reason for this discrepancy is that the fuselage effects are not taken into consideration in the the FVM. The Ka-32 fuselage is large and box-like, as shown Fig. 33, and at higher advance ratios the flow perturbations from the fuselage will reduce the downward convection of the tip vortices at the leading edge of the rotor disk and increase their convection at the rear of the rotor wake. These effects are most likely the reason for most of the discrepancies shown between the FVM and the measurements at the higher advance ratios.

3.3 Coaxial Rotor and Equivalent Single Rotor

This section discuss the comparisons that were made between a conventional single rotor and a coaxial rotor, in both hovering and in forward flight. A fair comparison between single rotor and coaxial rotor is not a straightforward as it might appear, and any type of comparisons need to be approached cautiously and also with careful qualification. The following section discusses the method used to derive an equivalent single rotor from a given coaxial rotor geometry.

3.3.1 Equivalent Single Rotor

To compare a single and a coaxial rotor on a fair basis, the rotors have to be identical in terms of geometry and also operating state. The parameters that have to be the same for the two rotor systems being compared are:

1. Number of blades, N_b
2. Disk loading, DL
3. Rotor solidity, σ
4. Tip speed, V_{tip}

Keeping the of blades, N_b , constant between the two rotor system ensures that the solidity, σ , is maintained for the coaxial system. Therefore, to derive an equivalent single rotor from a given coaxial rotor geometry, the total number of blades have to be equal. The disk loading, DL , is a very important parameter in helicopter analysis, which potentially

affects the hovering efficiency. Keeping the disk loading constant between any two rotor systems ensures that the rotors are compared on a fair basis. Tip speed, V_{tip} , has to be kept constant between the two rotor systems being compared because tip speed directly affects the profile power.

The coaxial rotor consists of an upper and a lower rotor, so the disk loading can be written as

$$\begin{aligned}(DL)_{\text{coaxial}} &= \frac{T}{A_{\text{tot}}} \\ &= \frac{T}{A^u + A^l}\end{aligned}\tag{3.8}$$

The two rotor systems are loaded equally so

$$\begin{aligned}(DL)_{\text{coaxial}} &= (DL)_{\text{eq}} \\ \frac{T}{A_{\text{coaxial}}} &= \frac{T}{A_{\text{eq}}} \\ \frac{T}{A^u + A^l} &= \frac{T}{A_{\text{eq}}}\end{aligned}\tag{3.9}$$

$$A_{\text{eq}} = 2A^u \quad (A^u = A^l)$$

$$\pi(R_{\text{eq}})^2 = 2\pi(R^u)^2$$

$$R_{\text{eq}} = \sqrt{2}R^u$$

The rotor solidity of the coaxial, σ_{coaxial} , and the equivalent rotor solidity, σ_{eq} , for the single rotor has to be equal so the equivalent single rotor will have blades of different chord length, i.e.,

$$\begin{aligned}\sigma_{\text{eq}} &= 2\sigma^u \quad (\sigma_{\text{coaxial}} = 2\sigma^u = 2\sigma^l) \\ \frac{N_b c_{\text{eq}}}{\pi R_{\text{eq}}} &= \frac{N_b c^u}{\pi R^u}\end{aligned}\tag{3.10}$$

$$c_{\text{eq}} = \sqrt{2}c^u$$

The result from Eq. 3.9 shows that the radius of the equivalent single rotor will be greater than for the coaxial rotor. If the rotational frequency for both the rotor systems is kept the same, then the tip speeds will be different. Because of this, the rotational frequency of the equivalent single rotor system has to be adjusted, i.e.,

$$(V_{\text{tip}})_{\text{eq}} = (V_{\text{tip}})_{\text{coaxial}}$$

$$\Omega_{\text{eq}} R_{\text{eq}} = \Omega_{\text{coaxial}} R_{\text{coaxial}} \quad (3.11)$$

$$\Omega_{\text{eq}} = \frac{\Omega_{\text{coaxial}}}{\sqrt{2}}$$

Using Eqs. 3.9, 3.10 and 3.11, the equivalent rotor geometry for a given coaxial rotor system can then be obtained. Using this approach, an equivalent single rotor for the Harrington 2 rotor is shown in Table 3.1. A comparison between the Harrington 2 rotor and its equivalent single rotor is discussed in the following section.

Table 3.1: *Rotor geometry of the Harrington 2 rotor and its equivalent single rotor.*

Parameter	Harrington 2	Equivalent single rotor
No. of rotors, N_r	2	1
No. of blades, N_b	2	4
Radius, R	3.81 m	5.38 m
Chord, c	0.457 m	0.645 m
Solidity, σ	0.152	0.152
Rotational frequency, Ω	31.50 rad/s	22.3 rad/s
Tip speed, V_{tip}	120 m/s	120 m/s
Rotor spacing, z/R	0.19R	-

3.3.2 Hover Performance Comparison: Harrington 2

The performance of the equivalent single rotor was predicted in hover using the FVM at several thrust values and the results plotted against Harrington 2 rotor; see Fig. 34. Prior studies have shown that the coaxial performs better than its equivalent single rotor (the geometry of the “equivalent” rotor was unclear in the previous studies) in hover, and the same trend was observed during this study. The coaxial rotor required about 9% less total system power than its equivalent single rotor configuration for varying values of total system thrust.

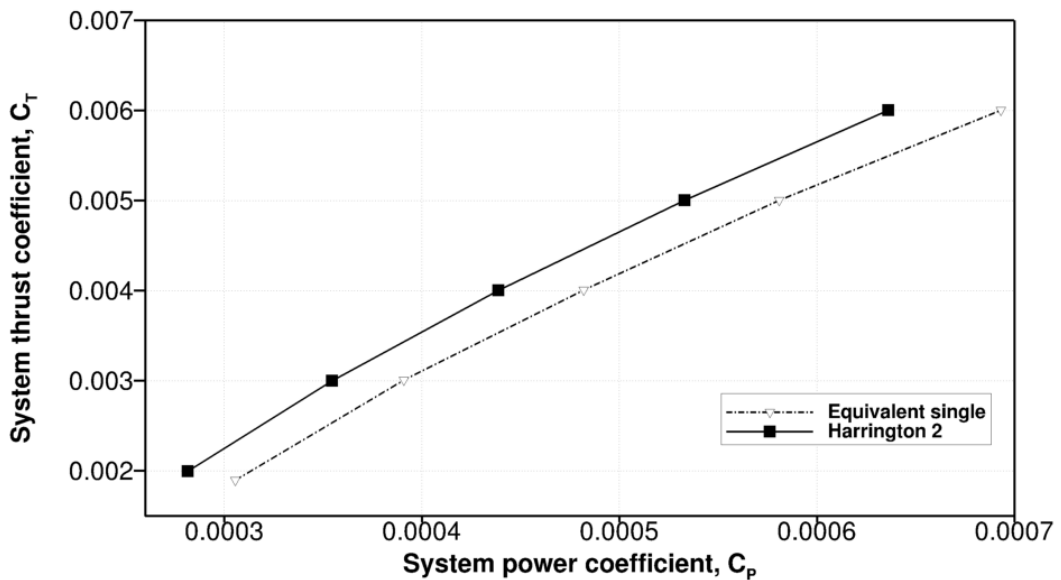


Fig. 34: Comparison between the Harrington 2 rotor and its equivalent single rotor in hover.

The breakdown of total system power into induced and profile power components in Fig. 35, shows that the profile power for both rotor systems is similar; the markers for C_{P_0} for the equivalent single rotor lie exactly behind the markers of the Harrington 2 rotor. The

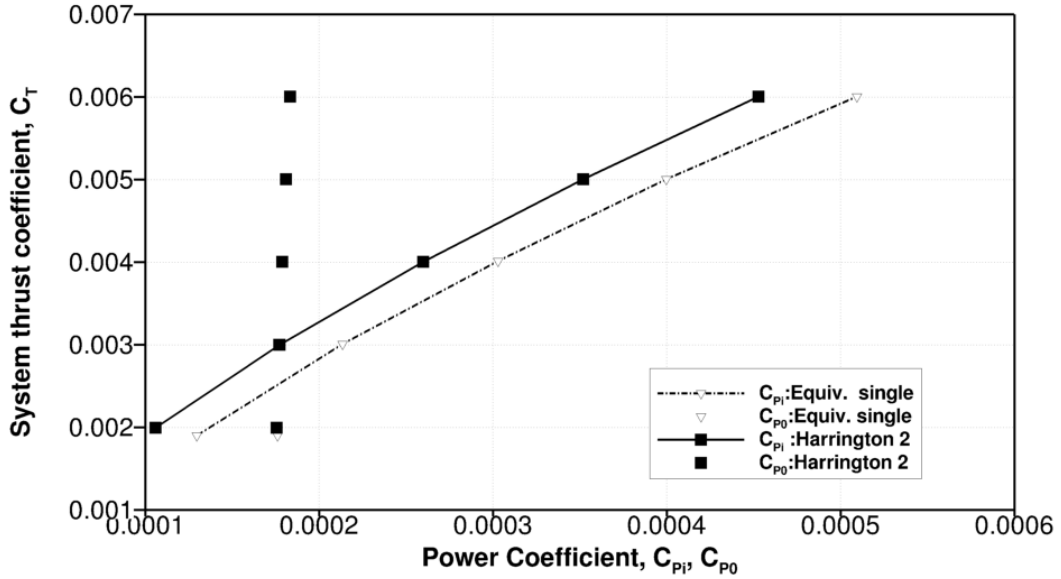


Fig. 35: Variation in induced and profile power at varying system thrusts for the Harrington 2 rotor compared with its equivalent single rotor.

difference in performance is entirely a result of induced power requirements; the coaxial rotor required between 11–17% less induced power over the system thrust range.

Notice the higher inflow ratio near blade tip of the equivalent single rotor, as shown in Fig. 36. Figure 37 indicates the thrust distribution (thrust per unit span), dC_T/dr , across the span of the equivalent single rotor is higher than of the upper and lower rotors of the coaxial rotor system.

3.3.3 Forward Flight Performance Comparison: UT Coaxial Rotor

Prior studies have suggested that the coaxial rotor performs better than its equivalent single rotor in forward flight [9, 32, 33]. The geometry of the assumed equivalent single

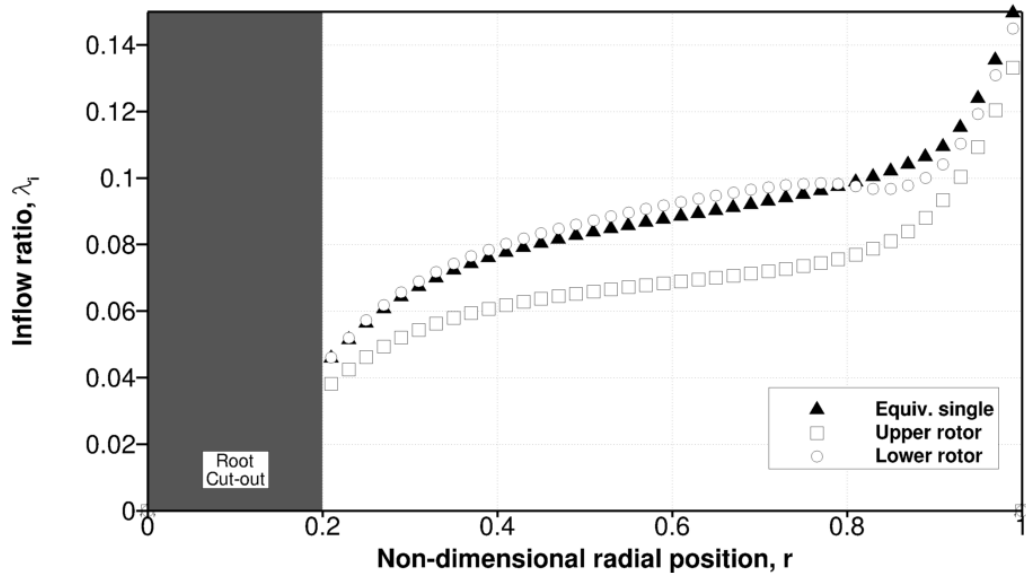


Fig. 36: Inflow distributions across the blade span of the Harrington 2 rotor and its equivalent single rotor in hover. $C_T = 0.005$

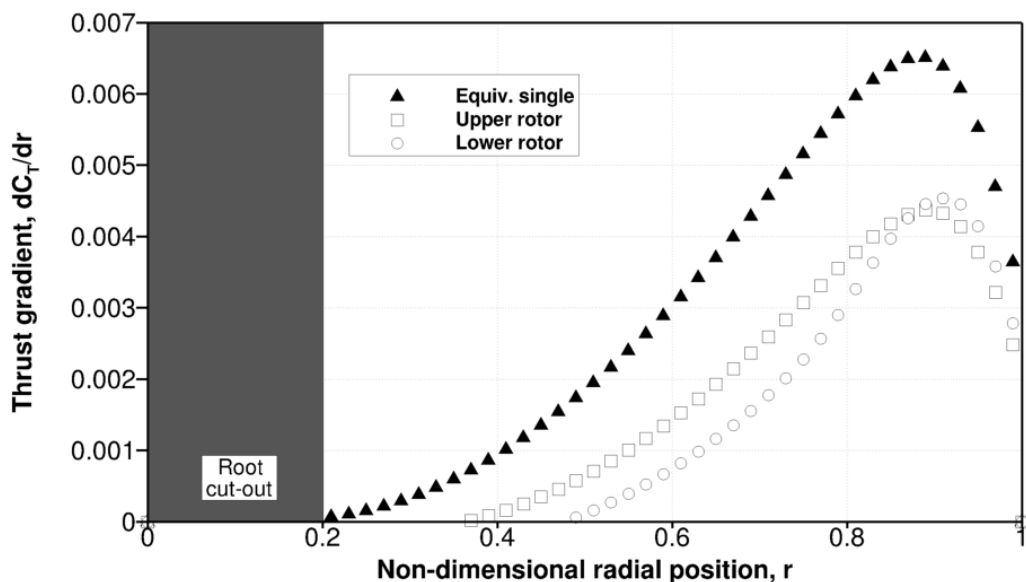


Fig. 37: Thrust gradient across the blade span of Harrington 2 and its equivalent single in hover. $C_T = 0.005$

rotors used in these studies, however, were not compared on the basis of the approach used in this thesis. Although the rotor solidity, σ , was kept constant, the disk loading was lower for the coaxial rotor (since the coaxial rotor consists of both an upper and a lower rotor), which is not a correct basis for comparison because a rotor with lower disk loading will always have lower induced losses. Loading the coaxial rotor and the single rotor equally for the same rotor disk loading establishes a much fairer basis for comparison.

The UT coaxial rotor tested at the University of Texas is used in the present study to compare the performance of a coaxial rotor and its equivalent rotor in forward flight. Equations. 3.9, 3.10 and 3.11 were used to derive the equivalent single rotor, as shown in Table 3.2.

Table 3.2: *Rotor geometry of the UT coaxial rotor and its equivalent single rotor.*

Parameter	UT coaxial rotor	Equivalent single rotor
No. of rotors, N_r	2	1
No. of blades, N_b	2	4
Radius, R	1.016 m	1.437 m
Chord, c	0.080 m	0.113 m
Solidity, σ	0.10	0.10
Rotational frequency, Ω	83.66 rad/s	59.15 rad/s
Tip speed, V_{tip}	85 m/s	85 m/s
Rotor spacing, z/R	0.14 R	-

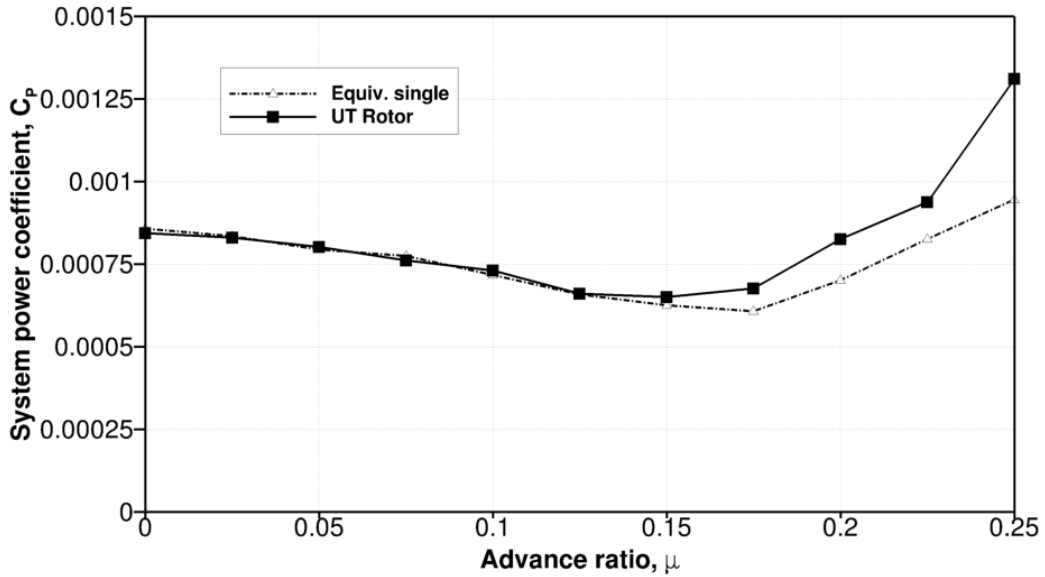


Fig. 38: Power required by the UT coaxial rotor compared to its equivalent single rotor in forward flight.

A plot showing a performance comparison between the UT coaxial rotor and its equivalent single rotor for several advance ratios is given in Fig. 38. The coaxial rotor system required less power than its equivalent single rotor in hover. As the advance ratio increases, both rotor systems require almost the same power up to an advance ratio of $\mu = 0.125$. Further increasing the advance ratio, however, shows that the two rotor systems require different power for operation; the coaxial rotor system required almost 38% more power at $\mu = 0.25$. This result is different from the previous studies, this result is not entirely unexpected because a different and more appropriate method is used in this thesis to derive the equivalent single rotor.

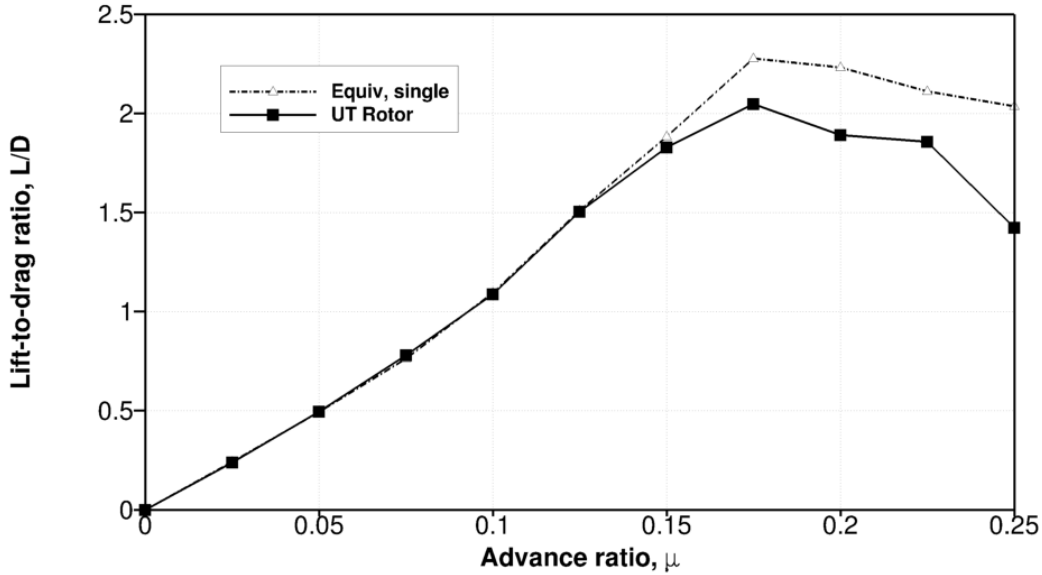


Fig. 39: Lift-to-drag ratios of the UT coaxial rotor compared to its equivalent single in forward flight.

The L/D ratios for the UT rotor are very low compared to full-scale coaxial rotors; see Fig 39. Notice, however, that the equivalent single rotor has a higher L/D compared to the coaxial rotor. The maximum L/D for both rotor systems occurs at similar advance ratios and hence the airspeed for maximum range will be same. As advance ratio increases, the L/D ratio decreases because of increase in profile drag of the rotor.

The ratio of thrust shared by the upper and lower rotors to the total system thrust is shown in Fig. 40. The thrust ratio of the upper rotor, C_{T_u}/C_T , decreases and thrust ratio of the lower rotor, C_{T_l}/C_T , increases as advance ratio increases. Both the upper and lower rotors performance is independent thus indicating lower aerodynamic interference at higher advance ratios.

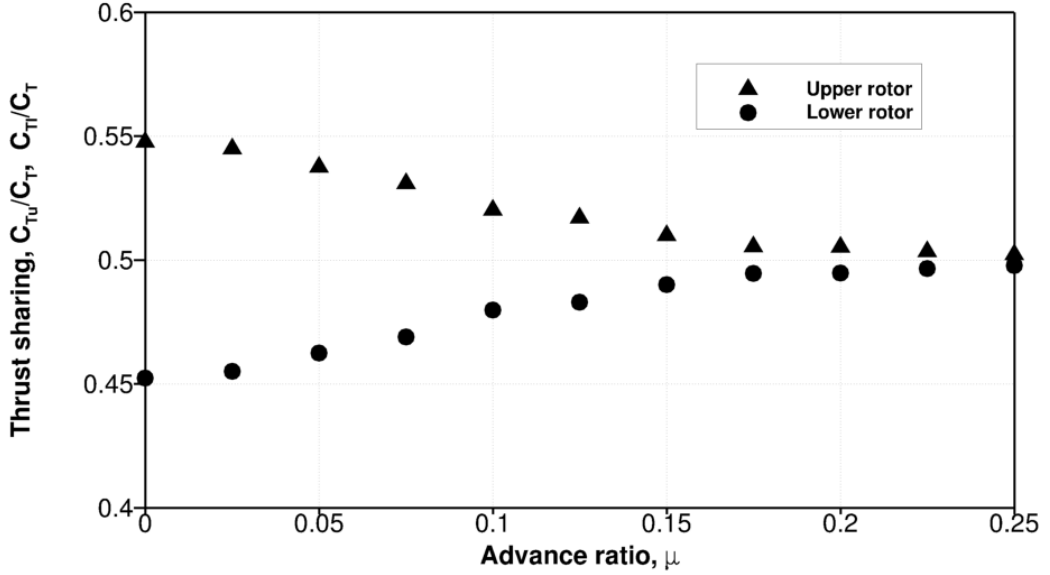


Fig. 40: Thrust sharing between the upper and lower rotors of the UT coaxial rotor in forward flight.

The wake geometry of the tip vortices is shown in Figs. 41(a) and 41(b) at $\mu = 0.15$ and 0.25, respectively. Notice the wake from the upper rotor skews back, which has a smaller influence on the lower rotor operation although it still does not operate independently. Consequently the upper and lower rotors are loaded almost equally, and the ratio of thrust shared is almost equal; see Fig. 40. Also, the C_T/σ for lower rotor increases with advance ratio. Although operation at a higher C_T/σ is desirable, flow separation is associated with rotor operations at too high a blade loading.

The maximum attainable value of C_T/σ depends on the local lift coefficient distribution across the rotor blade, the highest attainable lift coefficients being limited by stall. A contour of lift coefficient at $\mu = 0.2$ across an equivalent single rotor and UT coaxial rotor

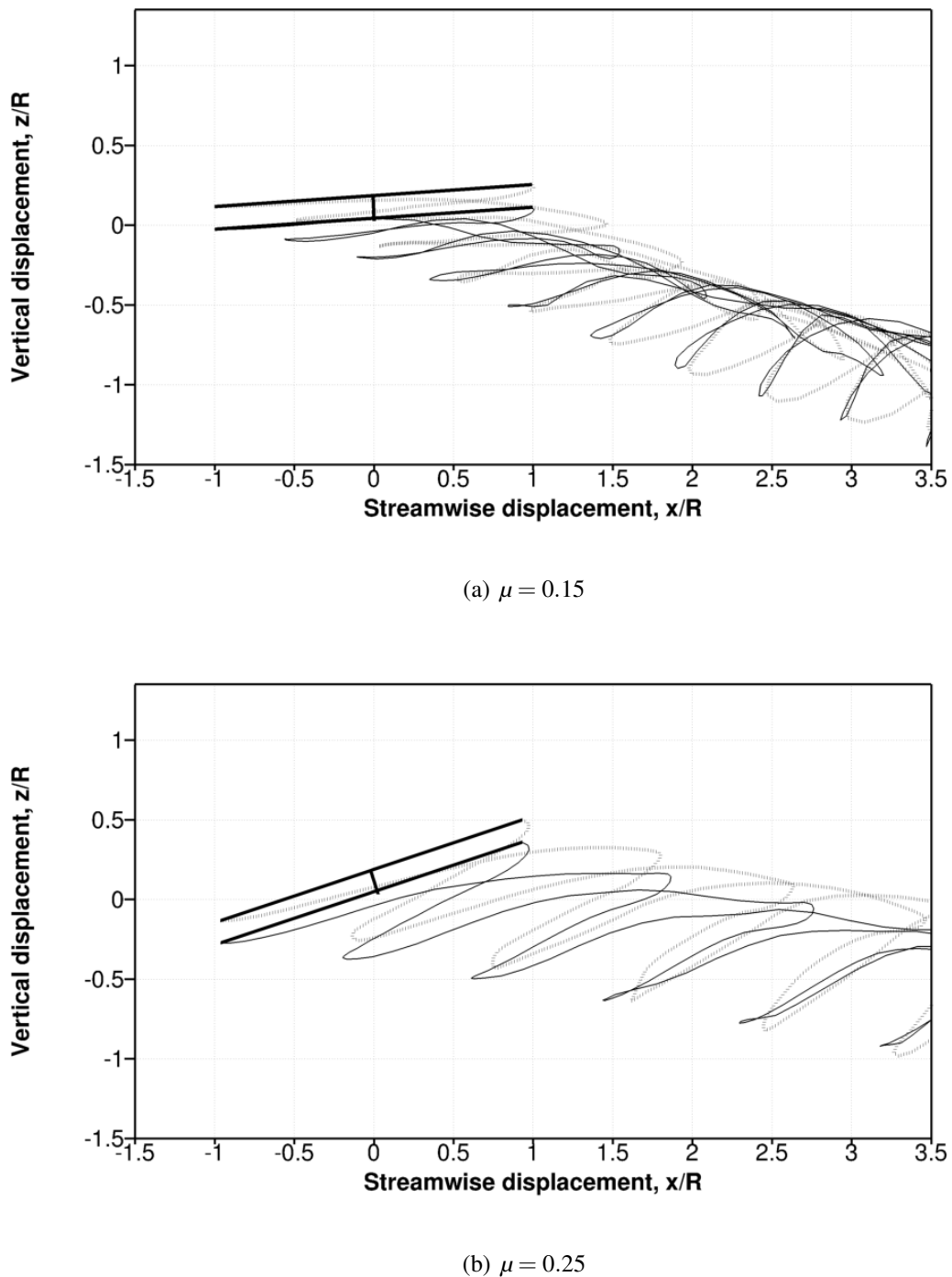


Fig. 41: Wake geometry produced by the UT rotor.

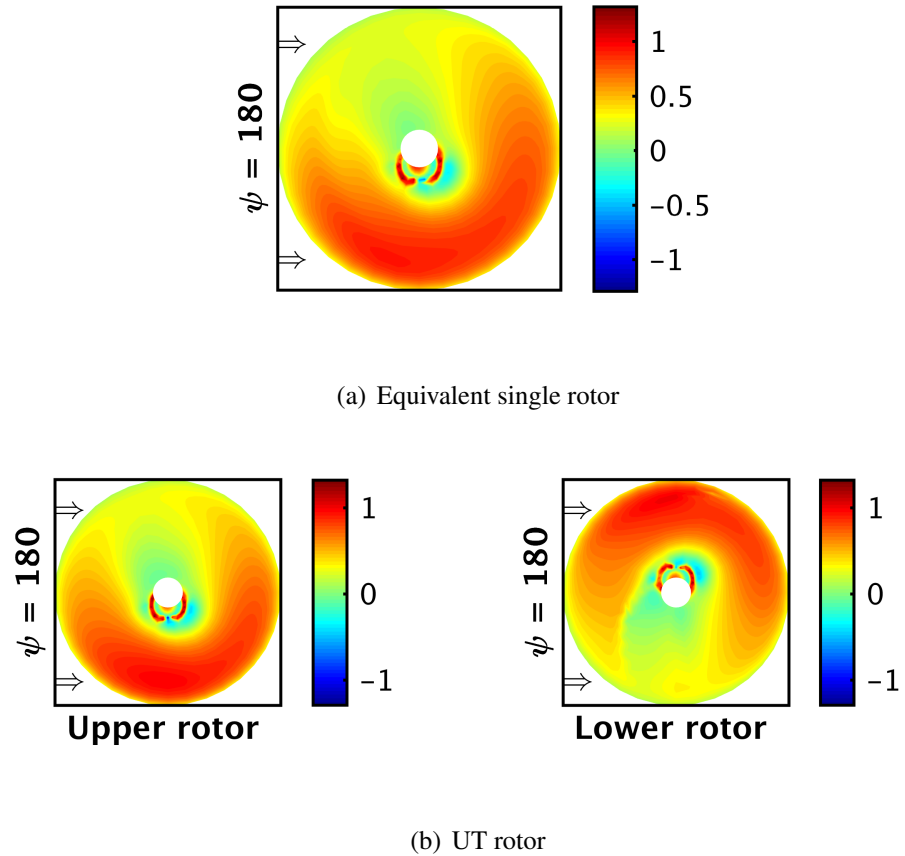


Fig. 42: Lift coefficient distribution across the UT rotor compared to its equivalent single rotor at $\mu = 0.2$.

is shown in Fig. 42. The lift coefficient near the retreating side of the equivalent single rotor is high; similarly, the lift coefficient across the upper and lower rotors is higher. At a higher advance ratios, as shown in Fig. 43, lift coefficient across the equivalent single rotor is higher. However, a section of the retreating sides of the upper and lower rotors has dark red bands indicating high lift coefficients, which is an indicator of the occurrence of blade stall.

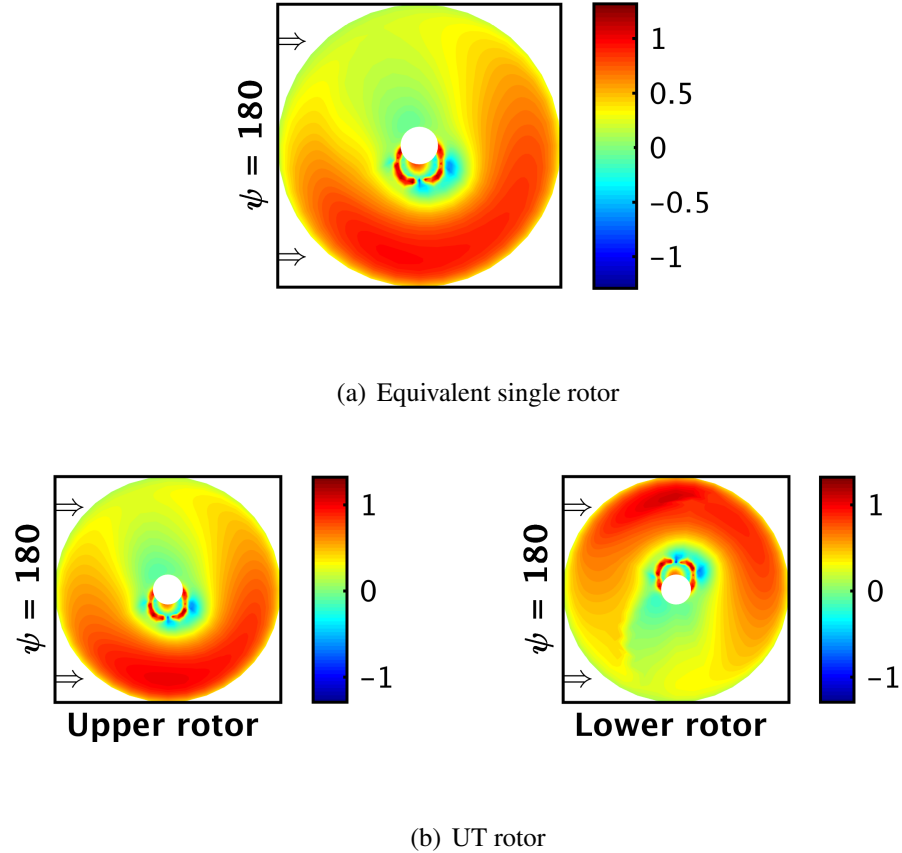


Fig. 43: Lift coefficient distribution across the UT rotor compared to its equivalent single rotor at $\mu = 0.225$.

At $\mu = 0.25$, onset of blade stall is seen on the upper and lower rotors; see Fig. 44(b).

However, the equivalent single rotor does not show any evidence of blade stall in Fig. 44(a).

Figure 44(b) indicates that C_T/σ is too high for the upper and lower rotors blades, especially for the lower rotor. The reason for this behavior is that the blades of the UT rotor are untwisted and non-tapered, which increases local lift coefficients at the inboard blade stations and produces premature stall at a lower value of C_T/σ .

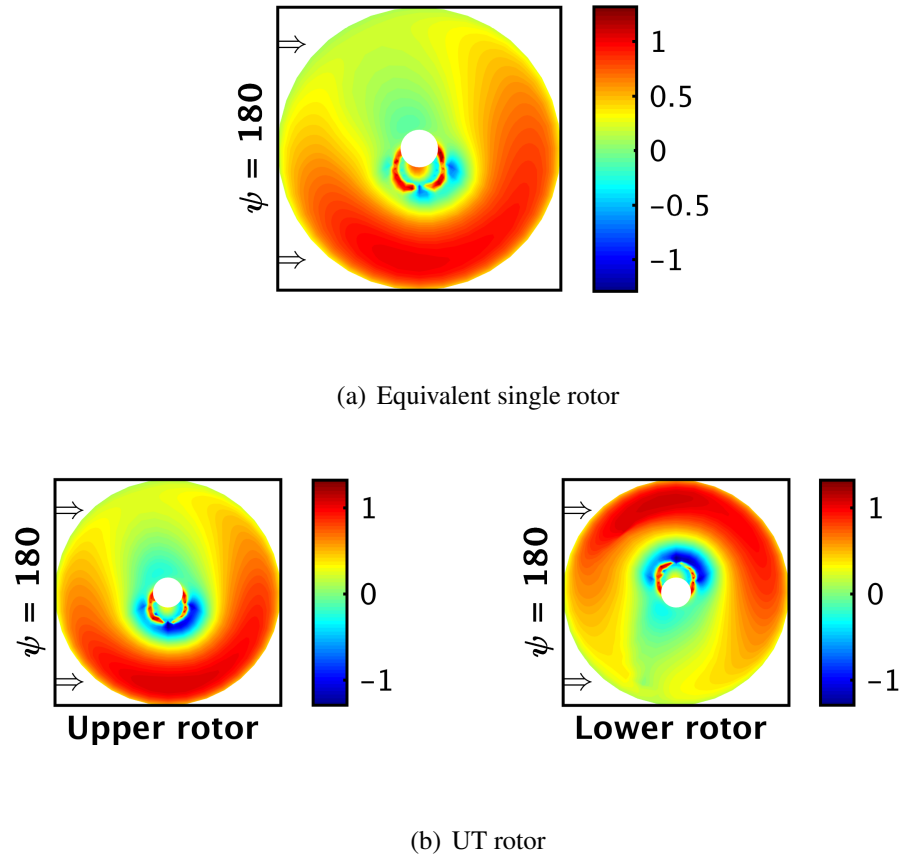


Fig. 44: Lift coefficient distribution across the UT rotor compared to its equivalent single rotor at $\mu = 0.25$.

3.4 Inter-Rotor Spacing: Harrington 2

This section discusses the effect of inter-rotor spacing on the performance of the coaxial rotor system. Furthermore, the effect of lower rotor on the performance of the upper rotor is also discussed. To this end, the Harrington 2 coaxial rotor system was used to investigate the effects of inter-rotor spacing. The coaxial system was tested for very low to moderately high inter-rotor spacings. The original inter-rotor spacing of $z/R = 0.19R$ of

the Harrington 2 was used, in addition to $z/R = 0.10$ and $z/R = 0.30$. The gains/loss in performance at different inter-rotor spacing were normalized with respect to the performance of the Harrington 2 rotor operating at a spacing of $z/R = 0.19R$.

The rotor geometry of the Harrington 2 is shown in Table A.2. The results in Fig. 45 compares the performance of the coaxial rotor at varying inter-rotor spacing. At $z/R = 0.30$, the coaxial rotor required 12% less power at low thrust and 0.08% less power at a higher thrust compared to an inter-rotor spacing of $z/R = 0.19R$. However, for a lower inter-rotor spacing the performance of the coaxial rotor system degrades. At $z/R = 0.10$, the coaxial rotor system required almost 24% more power for all values of thrust. This outcome is because of increased aerodynamic interference between the upper and lower rotors at lower values of inter-rotor spacing.

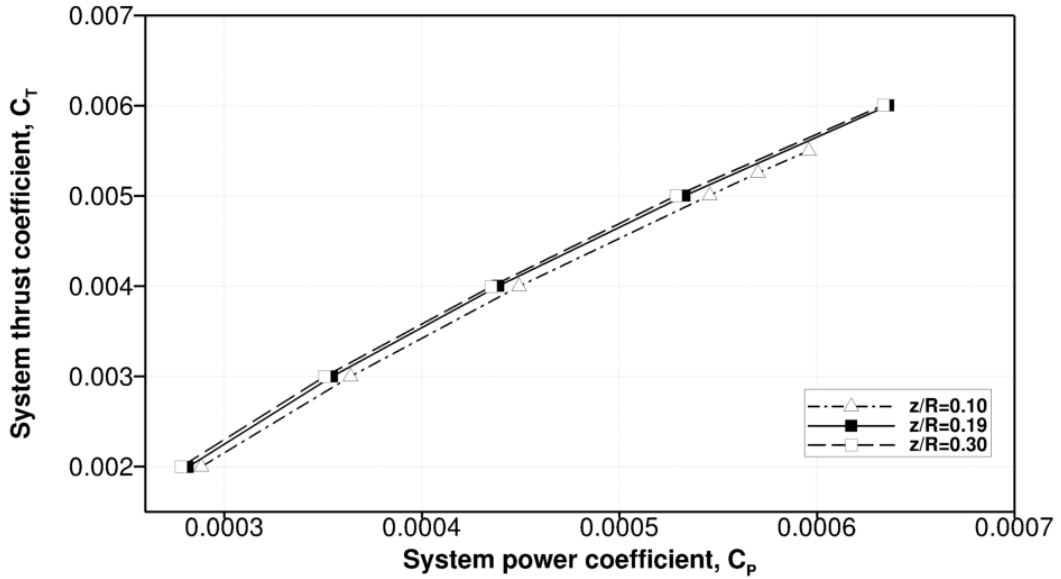


Fig. 45: Power polar of the Harrington 2 for varying inter-rotor spacings.

Notice that for a spacing of $z/R = 0.10$, the coaxial rotor system does not trim at higher thrust values. At low inter-rotor spacing the blade passage effects are more pronounced and so affect the performance of the rotor system, as shown in Fig. 48(a).

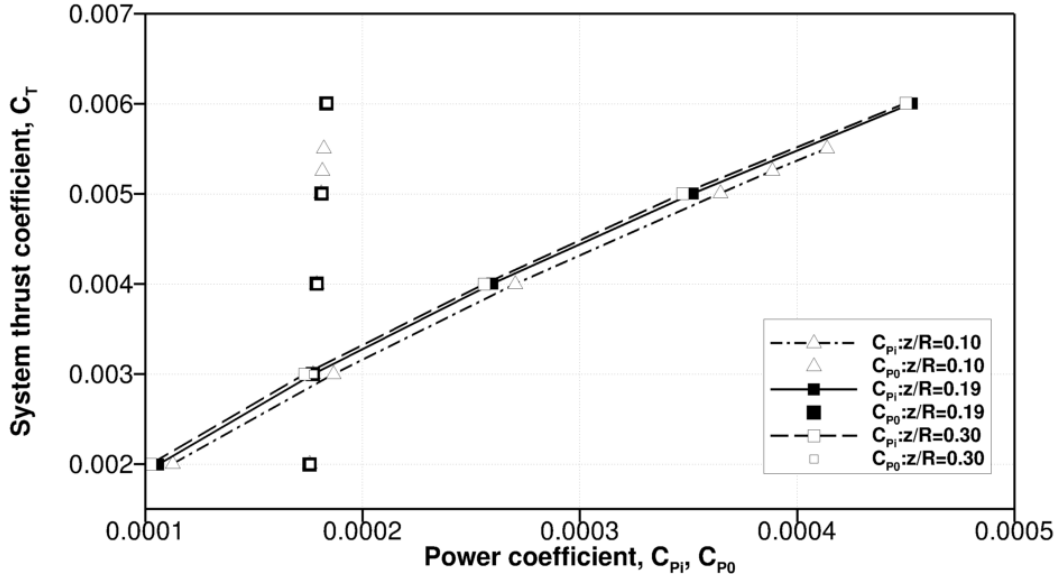
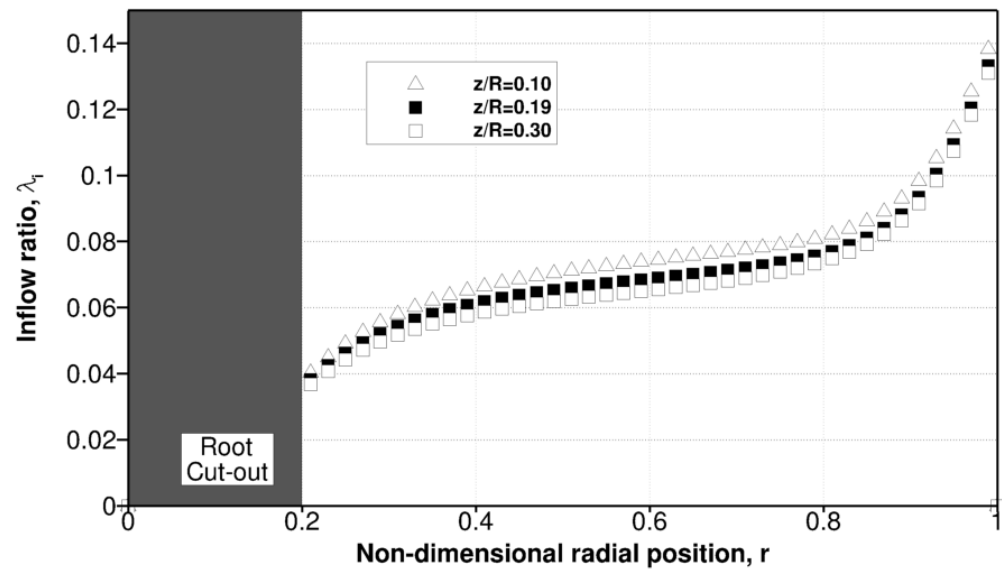


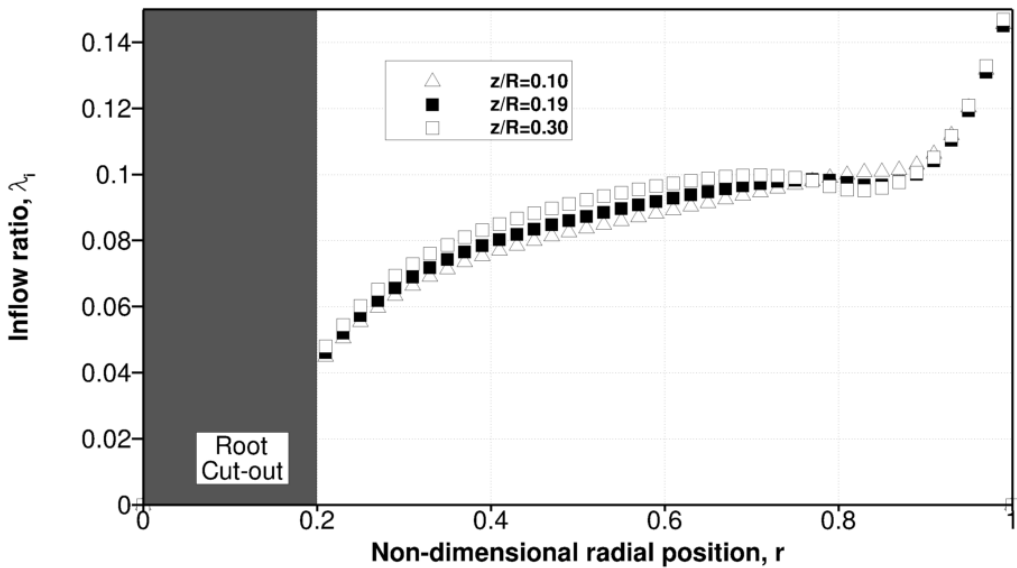
Fig. 46: Decomposition of induced and profile power for varying inter-rotor spacing.

In Fig. 46, the induced and profile power requirements at different inter-rotor spacings is plotted. Notice that the profile power requirements at all inter-rotor spacing remains the same, while the induced power requirement is clearly different.

The spanwise inflow ratio across the upper and lower rotors of the Harrington 2 rotor at a total system thrust of $C_T = 0.005$ is shown in Figs. 47(a) and 47(b), respectively. Notice the inflow distribution across the span is different for the upper rotor as the inter-spacing varies. The inflow ratio increases by 7% at $z/R = 0.10$, whereas the inflow decreases by 4% at $z/R = 0.30$. Similarly, Fig. 47(b) shows that the inflow across the lower rotor varies



(a) Upper rotor



(b) Lower rotor

Fig. 47: Spanwise inflow ratio across the Harrington 2 rotor.

for different inter-rotor spacings. The inflow ratio across the lower rotor decreases by 2% at $z/R = 0.10$ while the inflow increased by 3.5% at $z/R = 0.30$. At $z/R = 0.10$, there is no evidence of the upper rotor wake impinging on the lower rotor.

Figure 48 shows the inflow ratio contours across the upper and lower rotors at varying inter-rotor spacing of the Harrington 2 coaxial rotor system. Notice the inflow ratio (increase in light blue region) on the upper rotor decreases as inter-rotor spacing increases.

Figure 49 shows the ratio of thrust shared by the upper and lower rotors at varying inter-rotor spacings. At $C_T = 0.005$, the upper rotor at $z/R = 0.30$ carries 57% of total system thrust, whereas the upper rotor at $z/R = 0.10$ carries 54% of thrust. Consequently, the lower rotor carries 43% and 46% at $z/R = 0.30$ and $z/R = 0.10$, respectively. Because the thrust carried by the lower rotor increases as the rotor spacing decreases, the induced power required increases. The coaxial rotor is trimmed for a torque balance, hence the upper rotor operates at the same torque as the lower rotor, and so an increase in the power is required at lower inter-rotor spacings.

The wake geometry for the Harrington 2 coaxial rotor at different inter-rotor spacings is shown in Fig. 50. The upper rotor wake contracts up to $0.79R$ when it impinges on the lower rotor at an inter-rotor spacing of $z/R = 0.30$. It is known that, induced loss is maximum at low inter-rotor spacing [7], where it was stated that for minimum induced losses the lower rotor has to operate in the fully developed wake of the upper rotor. Theoretically, the wake contraction ratio is about $0.707R$, and it has been found experimentally that is about $0.78R$ [2]. It is therefore necessary the wake contracts by this much for minimum induced losses. Clearly, the results in Fig. 50 shows that the wake from the upper rotor contracts

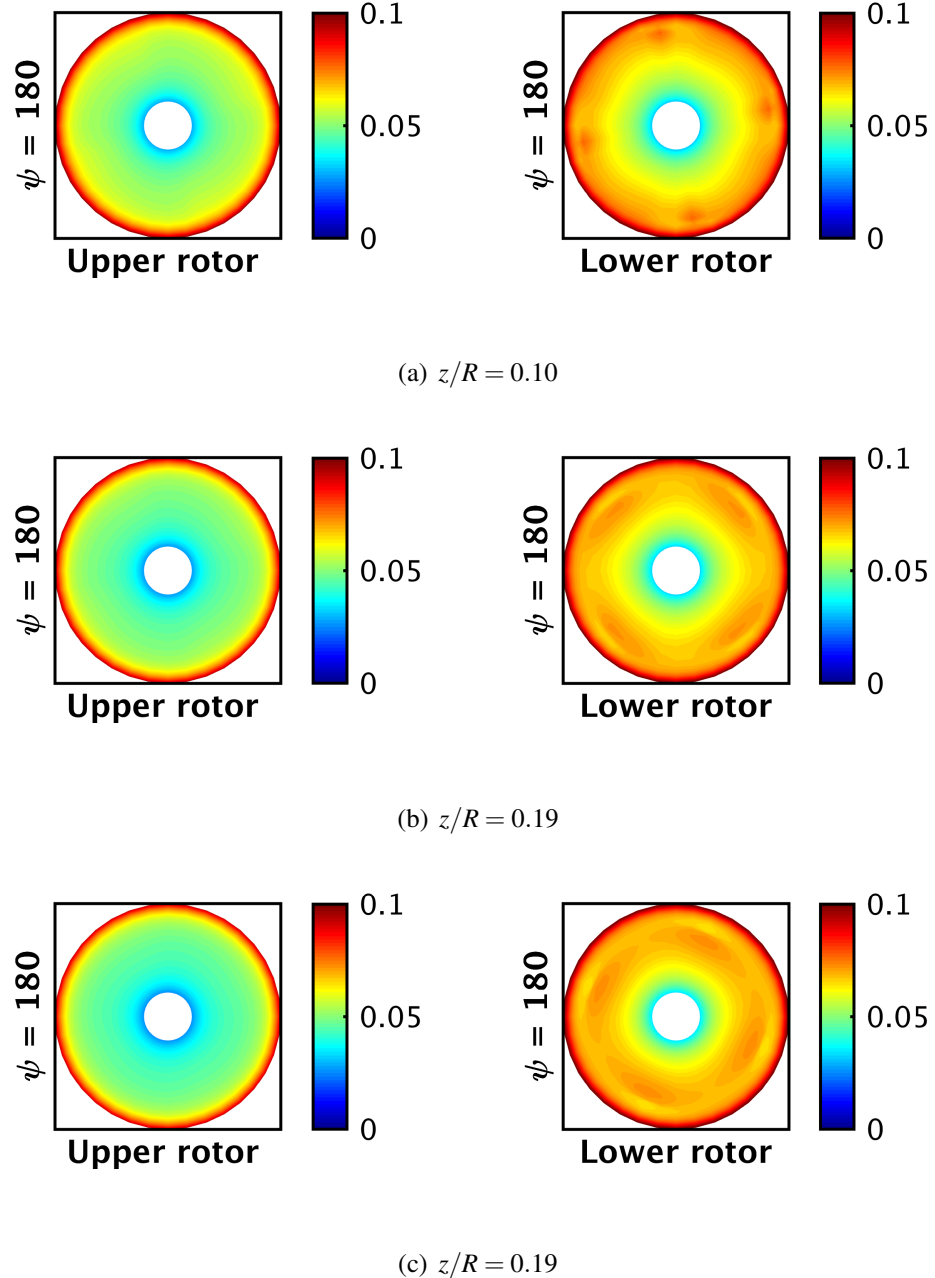


Fig. 48: Inflow ratio across the upper and lower rotors of the Harrington 2 rotor.

up to $0.83R$ at an inter-rotor spacing of $z/R = 0.10$. This explains why the coaxial system performance degrades as inter-rotor spacing is reduced.

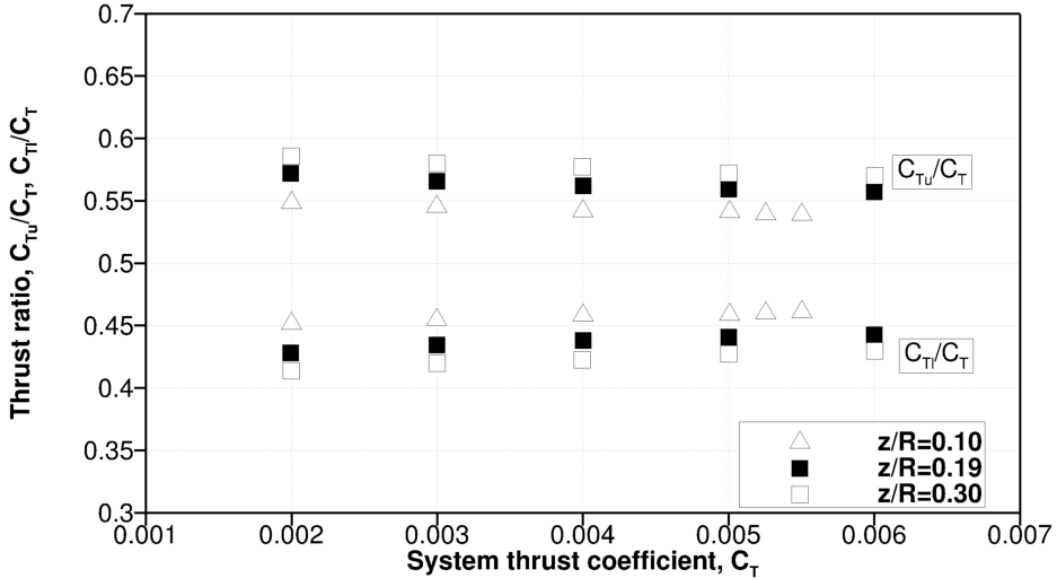


Fig. 49: Thrust sharing for varying inter-rotor spacings of the Harrington 2 rotor.

3.5 Effects of Comparison with Isolated rotors: UT coaxial rotor

The aerodynamic interactions between upper and lower rotors influence the power requirements of the coaxial rotor system. This section discusses the performance losses the upper and lower rotors incur from the effects of aerodynamic interference. The UT coaxial rotor was used to investigate aerodynamic losses of the upper and lower rotors operating as a coaxial rotor system. For the isolated system simulations, the single rotor was trimmed for a thrust that the upper and lower rotors of the coaxial rotor trimmed at when operating in a coaxial system for varying advance ratios. The isolated system performance is a sum of the performance of isolated upper and lower rotors.

Figure 51 shows the performance of the coaxial rotor and isolated system. The isolated system required less power than the coaxial rotor system. This is an expected result because

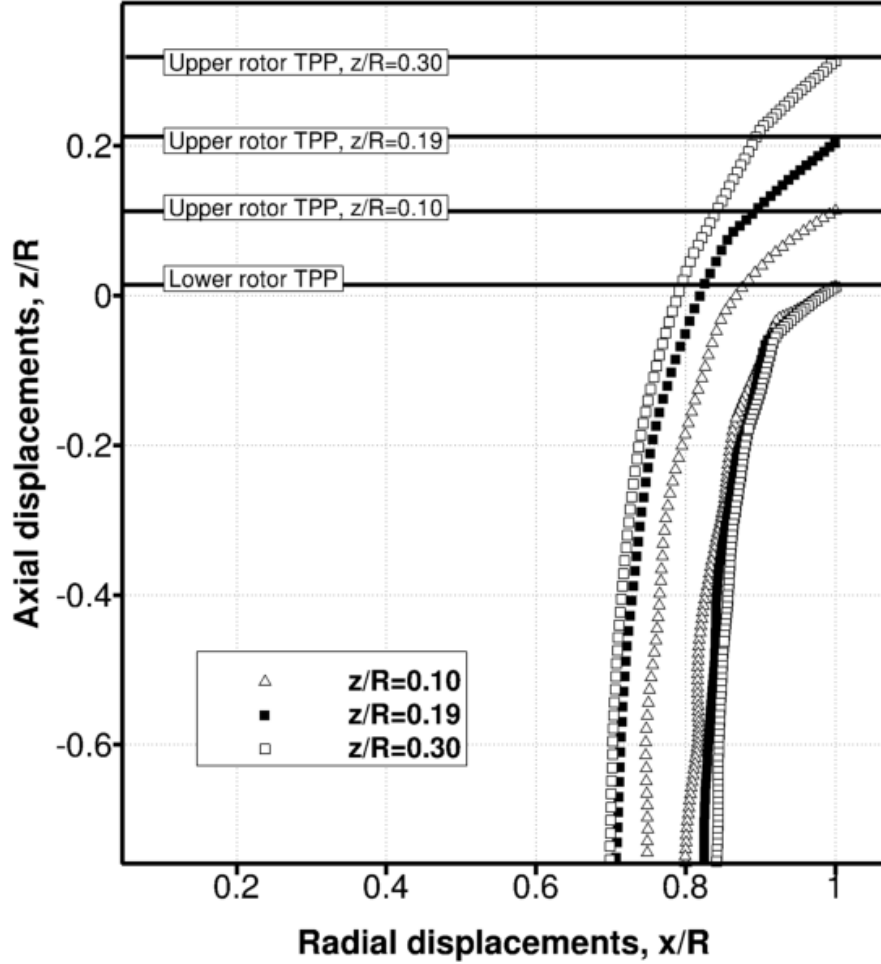


Fig. 50: Wake boundary as affected by varying inter-rotor spacing of the Harrington 2 rotor.

it is known that the aerodynamic interference deteriorates the performance. In hover, the coaxial system required 37% more total power than the isolated system. This difference in power requirement reduces as the advance ratio increases. At $\mu = 0.2$, the total power required by the coaxial system was 5% more than the isolated system. Therefore, the aerodynamic interference is a maximum in hover and decreases as advance ratio increases.

Figure 52 compares the upper and lower rotors of the UT coaxial rotor as isolated rotors. The upper rotor of the coaxial rotor was seen to require 33% more induced power in hover.

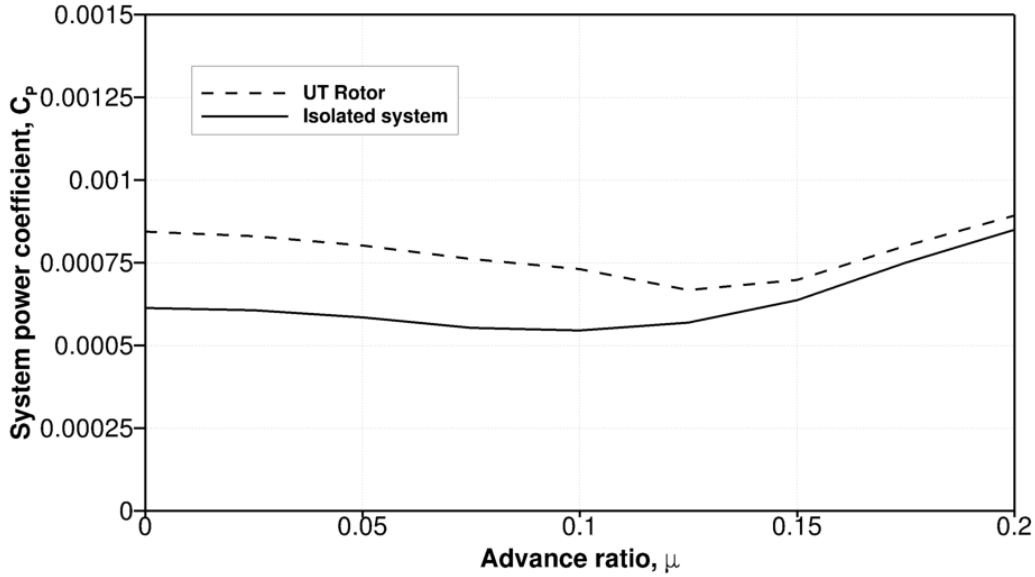


Fig. 51: Performance of the UT rotor compared to isolated rotor system operating at the same thrust.

This outcome indicates that the presence of the lower rotor affects its performance. Even as the advance ratio increases, the upper rotor does not operate completely independently. At moderately high advance ratio, the upper rotor performance is also affected because of aerodynamic interference. At $\mu = 0.2$, the upper rotor required 8% more induced power than the isolated rotor. The lower rotor performance is affected much more than the upper rotor. In hover, the lower rotor of the coaxial rotor required 77% more induced power than for the isolated rotor. Induced power requirement of the lower rotor of the coaxial rotor when compared to isolated rotor, dropped from 60% to 40% as advance ratio increased from 0.1 to 0.125. Beyond this advance ratio, the induced power requirement dropped to 11% at $\mu = 0.2$. While the induced power requirement varies, the profile power requirement remained the same when the upper and lower rotors were compared with the isolated rotors.

The L/D of the upper and lower rotors of the coaxial rotor system was compared with the isolated rotors, the results of which is shown in Fig. 53. The L/D of both the upper and lower rotors is less than isolated rotors. As the advance ratio increases the difference in the L/D decreases, which similar to the trend observed previously for the power required.

Figures 54–56 show the inflow ratio contour across the rotors in hover, $\mu = 0.1$ and 0.2 , respectively. In hover, the inflow across the upper rotor is much higher then the isolated upper rotor. The inflow across the lower rotor is also higher. As advance ratio increases to $\mu = 0.1$, the presence of the lower rotor influences the inflow across the upper rotor. The red regions in the aft section of the upper rotor of the coaxial rotor system indicate higher inflow compared to the blue and green regions on the isolated upper rotor. The forward part of the lower rotor does not become affected by the wake of the upper rotor, although it is a very small region on the lower rotor. At $\mu = 0.2$, the forward part of the upper rotor of the coaxial rotor system does not have the same inflow as the isolated upper rotor, the lower rotor affecting the inflow even at an advance ratio of $\mu = 0.2$. The inflow ratio across the aft part of the upper rotor is influenced by the lower rotor, a consequence of which the inflow ratio is higher than the isolated upper rotor. Although, the wakes at higher advance ratio skews back, the impingement of the upper rotor wake is apparent on the lower rotor; the yellow streaks on the lower rotor indicating regions of wake impingement. Also, the aft part of the lower rotor operates in the wake of the upper rotor.

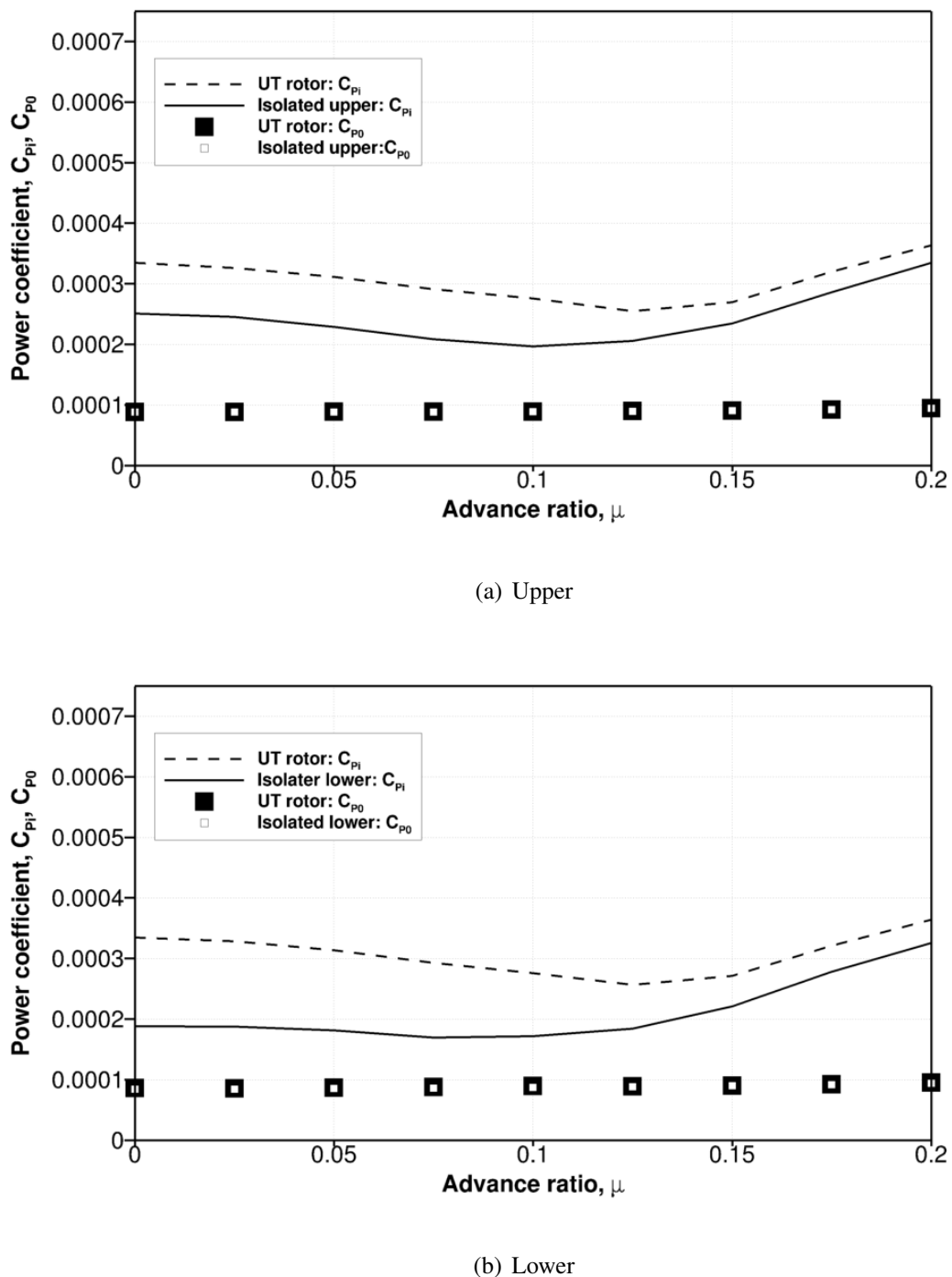


Fig. 52: Power in forward flight for the upper and lower rotors of UT rotor compared to isolated rotors operating at same thrust.

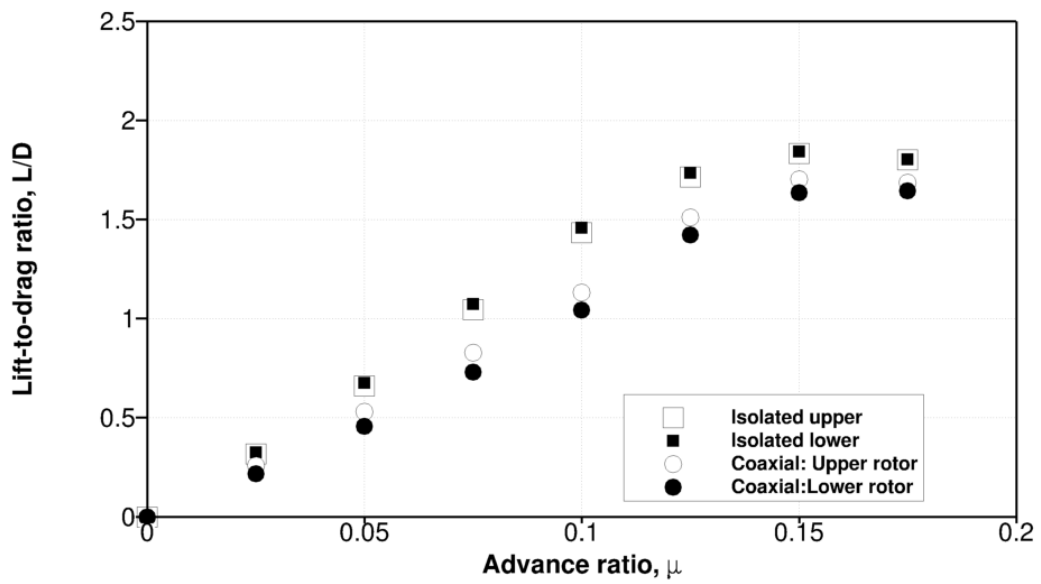


Fig. 53: Lift-to-drag ratios of the upper and lower rotors of the UT rotor compared to isolated rotors.

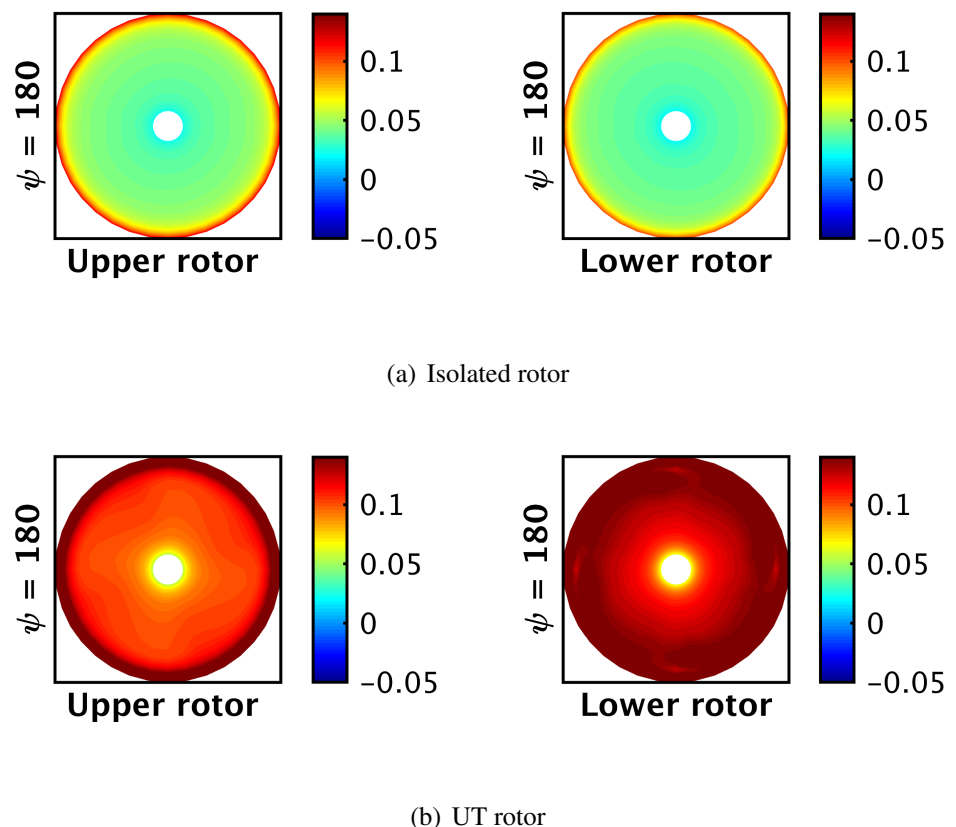


Fig. 54: Inflow ratio across UT rotor compared to isolated rotors in hover.

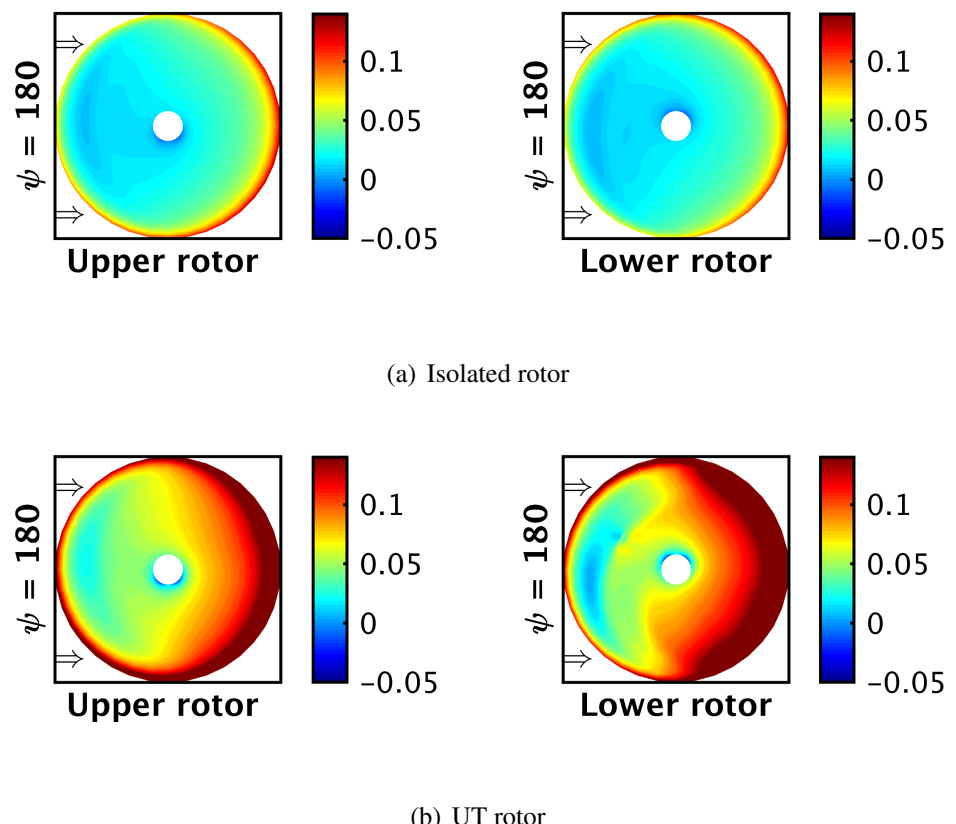


Fig. 55: Inflow ratio across UT rotor compared to isolated rotors at $\mu = 0.1$.

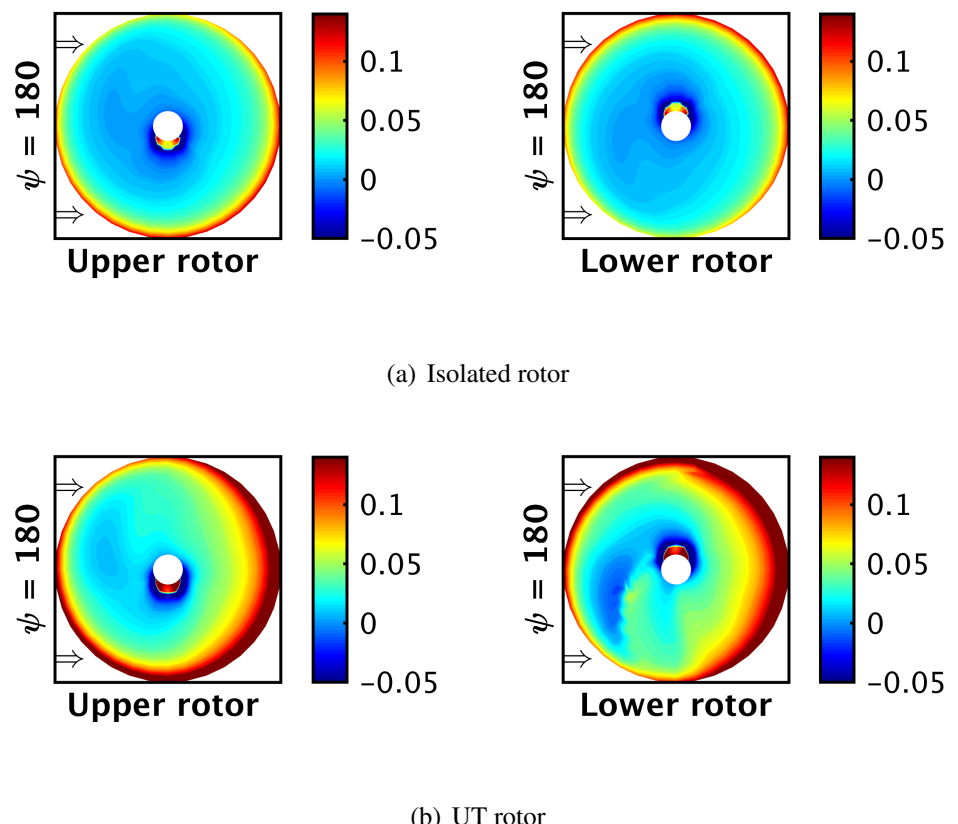


Fig. 56: Inflow ratio across UT rotor compared to isolated rotors at $\mu = 0.2$.

4. Conclusions and Recommendations

This final chapter summarizes the observations made from the results found during the research, draws some important conclusions, and also gives recommendations for future work.

First, a free-vortex method was validated against experimental measurements for coaxial rotors. The study also compared the coaxial rotor system with its “equivalent” single rotor, first by deriving an equivalent single rotor for the given coaxial rotor system, and then comparing thrust and power of both the rotor systems in hover and forward flight. Next, the effect of inter-rotor spacing on the performance of the coaxial rotor system was investigated. Finally, the effects of aerodynamic interference on the performance of the upper and lower rotor working in a coaxial system was quantified by comparing with an isolated rotor operating at the same conditions.

4.1 Conclusions

The observations and conclusions that have been drawn from various studies during this thesis research are as follows:

1. The FVM was validated for a coaxial rotor systems based on the measurements conducted by Harrington [8] and Cameron [18]. For hovering flight validation, the single rotor predictions compared very well with the experiments, while the power predic-

tions for the coaxial rotors were slightly overpredicted even though the trends were captured very well.

2. The FVM predictions were compared against forward flight experiments conducted by Dingeldien [9]. The power for both the single and coaxial rotors was overpredicted, however the trends with airspeed was captured well. While the discrepancies could be attributed to predictive capabilities of the free-vortex method, the trim conditions used during the experiments was not explicitly mentioned and remains a source of uncertainty. Attempts to resolve the discrepancies were made to try to establish the trim conditions using the available data from Dingeldien's research.
3. Rotor wake geometry predictions were compared against the smoke flow visualizations experiments for the Ka-32 coaxial rotor helicopter conducted by Akimov et. al. [47]. The predictions compared well at low advance ratios, however, the wake skew angles were under predicted for higher advance ratios. The differences, most likely, can be attributed to fuselage interference effects on the developing rotor wake.
4. To compare the conventional rotor and a coaxial rotor on a fair basis, an “equivalent” single rotor was derived for the given coaxial rotor geometry. The equivalent rotor had the same total number of blades, disk loading, solidity and tip speed as the coaxial rotor. The coaxial rotor was found to require about 9% less power than its equivalent single rotor in hovering flight. A break down of the total system power in to induced and profile power components showed that the induced power required by the coaxial rotor was 11–17% lower than the equivalent single rotor for the same

system thrust range. The profile power requirement for coaxial rotor and equivalent rotor was almost the same.

5. While the coaxial rotor required less total power for hovering flight, the power requirement at low advance ratios was almost the same when compared with its equivalent single rotor. Beyond $\mu = 0.125$, the coaxial rotor required more total power, and up to 38% more power at $\mu = 0.25$. At the higher advance ratios, there was evidence of blade stall on retreating side of the upper and lower rotors, the reason being that rotor blades were untwisted and uniform in planform.
6. The lift-to-drag ratio for the UT rotor is much lower than full scale rotors, however when compared with its equivalent single rotor, lift-to-drag ratio of the equivalent rotor was higher. The maximum lift-to-drag ratio for the UT rotor and its equivalent single rotor occurred at similar advance ratios.
7. Comparing the coaxial rotor at varying inter-rotor spacings showed that the power requirement increases as inter-rotor spacing reduces. All comparisons are made using the performance of the Harrington 2 with inter-rotor spacing of $z/R = 0.19R$ as the baseline. At a spacing of $z/R = 0.30R$ the coaxial system required 12% less power at low system thrusts and 0.08% at higher system thrust when compared with baseline rotor. At $z/R = 0.10R$, the coaxial rotor required almost 24% more power at all system thrusts. The increased power requirements at low inter-rotor spacings is because of the increased aerodynamic interference between the two rotors. For all inter-rotor spacings the profile power requirements remained the same.

8. The coaxial rotor required 37% more power in hover when compared with in isolated rotor system, which could be attributed to the aerodynamic interference between the upper and lower rotors. At higher advance ratios, the difference in power requirement reduced to 5% when compared with an isolated system. The upper and lower rotor require more induced power when compared with the isolated rotors, the effects of aerodynamic interference is maximum in hover and reduces with increasing advance ratio. The lift-to-drag ratio of the upper and lower rotor of the coaxial are affected at low advance ratio. Therefor, it is evident that even at moderately high advance ratios (e.g., $\mu \geq 0.2$), the upper rotor performance becomes affected by the lower rotor.

4.2 Recommendations for Future Work

This thesis has made an attempt to provide an insight in to the performance of a coaxial rotor. While the questions set out at the beginning have been answered, at least in part, several more questions have arisen and so require further research to resolve. Some suggestions for future work are the following:

1. The relative scarcity of experimental data on coaxial rotors makes the validation of performance prediction codes a difficult task, especially forward flight. Although there are measurements for coaxial rotors in the form of power and thrust, there is not much experimental data on the predicted wake geometry and blade loads. To further the levels of confidence and dependability on the predictive tools (even for initial design), it is recommended that a new series of experiments be conducted on coaxial rotors with specific emphasis on wake measurements, spanwise load measurements,

wake-blade interactions, etc., and also by using the necessary flow visualization techniques.

2. Blade-vortex interactions (BVI) between the upper rotor wake and the lower rotor blades result in highly unsteady aerodynamic loads, therefore, verification of the efficacy of the modeling of BVI in the free-vortex method is vital. Although the tip vortex model includes a “viscous” core growth model, BVI is inherently a viscous phenomenon. More emphasis is, therefore, needed to verify the ability to FVM to predict the basic quantitative behavior associated with BVI.
3. Comparing coaxial rotor with its “equivalent” rotor showed that the equivalent rotor required less power in forward flight. However, it is worth noting that the development of the reverse flow region affects the maximum attainable forward speed for the single rotor configuration. It is, therefore, recommended that if the main objective is higher cruise speed, the coaxial rotor design be further developed because it offers significant potential. However, this statement must be qualified by the need to keep the inter-rotor spacing to the minimum possible to reduce parasitic drag and while also avoiding blade collisions between the upper and lower rotors.

Bibliography

- [1] Bagai, A., “Aerodynamic Design of the X2 Technology Demonstrator Main Rotor Blade,” Proceedings of the American Helicopter Society 64th Annual Forum, AHS International, Montréal, Québec, Canada, April 29 – May 1, 2008.
- [2] Leishman, J. G., *Principles of Helicopter Aerodynamics*, 2nd Edition, Cambridge University Press, New York, NY, 2006.
- [3] Boulet, J., *History of the Helicopter: As Told by its Pioneers 1907–1956*, Editions France-Empire, Paris, 1984.
- [4] Liberatore, E. K., *Helicopters Before Helicopters*, Krieger Publishing Company, Malabar, FL, 1998.
- [5] Everett-Heath, J., *Soviet Helicopters: Design, Development and Tactics*, Jane’s, London, 1983.
- [6] Cheney, M. C, “The ABC Helicopter,” *Journal of the American Helicopter Society*. Vol. 14, No. 4, pp. 10–19, 1969.
- [7] Leishman, J. G., Syal, M., “Figure of Merit Definition for Coaxial Rotors,” *Journal of the American Helicopter Society*, Vol. 53, No. 3, pp. 290–300, 2008.

- [8] Harrington, R. D., "Full-Scale-Tunnel Investigation of the Static Thrust Performance of a Coaxial Helicopter Rotor," NACA TN-2318, March, 1951.
- [9] Dingeldien, R. C., "Wind-Tunnel Studies of the Performance of Multirotor Configurations," NACA TN-3236, August, 1954.
- [10] Bagai, A., Leishman, J. G., "Free-Wake Analysis of Tandem, Tilt-Rotor and Coaxial Rotor Configurations," *Journal of the American Helicopter Society*. Vol. 41, No. 3, pp. 196–207, 1996.
- [11] Lim, J. W., McAlister, K. W., Johnson, W., "Hover Performance Correlation for Full-Scale and Model-Scale Coaxial Rotors," *Journal of the American Helicopter Society*. Vol. 54, No. 3, pp. 32005-01–32005-14, 2009.
- [12] Coleman, C. P., "A Survey of Theoretical and Experimental Coaxial Rotor Aerodynamic Research," NASA TP-3675, 1997.
- [13] Rorke, J. B., "Hover Performance Tests of Full Scale Variable Geometry Rotors," NASA CR-2713, 1976.
- [14] Arents, D. N., "An Assessment of the Hover Performance of the XH-59A Advancing Blade Concept Demonstration Helicopter," USAAMRDL TN-25, 1977.
- [15] Ramasamy, M., "Hover Performance Measurements Toward Understanding Aerodynamic Interference in Coaxial, Tandem, and Tilt Rotors," *Journal of the American Helicopter Society*. Vol. 60, No. 3, pp. 1–17, 2015.

- [16] Cameron, C., Sirohi, J., “Performance and Loads of a Model Coaxial Rotor Part I: Wind Tunnel Testing,” Proceedings of the American Helicopter Society International 72nd Annual Forum, AHS International, West Palm Beach, FL , May 17–19, 2016.
- [17] Schmaus, J., Chopra, I., “Performance and Loads of a Model Coaxial Rotor Part II: Predication Validations with Measurements,” Proceedings of the American Helicopter Society International 72nd Annual Forum, AHS International, West Palm Beach, FL, May 17–19, 2016.
- [18] Cameron, C. G., Karpatne, A., Sirohi, J., “Performance of a Mach-Scale Coaxial Counter-Rotating Rotor in Hover,” *Journal of Aircraft*, Vol. 53, No. 3, pp. 746–755, May–June, 2016.
- [19] Betz, A., “Schraubenpropeller mit geringstem Energieverlust,” *Nachrichten von der Gesellschaft der Wissenschaften zu Göttingen, Mathematisch-Physikalische Klasse*, Vol. 1919, pp. 193–217, 1919.
- [20] Gessow, A., “Effect of Rotor Blade Twist and Planform Taper on Helicopter Hovering Performance,” NACA TN-L5H2, 1948.
- [21] Leishman, J. G., Ananthan, S., “An Optimum Coaxial Rotor System for Axial Flight,” *Journal of the American Helicopter Society*, Vol. 53, No. 4, pp. 366–381, 2008.
- [22] Bagai, A., Leishman, J. G., “Rotor Free-Wake Modeling Using a Pseudo-Implicit Technique Including Comparisons with Experimental Data,” *Journal of the American Helicopter Society*, Vol. 40, No. 3, pp. 29–41, 1995.

- [23] Syal, M., "Contributions to the Aerodynamic Optimization of a Co-axial Rotor System," M.S. Thesis, University of Maryland, College Park, MD, 2008.
- [24] Brown, R. E., "Rotor Wake Modeling for Flight Dynamic Simulation of Helicopters," *AIAA Journal*, Vol. 38, No. 1, pp. 57–63, 2000.
- [25] Brown, R. E., Line, A. J., "Efficient High-Resolution Wake Modeling Using the Vorticity Transport Equation," *AIAA Journal*, Vol. 43, No. 7, pp. 1434–1443, 2005.
- [26] Whitehouse, G. R., Brown, R. E., "Modeling the Mutual Distortions of Interacting Helicopter and Aircraft Wakes," *Journal of Aircraft*, Vol. 40, No. 3, pp. 440–449, 2003.
- [27] Whitehouse, G. R., Brown, R. E., "Modelling a Helicopter Rotors Response to Wake Encounters," *The Aeronautical Journal*, Vol. 108, No. 1079, pp. 15–26, 2004.
- [28] Brown, R. E., Whitehouse, G. R., "Modelling Rotor Wakes in Ground Effect," *Journal of the American Helicopter Society*, Vol. 49, No. 3, pp. 238–249, 2004.
- [29] Phillips, C., Brown, R. E., "Eulerian Simulation of the Fluid Dynamics of Helicopter Brownout," *Journal of Aircraft*, Vol. 46, No. 4, pp. 1416–1429, 2009.
- [30] Ahlin, G. A., Brown, R. E., "Investigating the Physics of Rotor Vortex Ring State Using the Vorticity Transport Model," 31st European Rotorcraft Forum, Florence, Italy, September 13–15, 2005.

- [31] Ahlin, G. A., Brown, R. E., “Wake Structure and Kinematics in the Vortex Ring State,” *Journal of the American Helicopter Society*, Vol. 54, No. 3, pp 32003-1–32003-18, 2009.
- [32] Kim, H. W., Brown, R. E., “A Rational Approach to Comparing the Performance of Coaxial and Conventional Rotors,” *Journal of the American Helicopter Society*, Vol. 55, No. 1, pp. 12003-1–12003-9, 2010.
- [33] Kim, H. W., Brown, R. E., “A Comparison of Coaxial and Conventional Rotor Performance,” *Journal of the American Helicopter Society*, Vol. 55, No. 1 pp. 12004-1–12004-20, 2010.
- [34] Ruzicka, G. C., Strawn, R. C., “Computational Fluid Dynamics Analysis of a Coaxial Rotor Using Overset Grids,” AHS Specialist’s Conference on Aeromechanics, San Francisco, CA, 2008.
- [35] Seokkwan, Y., William, M. C., Thomas, H. P., “Computations of Torque-Balanced Coaxial Rotor Flows,” 55th AIAA Aerospace Sciences Meeting, Grapevine, TX, January 9–13, 2017.
- [36] Juhasz, O., Syal, M., Celi, R., Khromov, V., Rand, O., Ruzicka, G, C., Strawn, R. C., “Comparison of Three Coaxial Aerodynamic Prediction Methods Including Validation with Model Test Data,” *Journal of the American Helicopter Society*, Vol. 59, No. 3, pp. 1–14, 2014.

- [37] Leishman, J. G., Bhagwat, M. J., Bagai, A., “Free-vortex Filament Methods for the Analysis of Helicopter Rotor Wakes,” *Journal of Aircraft*, Vol. 39, No. 5. pp. 759–775, 2002.
- [38] Saffman, P. G., “Low Reynolds Number Hydrodynamics,” *Journal of Fluid Mechanics*, Vol. 28, No. 4, pp. 826–828, 1967.
- [39] Bagai, A., Leishman, J. G., “The Maryland Free-Wake Analysis,” Technical Report, University of Maryland, MD, 1995.
- [40] Ananthan, S., “Analysis of Rotor Wake Aerodynamics During Maneuvering Flight Using a Free-Vortex Wake Methodology,” Ph.D Thesis, University of Maryland, MD, 2006.
- [41] Bhagwat, M. J., Leishman, J. G., “Stability, Consistency and Convergence of Time-Marching Free-Vortex Rotor Wake Algorithms,” *Journal of the American Helicopter Society*, Vol. 46, No. 1, pp. 59–71, 2001.
- [42] Bagai, A., “Contributions to the Mathematical Modeling of Rotor Flow-Fields using a Pseudo-Implicit Free-Wake Analysis,” Ph.D Thesis, University of Maryland, MD, 1995.
- [43] Beddoes, T. S., “Representation of Airfoil Behavior,” *Vertica*, Vol. 7, No. 2, pp. 183–187, 1983.

- [44] Taylor, M. K., "A Balsa-Dust Technique for Air-flow Visualization and its Application to Flow Through Model Helicopter Rotors in Static Thrust," NACA TN-2220, 1950.
- [45] McAlister, K., Tung, C., Rand, O., Khromov, V., Wilson, J. S., "Experimental and Numerical Study of a Model Coaxial Rotor," Proceedings of the American Helicopter Society 62nd Annual Forum, AHS International, Phoenix, AZ, May 9–11, 2006.
- [46] Abbott, I. H., Von Doenhoff, A. E., *Theory of Wing Sections*, Dover Publications, pp. 150, 1959.
- [47] Akimov, A. I., Butov, V. P., Bourtsev, B. N., Selemenev, S. V., "Flight Investigation of Coaxial Rotor Tip Vortex Structure," 50th Annual National Forum of the American Helicopter Society, Washington, D.C., May, 1994.
- [48] Oseen, C. W., "Über Wirbelbewegung in einer reibenden Flüssigkeit," *Annalen der Physik, Fys.* 7, pp. 14–21, 1915.
- [49] Lamb, H., *Hydrodynamics*, pp. 592–593, 668–669, Cambridge University Press, U.K., 1932.

A. Appendix: Rotor Geometries

Table A.1: *Rotor geometry of the Harrington 1.*

Parameter	Harrington 1
No. of rotors, N_r	2
No. of blades, N_b	2
Radius, R	3.81 m
Chord, c	0.287 m
Taper ratio, c_{root}/c_{tip}	2.61
Solidity, σ	0.027
Rotational frequency, Ω	40 rad/s
Tip speed, V_{tip}	150 m/s
Rotor spacing, z/R	0.19 R

Table A.2: *Rotor geometry of the Harrington 2.*

Parameter	Harrington 2
No. of rotors, N_r	2
No. of blades, N_b	2
Radius, R	3.81 m
Chord, c	0.457 m
Taper ratio, c_{root}/c_{tip}	1
Solidity, σ	0.076
Rotational frequency, Ω	31.5 rad/s
Tip speed, V_{tip}	120 m/s
Rotor spacing, z/R	0.19 R

Table A.3: *Rotor geometry of the UT Rotor.*

Parameter	UT Rotor
No. of rotors, N_r	2
No. of blades, N_b	2
Radius, R	1.016 m
Chord, c	0.080 m
Taper ratio, c_{root}/c_{tip}	1
Solidity, σ	0.05
Rotational frequency, Ω	83.66 rad/s
Tip speed, V_{tip}	85 m/s
Rotor spacing, z/R	$0.14R$

B. Appendix: Vortex Core Model

The Biot-Savart law assumes a potential vortex, which produces singularity value of velocity at its center. This means that points very close to the vortex will experience unrealistically large, non-physical induced velocities. Especially in the case of vortex and rotor blade interactions, such non-physical responses can cause the evolving rotor wake geometry to over-react and can quickly lead to numerical instabilities in the wake solution. Experiments on rotary and fixed wings have shown that in real flows, the tip vortices have viscous cores with finite radii. Implementing this physical behavior is vital to avoid all the numerical instabilities that may result by assuming potential (inviscid) vortices.

The selection of a vortex model for numerical purposes has to be approached very cautiously. In the FVM, the vortex model consists of a inner solid body rotation core, whereas the outer part of the vortex resembles the profile of a potential vortex. In general, the swirl velocity profile for a vortex is written as

$$V_\theta(r) = \frac{\Gamma r}{2\pi(r_c^{2n} + r^{2n})^{\frac{1}{n}}} \quad (\text{B.1})$$

where n is an integer variable, r is the radial distance from the center. The boundary separating the inner solid body (purely rotational) and the outer flow (potential) region lies at $r = r_c$; see Fig. 57.

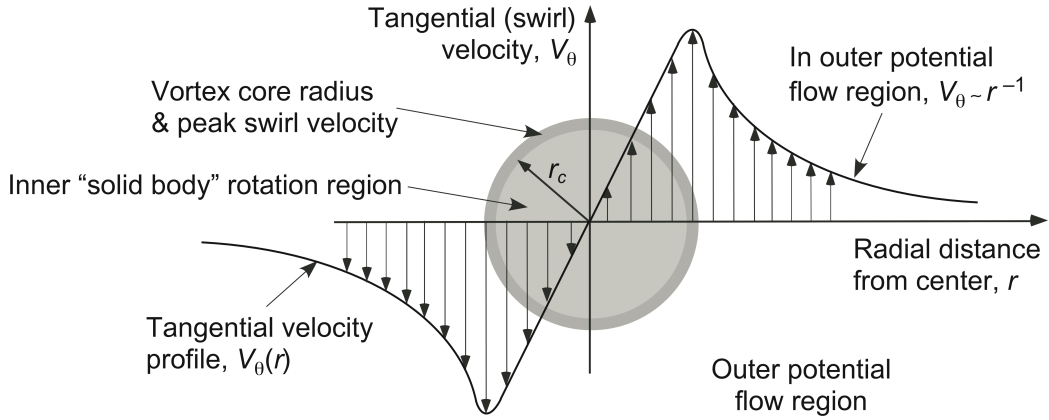


Fig. 57: Vortex core model [2].

Notice that if $n \rightarrow \infty$, the Rankine vortex profile is obtained; see Eq B.3. Although the Rankine vortex exhibits the key features of a viscous vortex, it over-predicts the values of swirl velocity. Another vortex model given by Oseen [48] and Lamb [49] for a single viscous vortex in an unbounded incompressible, laminar flow is written as

$$V_\theta(r) = \frac{\Gamma}{2\pi r_c r} \left(1 - e^{-\alpha r} \right) \quad (\text{B.2})$$

where $\alpha = 1.25643$. In Eq. B.1 if $n = 1$, the vortex is commonly known as the “Scully vortex.” While the Scully vortex is a good representation of the physical nature of the vortex, the FVM uses the velocity profile corresponding to $n = 2$, which is an algebraic approximation to the Lamb-Oseen vortex. The FVM allows the option to the user to choose between these two velocity profiles, i.e., $n = 1, 2$ and the Rankine velocity profile. The velocity profiles available in MFW are summarized as

1. For $n \rightarrow \infty$, Rankine vortex:

$$V_\theta(r) = \begin{cases} \left(\frac{\Gamma}{2\pi r_c}\right)\bar{r}, & 0 \leq \bar{r} \geq r_c \\ \left(\frac{\Gamma}{2\pi r_c}\right)\frac{1}{\bar{r}}, & \bar{r} > r_c \end{cases} \quad (\text{B.3})$$

2. $n = 1$ Scully vortex:

$$V_\theta(r) = \frac{\Gamma}{2\pi r_c} \frac{\bar{r}}{\left(1 + \bar{r}^2\right)} \quad (\text{B.4})$$

3. $n = 2$ vortex (model used for present study):

$$V_\theta(r) = \frac{\Gamma}{2\pi r_c} \frac{\bar{r}}{\sqrt{1 + \bar{r}^4}} \quad (\text{B.5})$$

where $\bar{r} = r/r_c$. The normalized velocity profiles are shown in Fig. 58. It is clearly seen that the Rankine vortex defines a discontinuous boundary between the inner solid body and the outer potential profile region. For $n = 1$ and $n = 2$, the peak velocities are lower than the Rankine vortex but there is a smooth transition from the inner solid body rotation and the outer potential flow region.

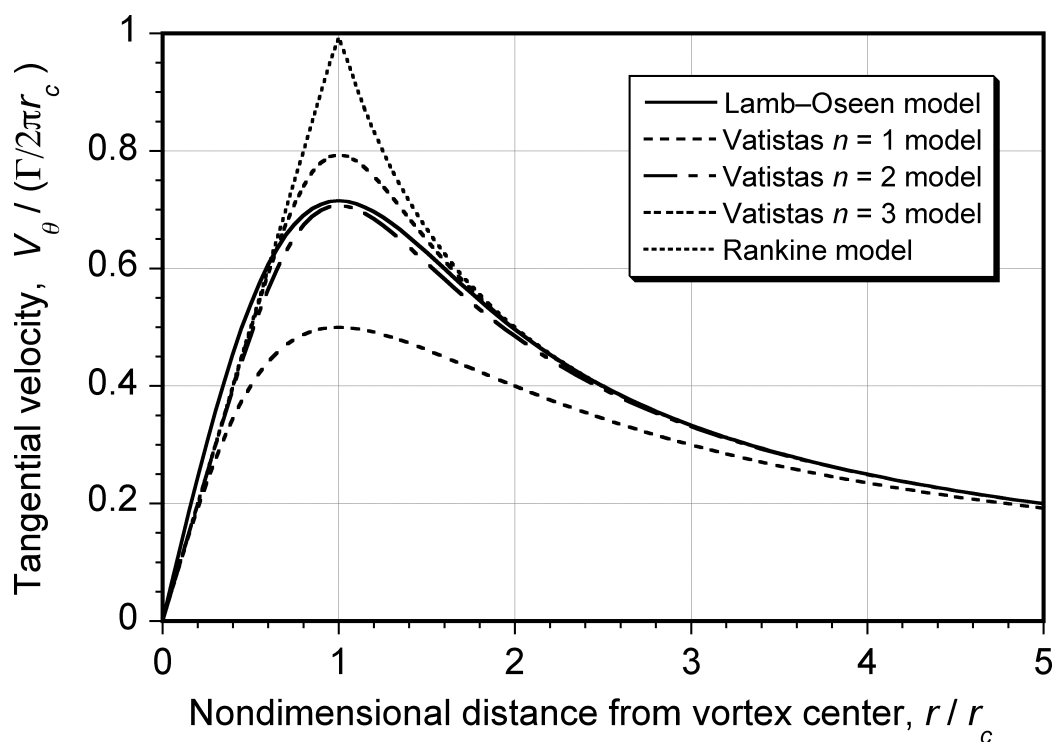


Fig. 58: Non-dimensional tangential velocity profiles [2].

C. Appendix: MATLAB Code for Contour Plots

```
clear all  
clc  
format long  
  
ns=40;  
vtip=85; % For harrington 1 Vtip= 152.4 m/s  
% For harrington 2 Vtip= 119.48 m/s  
% For Sirohi Vtip=85 m/s  
  
dp=10;  
p=360/dp;  
n_r=2;  
  
% mu=0.5;  
% muc=0.023;  
  
ct=0.005;
```

```

z_R=0.30;

mu=0.25;

generate_contour=1; % 1 to generate
save_fig=1;           % 1 to enable save
hover_only=0;

% Harrington 1 directory
% cd([' / data2 / Stanrich / THESIS / CO AXIAL / Harrington 1 / Harr 1
    coax / ', num2str(ct), '/ runtime ']);
% cd([' / data2 / Stanrich / THESIS / CO AXIAL / Harrington 1 / Harr 1
    Single / ', num2str(ct), '/ runtime ']);
% cd([' / data2 / Stanrich / THESIS / CO AXIAL / Harrington 1 / Harr 1
    coax forward / ', num2str(mu), '/ runtime ']);
% cd([' / data2 / Stanrich / THESIS / CO AXIAL / Harrington 1 /
    newharr1coaxfwd / ', num2str(mu), '/ runtime ']);

% Harrington 2 directory
% cd([' / data2 / Stanrich / THESIS / CO AXIAL / Harrington 2 / Harr 2
    coax / ', num2str(ct), '/ runtime ']);
% cd([' / data2 / Stanrich / THESIS / CO AXIAL / Harrington 2 / z_R runs
    / ', num2str(z_R), '/ ', num2str(ct), '/ runtime ']);

```

```
% cd(['/data2/Stanrich/THESIS/CO_AXIAL/Harrington_2/z_R_runs
      /Harr_2_coax_(single_equiv)/', num2str(ct), '/runtime']);
% cd(['/data2/Stanrich/THESIS/CO_AXIAL/Harrington_2/Harr_2
      single /', num2str(ct), '/runtime']);

% Sirohi Directory
% cd(['/data2/Stanrich/THESIS/CO_AXIAL/Sirohi/Sirohi_Coaxial
      /', num2str(ct), '/runtime']);
%cd(['/data2/Stanrich/THESIS/CO_AXIAL/Sirohi/Sirohi_Coaxial
      forward/z_R/', num2str(z_R), '/runtime']);
%cd(['/data2/Stanrich/THESIS/CO_AXIAL/Sirohi/Sirohi_Coaxial
      forward/mu/', num2str(mu), '/runtime']);
% cd(['/data2/Stanrich/THESIS/CO_AXIAL/Sirohi/Sirohi_Coaxial
      forward/mu/Single_rotor/', num2str(mu), '/lower/runtime']);
% cd(['/data2/Stanrich/THESIS/CO_AXIAL/Sirohi/Sirohi_Single
      equiv/mu/', num2str(mu), '/runtime']);
% cd(['/data2/Stanrich/THESIS/CO_AXIAL/Sirohi/
      SirohiSingEquivNew/', num2str(mu), '/runtime']);

% For 2nd rotor
```

```

if n_r==2

% cd([' / data2 / Stanrich / Results / mu_ , num2str(mu) , ' muc_ ,
num2str(muc) , ' alpha_ , num2str(alpha) , '/ runtime ]); 

%cd([' / data2 / Stanrich / THESIS / CO AXIAL / Harrington 1 / Harr 1
coax / , num2str(ct) , '/ runtime ]);

[filename directory_name] = uigetfile('lift.dat', 'Select a
file');

fullname = fullfile(directory_name, filename);

lift = load(fullname);

% load inflow data (VBZ_mr.dat)

[filename directory_name] = uigetfile('VBZ_mr.dat', 'Select
a file');

fullname = fullfile(directory_name, filename);

inflow = load(fullname);

% load VBZ_PSI.dat

[filename directory_name] = uigetfile('VBZ_PSI_mr.dat', ',
Select a file');

fullname = fullfile(directory_name, filename);

inflowpsi = load(fullname);

```

```

% for lower rotor

% Augment azimuthal and radial locations

for i=1:ns

    xloc_t(i)=inflow(ns+1,i,1);

end

xloc=xloc_t';

dpsi_d=linspace(0,360,p+1)';

dpsi=(pi/180)*dpsi_d;

dpsi(p+1)=dpsi(1);

k=0;

for i=1:40:ns*p

    k=k+1;

    for j=1:ns

        lift(i+j-1,12)=xloc(j);

        lift(i+j-1,13)=dpsi(k);

    end

end

dummy=inflowpsi(1+(ns*p):2*ns*p,6);

% dummy=inflowpsi(1:ns*p,6);

dummy_p=1*((1/vtip)*dummy);

lift=[lift dummy_p];

```

```

r=left(1:40,12);

t=dpsi;

[R,T]=meshgrid(r,t);

z=left(:,14);

z1=left(:,5);

z2=left(:,9);

z3=left(:,7);

k=0;

for i=p+1:1:2

    for j=1:n

        inf_1(i,j)=z(k+j);

        aoae_1(i,j)=z1(k+j);

        c1m2_1(i,j)=z2(k+j);

        c1_l(i,j)=z3(k+j);

    end

    k=k+40;

end

inf_1(1,:)=inf_1(p+1,:);

aoae_1(1,:)=aoae_1(p+1,:);

```

```

c1m2_1(1,:)=c1m2_1(p+1,:);

c1_1(1,:)=c1_1(p+1,:);

[X,Y]=pol2cart(T,R);

aoae_lower=aoae_1';

aoae_lower(:,p+1)=r';

save('aoae_lower.dat','aoae_lower','ascii','tabs')

infmax_1=max(max(inf_1));

infmin_1=min(min(inf_1));

infstep_1=(infmax_1-infmin_1)/15;

aoaemax_1=max(max(aoae_1));

aoaemin_1=min(min(aoae_1));

aoaestep_1=(aoaemax_1-aoaemin_1)/15;

c1m2max_1=max(max(c1m2_1));

c1m2min_1=min(min(c1m2_1));

c1m2step_1=(c1m2max_1-c1m2min_1)/15;

c1max_1=max(max(c1_1));

```

```

c1min_1=min( min( c1_1));
c1step_1=(c1max_1 - c1min_1)/15;

if generate_contour==1
figure(1);clf;
fig = gcf;
fig.PaperUnits = 'inches';
fig.PaperPosition = [0 0 5 1.5];
whitebg('k')
subplot(1,2,2)
contourf(X,Y,inf_1,150,'LineStyle','none')
colormap(jet)
hcb=colorbar;
caxis([-0.05,0.14])
set(gca,'xtick',[], 'ytick',[])
if mu>0
text(1,0.75,' \rightarrow ')
text(1, 0.75 , '\rightarrow')
end
axis square
grid on
ylabel(' \psi = 180 ', 'FontSize',10, 'FontWeight','bold')

```

```

xlabel('Lower rotor ', 'FontSize', 10, 'FontWeight', 'bold')

figure(2); clf;

fig = gcf;
fig.PaperUnits = 'inches';
fig.PaperPosition = [0 0 5 1.5];
whitebg('k')

subplot(1,2,2)

contourf(X,Y,aoae_1,150, 'LineStyle', 'none')

colormap(jet)

hcb=colorbar;

caxis([ 2.43 ,2.95])

set(gca, 'xtick',[], 'ytick',[])

% text( 1 ,0.75 , '\rightarrow')
% text( 1 , 0.75 , '\rightarrow')

axis square

ylabel('\psi=180', 'FontSize', 10, 'FontWeight', 'bold')

xlabel('Lower rotor ', 'FontSize', 10, 'FontWeight', 'bold')

figure(3); clf;

subplot(1,2,2)

contourf(X,Y,clm2_1,150, 'LineStyle', 'none')

```

```

colormap(jet)

hcb=colorbar;

caxis([ 0.016 ,0.14])

set(gca , 'xtick' ,[], 'ytick' ,[])

text( 1 ,0.75 , '\rightarrow')

text( 1 , 0.75 , '\rightarrow')

axis square

ylabel(' \psi=180 ', 'FontSize' ,12 , 'FontWeight' , 'bold')

xlabel(' ' , 'FontSize' ,12 , 'FontWeight' , 'bold')

figure(4); clf;

fig = gcf;

fig.Color='black';

fig.PaperUnits = 'inches';

fig.PaperPosition = [0 0 5 1.5];

whitebg('k')

subplot(1,2,2)

contourf(X,Y,c1_1,150 , 'LineStyle' , 'none')

colormap(jet)

hcb=colorbar;

caxis([ 1.29 ,1.24])

set(gca , 'xtick' ,[], 'ytick' ,[])

```

```

if mu>0

text( 1 ,0.75 , '\Rightarrow')
text( 1 , 0.75 , '\Rightarrow')

end

axis square

ylabel(' \psi = 180 ', 'FontSize' ,10 , 'FontWeight' , 'bold')

xlabel('Lower rotor ', 'FontSize' ,10 , 'FontWeight' , 'bold')

end

end

%%

% for 1st rotor

if n_r==1 || n_r==2

% cd(['/data2/Stanrich/THESIS/CO AXIAL/Sirohi/Sirohi Coaxial
forward/mu/Single rotor/' , num2str(mu) , '/upper/runtime'])

[filename directory_name] = uigetfile('lift_u.dat', 'Select
a file');

fullname = fullfile(directory_name, filename);

lift = load(fullname);

```

```

% load inflow data (VBZ_mr.dat)

[filename directory_name] = uigetfile('VBZ_mr.dat', 'Select
a file');

fullname = fullfile(directory_name, filename);

inflow = load(fullname);

% load VBZ_PSI.dat

[filename directory_name] = uigetfile('VBZ_PSI_mr.dat', 'Select
a file');

fullname = fullfile(directory_name, filename);

inflowpsi = load(fullname);

% Augment azimuthal and radial locations

for i=1:ns

    xloc_t(i)=inflow(ns+1:i,1);

end

xloc=xloc_t';

dpsi_d=linspace(0,360,p+1)';

dpsi=(pi/180)*dpsi_d;

dpsi(p+1)=dpsi(1);

k=0;

```

```

for i=1:40:ns*p
    k=k+1;
    for j=1:ns
        lift(i+j-1,12)=xloc(j);
        lift(i+j-1,13)=dpsi(k);
    end
end

dummy=inflowpsi(1:ns*p,6);
dummy_p=1*((1/vtip)*dummy);
lift=[lift dummy_p];

r=lift(1:40,12);
t=dpsi;

[R,T]=meshgrid(r,t);

z=lift(:,14);
z1=lift(:,5);
z2=lift(:,9);
z3=lift(:,7);

k=0;
for i=1:p

```

```

for j=1:ns

    inf_u(i,j)=z(k+j);

    aoae_u(i,j)=z1(k+j);

    clm2_u(i,j)=z2(k+j);

    cl_u(i,j)=z3(k+j);

end

k=k+40;

end

inf_u(p+1,:)=inf_u(1,:);

aoae_u(p+1,:)=aoae_u(1,:);

clm2_u(p+1,:)=clm2_u(1,:);

cl_u(p+1,:)=cl_u(1,:);

[X,Y]=pol2cart(T,R);

aoae_upper=aoae_u';

aoae_upper(:,p+1)=r';

save('aoae_upper.dat','aoae_upper','ascii','tabs')

infmax_u=max(max(inf_u));

infmin_u=min(min(inf_u));

infstep_u=(infmax_u - infmin_u)/15;

```

```

aoaemax_u=max(max(aoae_u));
aoaemin_u=min(min(aoae_u));
aoaestep_u=(aoaemax_u-aoaemin_u)/15;

clm2max_u=max(max(clm2_u));
clm2min_u=min(min(clm2_u));
clm2step_u=(clm2max_u-clm2min_u)/15;

clmax_u=max(max(c1_u));
clmin_u=min(min(c1_u));
clstep_u=(clmax_u-clmin_u)/15;

if generate_contour==1
figure(1);
fig = gcf;
% fig.Color='black';
fig.PaperUnits = 'inches';
fig.PaperPosition = [0 0 5 1.5];
if n_r==2
subplot(1,2,1)
end
contourf(X,Y,inf_u,150,'LineStyle','none')

```

```

colormap(jet)

hcb=colorbar;

caxis([ 0.05 ,0.14])

set(gca , 'xtick' ,[], 'ytick' ,[])

if mu>0

text( 1 ,0.75 , '\rightarrow')

text( 1 , 0.75 , '\rightarrow')

end

axis square

ylabel('psi = 180' , 'FontSize' ,10 , 'FontWeight' , 'bold')

xlabel('Upper rotor ' , 'FontSize' ,10 , 'FontWeight' , 'bold')

figure(2);

fig = gcf;

fig.PaperUnits = 'inches';

fig.PaperPosition = [0 0 5 1.5];

if n_r==2

subplot(1,2,1)

end

contourf(X,Y,aoae_u ,150 , 'LineStyle' , 'none')

colormap(jet)

hcb=colorbar;

```

```

caxis([ 2.43 ,2.95])

set(gca , 'xtick' ,[], 'ytick' ,[])

% text( 1 ,0.75 ,'\rightarrow')

% text( 1 , 0.75 ,'\rightarrow')

axis square

ylabel(' \psi = 180 ', 'FontSize' ,10 , 'FontWeight' , 'bold')

xlabel('Upper rotor ', 'FontSize' ,10 , 'FontWeight' , 'bold')

figure(3);

if n_r==2

subplot(1 ,2 ,1)

end

contourf(X,Y,clm2_u ,150 , 'LineStyle' , 'none' )

colormap(jet)

hcb=colorbar;

caxis([ 0.016 ,0.14])

set(gca , 'xtick' ,[], 'ytick' ,[])

text( 1 ,0.75 ,'\rightarrow')

text( 1 , 0.75 ,'\rightarrow')

axis square

ylabel(' \psi=180 ', 'FontSize' ,12 , 'FontWeight' , 'bold')

xlabel(' ', 'FontSize' ,12 , 'FontWeight' , 'bold')

```

```
figure(4);

fig = gcf;
fig.PaperUnits = 'inches';
fig.PaperPosition = [0 0 5 1.5];
if n_r==2
    subplot(1,2,1)
end

contourf(X,Y,cl_u,150,'LineStyle','none')

colormap(jet)

hcb=colorbar;

caxis([ 1.29 ,1.24])

set(gca,'xtick',[], 'ytick',[])
if mu>0
    text( 1 ,0.75 , '\rightarrow')
    text( 1 , 0.75 , '\rightarrow')
end

axis square

if n_r==2
    xlabel('Upper rotor ', 'FontSize',10, 'FontWeight','bold')
end

end
```

```
cd ('.. / ')
end

if save_fig==1

figure(1);

saveas(figure(1), 'inflow.png')
print('inflow', ' dpng', ' r600')

figure(2);

saveas(figure(2), 'aoae.png')
print('aoae', ' dpng', ' r600')

figure(3);

saveas(figure(3), 'clm2.png')

fig = gcf;
fig.PaperUnits = 'inches';
fig.PaperPosition = [0 0 6 3];
print('clm2', ' dpng', ' r600')

figure(4);

saveas(figure(4), 'cl.png')

print('cl', ' dpng', ' r600')

end

if hover_only==1
```

```

%% Hover only

inf_mean_l=zeros(ns+2,1);
inf_mean_u=zeros(ns+2,1);
cl_mean_l=zeros(ns+2,1);
cl_mean_u=zeros(ns+2,1);
aoa_mean_l=zeros(ns+2,1);
aoa_mean_u=zeros(ns+2,1);
rad_loc=zeros(ns+2,1);
rad_loc(ns+2,1)=1;
for i=1:ns
    temp_sum_l=0;
    temp_sum_u=0;
    temp_sum_l_cl=0;
    temp_sum_u_cl=0;
    temp_sum_l_aoa=0;
    temp_sum_u_aoa=0;
    for j=1:360/dp
        if n_r==2
            temp_sum_l=temp_sum_l+inf_l(j,i);
        end
        temp_sum_u=temp_sum_u+inf_u(j,i);
        if n_r==2

```

```

temp_sum_l_cl=temp_sum_l_cl+cl_l(j,i);

end

temp_sum_u_cl=temp_sum_u_cl+cl_u(j,i);

if n_r==2

temp_sum_l_aoa=temp_sum_l_aoa+aoae_l(j,i);

end

temp_sum_u_aoa=temp_sum_u_aoa+aoae_u(j,i);

end

inf_mean_l(i+1)=temp_sum_l/(360/dp);

inf_mean_u(i+1)=temp_sum_u/(360/dp);

cl_mean_l(i+1)=temp_sum_l_cl/(360/dp);

cl_mean_u(i+1)=temp_sum_u_cl/(360/dp);

aoa_mean_l(i+1)=temp_sum_l_aoa/(360/dp);

aoa_mean_u(i+1)=temp_sum_u_aoa/(360/dp);

rad_loc(i+1,1)=r(i,1);

end

inf_mean_l=[inf_mean_l rad_loc];

inf_mean_u=[inf_mean_u rad_loc];

cl_mean_l=[cl_mean_l rad_loc];

cl_mean_u=[cl_mean_u rad_loc];

aoa_mean_l=[aoa_mean_l rad_loc];

aoa_mean_u=[aoa_mean_u rad_loc];

```

```
save('inf_mean_l.dat','inf_mean_l','ascii','tabs')  
save('inf_mean_u.dat','inf_mean_u','ascii','tabs')  
save('cl_mean_l.dat','cl_mean_l','ascii','tabs')  
save('cl_mean_u.dat','cl_mean_u','ascii','tabs')  
save('aoa_mean_l.dat','aoa_mean_l','ascii','tabs')  
save('aoa_mean_u.dat','aoa_mean_u','ascii','tabs')  
  
end
```

D. Appendix: MATLAB Code for Wake Boundary

```

clear all

clc

nt=6;
dp=10;
dz=1+(nt*360/dp);
ct=0.005;
z_R=1.5;
alpha_s=3.9;
beta_0=0;
mu=0.169;

TT=[cosd(alpha_s) 0 sind(alpha_s);0 1 0; sind(alpha_s) 0
cosd(alpha_s)];
T=inv(TT);

% cd([' / data2 / Stanrich / THESIS / CO_AXIAL / Harrington_2 / Harr_2
single / ', num2str(ct), '/ runtime / wakefiles ']);

```

```
% cd(['/data2/Stanrich/THESIS/CO_AXIAL/Harrington_1/Harr_1
      coax/num2str(ct),'/runtime/wakefiles']);
% cd(['/data2/Stanrich/THESIS/CO_AXIAL/Harrington_2/z_R_runs
      /',num2str(z_R),'/',num2str(ct),'/runtime/wakefiles']);
% cd(['/data2/Stanrich/THESIS/CO_AXIAL/Harrington_1/Harr_1
      coax_forward/num2str(mu),'/runtime/wakefiles']);
% cd(['/data2/Stanrich/THESIS/CO_AXIAL/Sirohi/Sirohi_Single
      equiv/mu/num2str(mu),'/runtime/wakefiles']);
% cd(['/data2/Stanrich/THESIS/CO_AXIAL/Sirohi/Sirohi_Coaxial
      forward/mu/num2str(mu),'/runtime/wakefiles']);
cd(['/data2/Stanrich/THESIS/CO_AXIAL/ka32/num2str(mu),/
      runtime/wakefiles']);

[filename directory_name] = uigetfile('FWGEOM_mr_050.dat','
      Select a file');

fullname = fullfile(directory_name, filename);
geom = load(fullname);

nr=2;
psi=10;
psi_loc=psi/dp+0;
% wake_loc=zeros(dz,3);
```

```

% wake_loc_f=zeros(dz,3);

A=zeros(3,1);

j=1;

for i=1:dz*360/dp*nr

if geom(i,4)<=0.01 && geom(i,4)>=0.01 && geom(i,5)
>= 0.4 && geom(i,3)~=0

wake_loc(j,1)=geom(i,3);

wake_loc(j,2)=geom(i,4);

wake_loc(j,3)=geom(i,5);

A=[wake_loc(j,1);wake_loc(j,2);wake_loc(j,3)]; 

AA=T*A;

wake_loc(j,1)=AA(1,1);

wake_loc(j,2)=AA(2,1);

wake_loc(j,3)=AA(3,1);

j=j+1;

end

end

cd ('..');

save('wake_boundary.dat','wake_loc','ascii','tabs');

plot(wake_loc(:,1),wake_loc(:,3),'*')

axis square;

```